TÉCNICO LISBOA

Finite element modelling of iron corrosion behavior

Pedro Manuel Neto Neves

Thesis to obtain the Master of Science Degree in

Mechanical Engineering

Supervisors: Prof. Maria Beatriz Cipriano de Jesus Silva

Prof. Maria de Fátima Reis Vaz

Examination Committee

Chairperson: Prof. Rui Manuel dos Santos Oliveira Baptista

Supervisor: Prof. Maria Beatriz Cipriano de Jesus Silva

Members of the Committee: Prof. Augusto Manuel Moura Moita de Deus

Dr. João Pedro Grosa Magrinho

September 2021

Abstract

The number of bone injuries is rising due to several different factors, such as the increase in the elderly population, the soaring average life expectancy and the growing number of osteoporosis cases. This has led to research for better solutions for fixing and repairing bone, in general performed by introducing an implant that may be permanent or temporary.

Bio-inert metals tend to be used as temporary implant materials, which are not ideal as sometimes a second surgery is needed, for example, due to the appearance of inflammation. This outcome has prompted research into other materials that could better perform this function and that could degrade inside the human body, for example, biodegradable materials.

Nowadays, pure iron is one of the most investigated metals for this purpose presenting good biocompatibility. However, iron presents a higher stiffness than bone, which leads to the stress shielding effect and shows a slow degradation in the human body. These disadvantages can be overcome if porosity and topological optimization are used.

The purpose of this dissertation is to mechanically characterize pure iron and numerically evaluate the corrosion behaviour of this material when in contact with simulated body fluid (SBF) . To do so, the finite element analysis (FEA) software *COMSOL Multiphysics* with the Corrosion Module was used. The results obtained in the simulations were compared with experimental results accomplished by Salama et al. [1], enabling an evaluation of the accuracy of the models developed. Numerical analysis of corrosion was performed on simple iron specimens with a parallelepiped closed shape (bulk specimens), and on porous specimens with parallelepiped shape with a certain distribution of holes. The samples used were similar to the ones of Salama et al. [1]. Several corrosion parameters were tested and their effect on the weight loss of samples was evaluated.

Firstly, a mesh refinement was performed to evaluate the convergence of results. Other parameters were also changed including two different types of boundary conditions, changing the electrolyte volume, the specimen positioning as well as the duration of the tests. The experimental results of the bulk specimens allowed developing four different calibrated models, later used on porous iron specimens. It was verified that the mass loss in the numerical results was always slightly higher than in the experimental results.

Nevertheless, the previous experimental results were used to tune the parameters of the FEA enabling a good correlation between simulations and experiments. The simulation data gathered in this work can be further applied, for example, on the analysis of porous specimens with complex geometries.

Keywords: numerical simulation, corrosion, biodegradability, porous iron, mechanical properties

Resumo

O número de lesões ósseas tem vindo a aumentar devido a vários diferentes fatores, tais como o aumento da população idosa, o aumento da esperança média de vida e o número crescente de casos de osteoporose. Isto levou à investigação de melhores soluções para a fixação e reparação de ossos, em geral realizada através da introdução de um implante que pode ser permanente ou temporário.

Os materiais dos implantes temporários tendem a ser metais bio-inertes, que por vezes não são os ideais, sendo necessária uma segunda cirurgia para a sua remoção, por exemplo, devido ao aparecimento de inflamação. De modo a evitar a cirurgia de remoção do implante, a utilização de materiais biodegradáveis, que se consigam degradar dentro do corpo humano tem vindo a ser proposta.

Atualmente, o ferro puro é um dos metais mais investigados para essa finalidade apresentando excelente biocompatibilidade. No entanto, o ferro apresenta maior rigidez do que o osso, o que conduz ao efeito de stress-shielding, para além de apresentar lenta degradação no corpo humano. Essas desvantagens podem ser superadas ao conjugar a porosidade com modificações topológicas.

O objetivo desta dissertação é caracterizar mecanicamente o ferro puro e avaliar numericamente o comportamento à corrosão desse material quando em contato com fluido corporal simulado (SBF). Deste modo, foi usado o software de análise de elementos finitos (FEA) *COMSOL Multiphysics* com o Módulo de Corrosão. Os resultados das simulações foram comparados com resultados experimentais obtidos por Salama et al. [1], permitindo uma avaliação dos modelos desenvolvidos. A análise numérica da corrosão foi realizada em amostras de ferro com forma paralelepipédica (amostras bulk), e em amostras com formato paralelepípedico mas com uma certa distribuição de porosidade (amostras porosas). As amostras utilizadas foram semelhantes às usadas por Salama et al. [1]. Os resultados experimentais anteriores foram usados para ajustar os parâmetros do FEA.

Vários parâmetros do modelo de corrosão foram testados e o seu efeito na perda de peso das amostras foi avaliado. Em primeiro lugar foi realizado um refinamento da malha para avaliar a convergência dos resultados. Os outros parâmetros que foram variados incluíram dois tipos diferentes de condições de fronteira, o volume do electrólito, o posicionamento da amostra, bem como a duração dos testes. Os resultados experimentais das amostras bulk permitiram a calibração de quatro modelos, que foram posteriormente utilizados com os provetes porosos. Verificou-se que a perda de massa nos resultados numéricos foi sempre ligeiramente superior à verificada nos resultados experimentais.

Os resultados das simulações obtidos neste trabalho podem ser posteriormente aplicados, por exemplo, na análise do comportamento à corrosão de amostras porosas de geometrias complexas.

Palavras-chave: simulação numérica, corrosão, biodegradabilidade, ferro poroso, propriedades mecânicas

Acknowledgements

First and foremost, I would like to express my sincere gratitude towards my supervisors Professor Beatriz Silva and Professor Fátima Vaz for the excellent guidance, the knowledge transmitted, and all the help and availability provided at any occasion. Also, for embracing with me the challenge of getting out of my comfort zone and developing a thesis around a topic that involved a bit of chemistry and a new software.

Additionally, I thank Engineer Mariana Salama and Professors Maria João Carmesim and Catarina Santos from IPS for all the help with their previous work about porous iron corrosion, which gave rise to the subject of my thesis. To the professors mentioned, I also thank the incredible help with corrosion theory and the guidance provided.

Also, I show my great appreciation to Engineer João Pragana and Professor Ivo Bragança for the help and advice in Laboratório de Tecnologia Mecânica in the experimental tests, and also with the DIC equipment data acquisition.

I thank Professor Augusto Moita de Deus for being always ready to help with his previously acquired knowledge in *COMSOL* software.

At the same time, I show my appreciation to Mister Carlos Farinha for his incredible availability and guidance for the compression specimens machining in Laboratório de Tecnologia Mecânica. Also, I present my gratitude to NOF for machining the tensile specimens.

In addition, I thank Fundação para a Ciência e Tecnologia (FCT) for supporting this thesis through IDMEC, under LAETA project UIDP/50022/2020. The author gratefully acknowledges the funding of the PL 647 project.

I thank all my friends who supported me, shared experiences with me and helped me, somehow, make the choices that brought me here. To the ones that walked with me the IST path, I gratefully thank you your fellowship and for making me feel at home again.

A special thank you to the people in FST Lisboa that helped me work out the engineer in me, and with whom I shared the build of two amazing cars.

Last but not least, the most special thank you to my mother and father for never giving up on me and encouraging me to always be better, to my girlfriend Filipa for her patience and for always cheering me up specially while I was developing the thesis work, and to my family for their caring and for making me who I am today.

Contents

Abstract . . . iii
Resumo . . . iv
Acknowledgements . . . v
List of Tables . . . ix
List of Figures . . . xi
Abbreviations . . . xv

1 Introduction **1**

2 State of the art **3**
2.1 Bone Implants and Grafts . . . 3
2.1.1 Implant materials . . . 5
2.1.1.1 Permanent metals . . . 5
2.1.1.2 Biodegradable metals . . . 7
2.2 Iron applications on implants . . . 8
2.3 Corrosion . . . 23
2.3.1 Electrical conductivity . . . 24
2.3.2 External Electric Potential . . . 24
2.3.3 Polarization curves . . . 25

3 Materials and Methods **28**
3.1 Material characterization . . . 28
3.1.1 Tensile Tests . . . 28
3.1.2 Compression Tests . . . 30
3.1.3 Strain Measurement . . . 31
3.2 Finite Element Modelling of iron degradation . . . 33
3.2.1 Numerical model . . . 35
3.2.1.1 Physics and Study . . . 35
3.2.1.2 Specimen . . . 35
3.2.1.3 Material Properties . . . 36
3.2.1.4 Current Distribution and Boundary Conditions . . . 37
3.2.1.5 Other parameters . . . 38

3.2.1.6 Mesh Creation . . . 39
3.2.2 Sensitivity Analysis . . . 39
3.2.2.1 Mesh Refinement . . . 40
3.2.2.2 Mechanical Properties . . . 41
3.2.2.3 Influence of changes in time . . . 41
3.2.2.4 Sharma and Čapek polarization curves . . . 42
3.2.2.5 External Electric Potential (EEP) boundary condition . . . 42
3.2.2.6 Average Current Density (ACD) boundary condition . . . 42
3.2.2.7 Electrolyte conductivity, κ . . . 42
3.2.2.8 Temperature, T . . . 43
3.2.3 Sample Positioning . . . 43
3.2.4 Electrolyte volume . . . 44
3.2.5 Porous Specimens . . . 44

4 Results and Discussion **46**
4.1 Mechanical Characterization . . . 46
4.1.1 Tensile Tests . . . 46
4.1.2 Compression Tests . . . 49
4.1.3 Principal Strain Plane . . . 53
4.2 Sensitivity Analysis . . . 53
4.2.1 Mesh Refinement . . . 53
4.2.2 Mechanical Properties . . . 55
4.2.3 Influence of changes in time . . . 56
4.2.4 Sharma and Čapek polarization curves . . . 56
4.2.5 External Electric Potential (EEP) boundary condition . . . 57
4.2.6 Average Current Density (ACD) boundary condition . . . 58
4.2.7 Electrolyte conductivity, κ . . . 59
4.2.8 Temperature, T . . . 61
4.2.9 Sensitivity analysis conclusions . . . 61
4.2.10 Sample Positioning . . . 62
4.2.11 Electrolyte volume . . . 63
4.3 Porous Specimens . . . 65
4.3.1 Condition A . . . 66
4.3.2 Condition B . . . 68
4.3.3 Condition C . . . 69
4.3.4 Parameters Confirmation . . . 70

5 Conclusions and Future Work **71**
5.1 Conclusions . . . 71
5.2 Future Work . . . 72

References **74**

Appendix A *COMSOL* tutorial **A.1**

List of Tables

2.1 Types of human bone and their healing period [9]. 3
2.2 Young's modulus of the two types of bone and the most used PM on bone implants. . . . 6
2.3 Mechanical properties and maximum daily intake of zinc, magnesium and iron [32, 64–66]. 8
2.4 Mechanical characteristics of human bone [71]. 9
2.5 Compressive Yield Stress and Ultimate Compressive Strength of the prepared materials [71]. 10
2.6 Properties of Fe-Mn alloys compared to SS316L. Values in parenthesis refer to the specimen properties after it has been subjected to 20% of plastic deformation [77]. 12
2.7 Electrochemical data calculated from the potentiodynamic polarization solution at 37 ° C, adapted from Feng et al. [83]. 15
2.8 Corrosion parameters for RPIS samples in prepared SBF solution at 37 ° C determined using Tafel analysis, adapted from Sharma and Pandey [86]. 17
2.9 Corrosion parameters for TOPIS samples in prepared SBF solution at 37 ° C determined using Tafel analysis, adapted from Sharma and Pandey [86]. 17
2.10 Mechanical properties and weight loss of the SLM produced samples [79]. 19
2.11 Relative cytocompatibility (%) of different iron scaffolds against titanium controls, after 24, 48 and 72 hours [79]. 21
2.12 Specimen dimensions. 22
2.13 Experimental results for 3PB tests of samples before and after immersion in SBF solution: stiffness *K*, adapted from Salama et al. [1]. 23
2.14 E_{eq} and $i_{average}$ from electrochemical analysis [71, 78]. 27

3.1 Polarization curves data [71, 78]. 37
3.2 Mesh elements properties. 39

4.1 Mesh refinement computation times. 54
4.2 Variance of results with the mechanical properties at the 730th day. 55
4.3 Variance of results with little changes in time at the 7th day. 56
4.4 Results with different EEP boundary conditions applied. 57
4.5 Results with different ACD boundary conditions applied (1). 58
4.6 Results with different ACD boundary conditions applied (2). 59

4.7 Results with different κ and EEP boundary condition of -0.6 V. 60
4.8 Results with different κ and EEP boundary condition of -0.57 V. 60
4.9 Results with different temperatures, for different boundary conditions. 61
4.10 Iterated variables to use in *COMSOL*. 62
4.11 Results with EEP boundary condition applied: -0.57 V. 62
4.12 Results with ACD boundary condition applied: 0.0523 A/m^2. 63
4.13 Results with EEP boundary condition applied: -0.57 V. 64
4.14 Results with EEP boundary condition applied: -0.57 V. 65
4.15 Coding used for the three different simulations conditions. 65
4.16 Results of A4_2_20 specimen with EEP and ACD boundary condition. 66
4.17 Results of A4_2_23 specimen with ACD boundary condition: 0.0523 A/m^2. 67
4.18 Results of A4_2_30 specimen with ACD boundary condition: 0.0523 A/m^2. 67
4.19 A4_2_20 specimen: continuous analysis vs. phased analysis. 68
4.20 Results of porous specimen for a 42 days analysis. 69
4.21 Results of A4_2_30 specimen for a 42 days analysis with Finer and Extra Fine meshes. . 70
4.22 Results of A4_2_30 specimen for a 42 days analysis with different boundary conditions applied. 70

List of Figures

2.1 Relationship between mechanical integrity and degradation rate of bone implants during healing process [11]. . . . 4
2.2 Cortical and trabecular bone [44]. . . . 6
2.3 Representative scheme of SPS manufacturing process [73]. . . . 9
2.4 Representative scheme of SHT manufacturing process [74]. . . . 10
2.5 Metabolic activity of L929 cells after 1 day incubation with concentrated and diluted (50% and 25%) extracts of tested samples. According to ISO 10993-5 standard [76], the dashed line indicates the cytotoxicity limit of 70% [71]. . . . 11
2.6 Metabolic activity of L929 cells after 1 day of exposition to the extracts (100% undiluted and 50% diluted extract) compared to the control (sole cultivation medium). Black line indicates the cytotoxicity limit of 70% according to ISO 10993-5 standard [57, 76]. . . . 11
2.7 Relative metabolic activity of 3T3 fibroblast cells in presence of Fe-Mn alloys powders with different manganese content [77]. . . . 12
2.8 Mechanical properties of Fe and Fe-CS composites with different percentages of CS: (a) compressive strength; (b) bending strength [23]. . . . 13
2.9 Degradation rates of pure Fe and Fe-CS composites [23]. . . . 14
2.10 Indenters geometry: (a) Berkovich; (b) Vickers [85]. . . . 14
2.11 Fe-30Mn6Si1Pd-20%NaCl mechanical properties in function of immersion in time: (a) reduced Young's modulus; (b) hardness [83]. . . . 14
2.12 Saos-2 cells during 10 days of culture with conditioned media: (a) Cell viability; (b) cell proliferation [83]. . . . 15
2.13 Designed CAD model of TOPIS samples. In detail, the three levels of porosity with the pore size of 1.0, 1.25 and 1.5 mm [78]. . . . 16
2.14 CAD model of unit cell structures used for preparation of TOPIS samples: (a) cubic; (b) truncated octahedron; (c) pyramid shaped [86]. . . . 16
2.15 Schematic of the selective laser melting process [87]. . . . 18
2.16 Longitudinal and top views of the CAD models of: (a) S0.2; (b) Dense-in; (c) Dense-out; (d) S0.4 [79]. . . . 19
2.17 Mechanical properties of the AM porous iron specimens before and after biodegradation for 28 days: stress-strain curves (a) before biodegradation; (b) after biodegradation [79]. . 20

2.18 Relative cytocompatibility, in percentage, of different iron scaffolds against titanium controls: (a) S0.2; (b) Dense-in; (c) Dense-out; (d) S0.4 [79]. 20
2.19 Iron specimens: (a) Bulk; (b) A4_2_20%; (c) A4_2_23%; (d) A4_2_30% [1]. 21
2.20 Procedure of the experimental corrosion tests in Salama et al. [1]. 22
2.21 Porous iron weight loss as a function of SBF immersion time, in Salama et al. [1]. 22
2.22 Uniform corrosion process of iron, adapted from [89]. 23
2.23 Electrolyte conductivity values in Magyari et al. [92]. 24
2.24 OCP vs. time graphic in Wagener et al. [94]. 24
2.25 Electric circuit to perform an electrochemical analysis [95]. 25
2.26 Sharma and Pandey [78] and Čapek et al. [71] polarization curves. 26
2.27 Representation of the Tafel extrapolation, adapted from [95]. 27

3.1 Tensile specimen (a) Render; (b) Technical drawing. 29
3.2 Tensile test machine. 29
3.3 Compression specimen (a) Render; (b) Technical drawing. 30
3.4 Hydraulic testing machine *Instron SATEC 1200* [100]. 31
3.5 Strain measurement equipment and preparing (a) *Q-400 3D* model from *Dantec Dynamics* [100]; (b) first layer of white spray on tensile specimen; (c) final aspect of painted tensile specimen. 32
3.6 Tensile test DIC system setup (a) schematic representation [100]; (b) system setup in the experimental tests. 32
3.7 Compression test DIC system setup (a) schematic representation [98]; (b) system setup in the experimental tests. 33
3.8 Specimens drawn on Solidworks® (a) bulk specimen; (b) A4_2_20% specimen; (c) A4_2_23% specimen; (d) A4_2_30% specimen. 35
3.9 *COMSOL* model - vertical bulk specimen. 36
3.10 Rules by Fontana [95] applied on the Sharma polarization curve. 36
3.11 New values obtained with Tafel Extrapolation for Average Current Condition (a) Sharma additional $i_{average}$ 1; (b) Sharma additional $i_{average}$ 2; (c) Čapek $i_{average}$. 37
3.12 *COMSOL* - modelling method choice flow chart in *COMSOL* Corrosion Module User's Guide [103]. 38
3.13 Sensitivity analysis scheme. 39
3.14 Local refinement meshes (a) Mesh Quality: Normal (5); (b) Mesh Quality: Fine (6); (c) Mesh Quality: Finer (7); (d) Mesh Quality: Extra Fine (8); (e) Mesh Quality: Extremely Fine (9). 40
3.15 Local refinement entire meshes (a) Mesh Quality: Normal (5); (b) Mesh Quality: Finer (7); (c) Mesh Quality: Extremely Fine (9). 40

3.16 Global refinement meshes (a) Mesh Quality: Extremely Coarse (1); (b) Mesh Quality: Extra Coarse (2); (c) Mesh Quality: Coarser (3); (d) Mesh Quality: Coarse (4); (e) Mesh Quality: Normal (5); (f) Mesh Quality: Fine (6); (g) Mesh Quality: Finer (7); (h) Mesh Quality: Extra Fine (8). 41
3.17 Electrolyte conductivity values. Adapted from Magyari et al. [92]. 43
3.18 Specimen positioning in the electrolyte recipient (a) Vertical; (b) Inclined; (c) Horizontal. . 44
3.19 Variations in the electrolyte volume (a) Smaller recipient, $Volume$ = 23556 mm^3; (b) Original recipient, $Volume$ = 32490 mm^3; (c) Bigger recipient, $Volume$ = 42786 mm^3. . . 44
3.20 Porous specimens' models on *COMSOL* (a) A4_2_20 specimen; (b) A4_2_23 specimen; (c) A4_2_30 specimen. 45
3.21 The three different methods to analyse the porous specimens. 45

4.1 Tensile specimen after being tested. 47
4.2 Force-displacement evolution for the two tensile specimens. 47
4.3 True Stress-True Strain evolution for the two tensile specimens. 48
4.4 Strain data acquired with DIC in several moments of the tensile test, 2D results: (a) beginning of the test; (b) halfway through the test, before losing data of half of the specimen; (c) after losing data of half of the specimen; (d) end of testing. 48
4.5 Strain data acquired with DIC in several moments of the tensile test, 3D results: (a) beginning of the test; (b) halfway through the test, before losing data of half of the specimen; (c) after losing data of half of the specimen; (d) end of testing. 49
4.6 Compression specimens after being tested. 49
4.7 Elastic recovery displacement-force evolution. 50
4.8 Force-displacement evolution for the compression C1 specimen, with and without the displacement corrected. 50
4.9 Force-corrected displacement evolution for the three compression specimens. 51
4.10 True Stress-True Strain evaluation for the three compression specimens. 51
4.11 Approximation of a Ludwik-Hollomon curve to the compression tests results. 52
4.12 Strain data acquired with DIC in several moments of the compression test: (a) beginning of the test; (b) halfway through the test; (c) end of testing. 52
4.13 Principal strain plane from the strains measured in the tensile and compression tests. . . 53
4.14 Mesh refinement results graphic. 54
4.15 Mesh from Global Refinement with mesh quality index *Finer* (7). 55
4.16 Results of mass change variation in time, with ACD and EEP boundary conditions applied in Sharma and Čapek polarization curves. 56
4.17 EEP boundary conditions results (a) $\phi_{s,ext} : -0.68V$; (b) $\phi_{s,ext} : -0.636V$; (c) $\phi_{s,ext} : -0.62V$; (d) $\phi_{s,ext} : -0.6V$; (e) $\phi_{s,ext} : -0.57V$. 57
4.18 ACD boundary conditions results (1) (a) $i_{average} : 0.1153$ A/m^2; (b) $i_{average} : 0.1053$ A/m^2; (c) $i_{average} : 0.1$ A/m^2; (d) $i_{average} : 0.01$ A/m^2; (e) $i_{average} : 0.062$ A/m^2. 58

4.19 ACD boundary conditions results(2) (a) $i_{average}$: 0.0523 A/m^2; (b) $i_{average}$: 0.0150 A/m^2. . 59
4.20 *COMSOL* results with EEP boundary condition of -0.57 V and κ of 2.356 S/m. 60
4.21 *COMSOL* results with EEP boundary condition of -0.57 V, κ of 2.356 S/m and 37 $^\circ$C. . . 61
4.22 Sensitivity analysis scheme completed. 62
4.23 Results with different ways of positioning the specimen (a) legend; (b) vertical; (c) inclined; (d) horizontal. 63
4.24 Best positioning to be used for the bulk specimen model. 64
4.25 *COMSOL* models for the porous specimens (a) A4_2_20; (b) A4_2_23; (c) A4_2_30. . . 65
4.26 *COMSOL* results at 28th day for the specimen A4_2_20 (a) $\phi_{s,ext} = -0.6$ V; (b) $\phi_{s,ext} = -0.57$ V; (c) $i_{average} = 0.1153$ A/m^2; (d) $i_{average} = 0.0523$ A/m^2. 66
4.27 *COMSOL* results at 28th day (a) legend; (b) A4_2_23 specimen; (c) A4_2_30 specimen. . 67
4.28 *COMSOL* results for the phased analysis (a) results at the 7th day; (b) results at the 14th day; (c) results at the 21th day; (d) results at the 28th day. 68
4.29 *COMSOL* results at 42th day (a) legend; (b) A4_2_20 specimen; (c) A4_2_23 specimen; (d) A4_2_30 specimen. 69

Abbreviations

η	Activation overpotential
$\overline{\rho}$	Relative density
$\phi_{s,ext}$	Voltage applied on the specimen boundaries
E	Applied potential
E_{eq}	Corrosion potential
i	Current
$i_{average}$	Average current density
P	Porosity
R_p	Corrosion resistance
T	Temperature
Y	Young's modulus
Y_r	Reduced Young's modulus
3PB	Three-point bending
ϕ	Electric Potential
ACD	Average Current Density
AM	Addictive Manufacturing
BM	Biodegradable metals
CAD	Computer-aided design
CS	Calcium Silicate
DIC	Digital Image Correlation
e	Engineering Strain
EEP	External Electric Potential

FEA	Finite Element Analysis
FEM	Finite Element Method
HA	Hydroxyapatite
IPS	Instituto Politécnico de Setúbal
IST	Instituto Superior Técnico
PLA	Polylatic acid
PLA/HA	Polylatic acid/hydroxyapatite
PLA/TCP	Polylatic acid/β-tricalcium phosphate
PM	Permanent metals
RPIS	Random porous iron scaffolds
S	Engineering Stress
SBF	Simulated Body Fluid
SCE	Saturated Calomel Electrode
SHT	Space holder technique
SLM	Selective Laser Melting
SPS	Spark plasma sintering
TCP	β-tricalcium phosphate
TOPIS	Topologically ordered porous iron scaffolds

Chapter 1

Introduction

Bones in the human body are part of the skeleton that serves as a structure to hold the body. The relation of the bones to the rest of the body (namely nervous, digestive, respiratory and cardiovascular systems and the muscles voluntarily activated) shows that the skeleton has three different functions: support, protection and motion. Comparing the human skeleton to other mammals, the distinctive feature is the erect posture that, while it has brought the benefit of freeing the arms for a wide variety of functions, it brought along some mechanical problems, one of the most serious being the weight bearing [2]. Also, the occurrence of bone fractures is rising due to several causes like osteoporosis and increased life expectancy, being both dangerous when falls happen. Falls are nowadays the second main cause of unintentional injury deaths all over the world, where on an annual basis approximately 684000 humans die from falls and 37.3 million are serious enough to need medical assistance. Concerning specifically children, in the People's Republic of China, for every death due to a fall, there are four cases of permanent disability, thirteen cases requiring hospitalization for more than ten days, 24 cases requiring hospitalization for one to nine days, and 690 cases seeking medical care or missing work or school [3].

When the defect in the bone is irreparable only by biological processes within the human body, any medical intervention is needed so the bone can regenerate itself back to its healthy condition. Nowadays, the implants used to help regenerate the bone are usually made of permanent metals (PM): bio-inert metals that do not trigger any primary response in the host body. However, these type of metals have associated disadvantages that makes them options that are not 100% ideal, such as the appearance of long-term inflammation and patient discomfort. So, for about 20 years, research has been about biodegradable metals (BM) and finding a way of turning them the best option when it comes to bone implants. Among BM there is iron (Fe), one of the most promising materials for bone fixation. The difficulty of BM is understanding how they will degrade in the human body and for how long. Taking little time would be dangerous, as the bone implant would not perform its task for long enough and would put the recovery of the bone in question. Taking too long would mean that the BM was almost as a PM, and that the corrosion rate of this biodegradable metal could be improved.

So, apart from investigating about what material offers better performance in medical implants and

testing samples, the finite element method (FEM) can be applied in corrosion problems. Using it, as long as the models are calibrated for real experimental conditions, makes possible to predict how the corrosion of the implant will occur, reducing the amount of time, material and capital investment applied on the investigations, with equal or even better results.

In this context, previous investigation on iron samples had already been made experimentally in Instituto Superior Técnico (IST) and Instituto Politécnico de Setúbal (IPS) by Salama et al. [1]. This work had the purpose to study and evaluate the degradation evolution and mechanical properties of porous iron samples with porosities varying between 20 and 30%, having a bulk specimen as control sample. The Fe samples have undergone chemical degradation by immersion in simulated body fluid (SBF) and it was found that the topology of porous samples had a strong influence on the iron properties.

The aim of this dissertation is to develop a numerical model for the iron corrosion behaviour in SBF, and it is validated through the previous experimental work performed by Salama et al. [1]. Prior to Finite Element Analysis (FEA), a mechanical characterization of iron was performed in order to evaluate the tensile and compression properties of the material, needed as input in the FEA software.

The present dissertation is structured as follows:

Chapter 1 introduces the motivation and objectives of the dissertation, highlighting the up-to-date and upcoming problems related to bone damage and subsequent regeneration. It also features previous experiments performed by IST and IPS researchers, which is the basis of this dissertation.

Chapter 2 introduces the importance of having reliable solutions when it comes to bone implants and the materials used to do so, with the respective advantages and disadvantages. This chapter also provides information about the results in a recent paper by Salama et al. [1], which was used as a reference for the numerical simulations performed in this dissertation. It is also presented different results obtained with topologically optimized bone implants, iron-alloys and porous iron. Lastly, a literature review about the corrosion process and the variables involved is shown.

In Chapter 3, the materials and methods used are indicated, presenting the laboratory equipment used and what methods were applied to characterize the mechanical behaviour of iron samples. An introduction will be made to the Finite Element software *COMSOL* that was used to numerically analyse the iron corrosion. A sensitivity analysis of the created models is also performed with a simple specimen, due to the fact that this specimen is simpler than the porous ones.

Chapter 4 highlights the major findings concerning the experimental tests and simulations introduced on Chapter 3, involving also some conclusions about the several results obtained.

Finally, in Chapter 5, the final conclusions about the work performed on this dissertation are drawn. Additionally, some remarks for future research are also presented.

Chapter 2

State of the art

2.1 Bone Implants and Grafts

Bones are a complex tissue that constantly goes through dynamic biological reconstruction. Specifically, there is a process where mature bone is regularly being replaced by new one in order to maintain a healthy homeostasis, being this the characteristic that makes the bone able to remodel itself to repair when damaged. Nevertheless, when the defect surpasses a critical size (if a fracture is greater than 30 mm), bone will not heal on its own [4]. Consequently, any kind of medical intervention is needed so that the bone is helped to eliminate the defect [5, 6], and this surgical trauma (for instance, from an extraneous bone grafting) can trigger the initiation of bone regeneration [7]. The way that the bone defect is treated will depend on the patient age, health and the dimensions and place of the damages [8]. The bone regeneration rate also relays on these factors, and table 2.1 demonstrates the renewal time for different types of human bone.

Table 2.1: Types of human bone and their healing period [9].

Type of bone	Healing period (Weeks)
Fingers	4-8
Clavicle	5-7
Scaphoid	>10
Humerus	5-8
Distal radius	3-4
Radius and Ulna	8-12
Pelvis	6-10
Femur	8-14
Neck of Femur	12-24
Tibia	8-12
Calcaneus	6
Toes	6-8

As an example, in a critical zone where the bone has load-bearing responsibilities, there is an imperative medical need for bone grafts with initial strong mechanical properties [8] of, at least, bone-like mechanical properties to rectify the damage [10]. The figure 2.1 shows the evolution of mechanical integrity and corrosion that a bone implant should have.

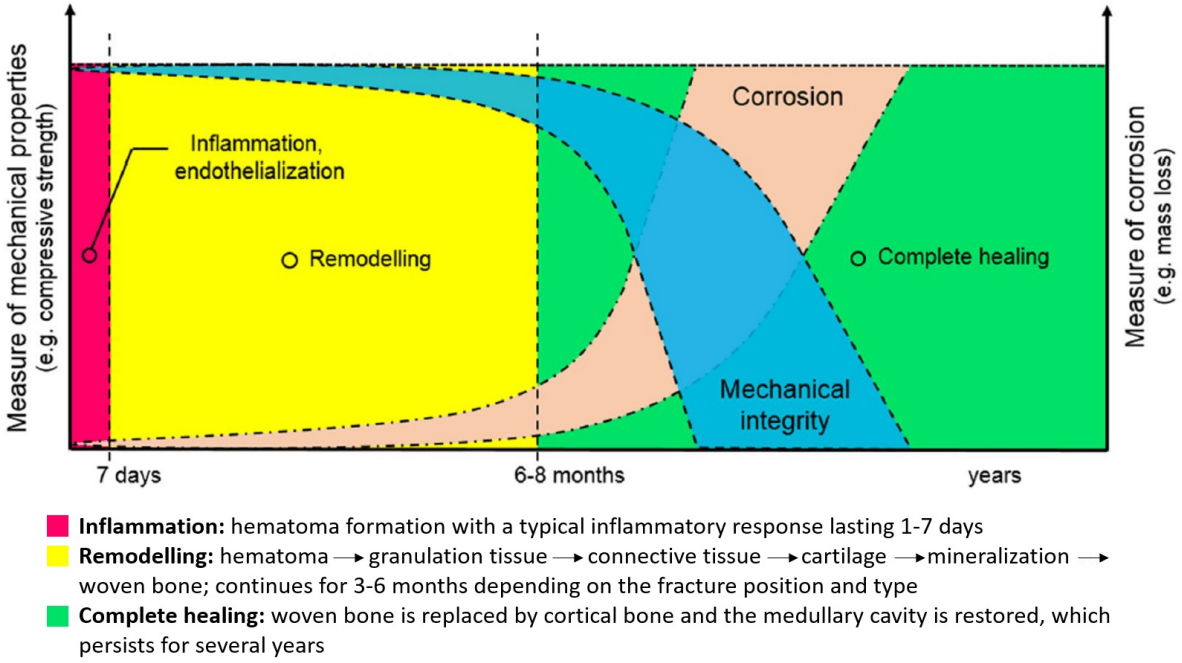

Figure 2.1: Relationship between mechanical integrity and degradation rate of bone implants during healing process [11].

The development of reliable bone implants is a major concern due to the fact that the occurrence of bone fractures is rising because of several causes, like lack of calcium [12] and increase in the ageing population. Also, according to International Osteoporosis Foundation, there are more than 8.9 million fractures every year around the world. It is expected that, around 2050, hip fracture will increase 310% and 240% respectively in men and in women, when in contrast to the rates in 1990 [9]. So, responding to these developments, there is a need to increase the life quality of the patients that need extreme bone recovery. To provide an adaptable fit anatomically and meet the requirements of each patient, perfect bone implants for fixing bones with load-bearing functionalities should:

1. Fully fit with the complex morphology of the bone damaged zone [13–15];
2. Have suchlike mechanical properties with the patient tissues in order to prevent stress-shielding [16–18];
3. Bear *in vivo* biodegradable capacity, at an intermediate rate, to hold the mechanical support functions while the whole process of regeneration takes part (involving implant deterioration and bone recovery) [19–21], decrease the chance of infection from long-term implant and reduce the chance of new surgery [22];

4. Possess a way of enhancing nutrient exchange and vascularization to stimulate the bone regeneration [13, 20, 23–26];

5. Biocompatible to prevent infections, and ideally osteoconductive [27].

Although there is an extensive research on materials used in load-bearing or permanent implants, the same is not true for temporary implants where studies are rare, such as the use of this type of implants to repair bone damage.

Biocompatibility is the ability of being at one with the host body, without causing any harm on it [28]. As already said, a bone scaffold or implant must be biocompatible and non-toxic: cells must stick to the scaffold, normally operate, breed, divide and generate new matrix [29–31]. Another feature that comes from the biocompatibility is the bioactivity, which describes the capability of interacting with the neighbouring organs and tissues [27].

Biodegradable functionality is important to enable the formation of tissue while the degradation of the metallic scaffold occurs, being the products of this process non-toxic and expelled without hazardous reaction to the host body. The biodegradation is caused by corrosion processes, indicating accurately the electrochemical mechanisms of metal wear that begins when the metallic implant is placed in contact with the human/animal body fluid (*in vivo*), or its substitute (*in vitro*) [32], causing variation of the mechanical strength. Metals with high biodegradation rate tend to be applied in low load bearing applications because the load must be progressively passed to the recovering bone [33, 34], which would be critical for high load bearing implants.

2.1.1 Implant materials

Nowadays, several different materials are being researched to use in bone implants from the family of metals, polymers and ceramics. The latter two groups have revealed adequate biocompatibility and biodegradability, while also stimulated bone regeneration [35]. Anyway, either polymers, ceramics or composites have, usually, insufficient mechanical properties to fix a load-bearing bone [36]. However, recent studies from Backes et al. [37] with 3D specimens made from polylatic acid (PLA), polylatic acid/hydroxyapatite (PLA/HA) and polylatic acid-β-tricalcium phosphate (PLA/TCP) concluded that these materials had mechanical properties adequate for bone graft and bone tissue engineering, while also being biocompatible. Regarding metals, there are two large groups: permanent or non-biodegradable metals (PM) and biodegradable or absorbable metallic materials (BM), according to ASTM-F3160-21 [38], standard guide for metallurgical characterization of absorbable metallic materials for medical implants. Metals turn out to be the better option for bone implants, since they are more easily found on Earth and are very necessary for the functioning of the human body.

2.1.1.1 Permanent metals

PM or bio-inert bone implants, as the name suggests, are implants that do not trigger any corrosion reaction on the host body. These are usually made of tantalum, cobalt-chromium-molybdenum

(CoCrMo), Ti6Al4V (one of the most used Ti alloys for medical implants) and stainless steel (SS). All of them cause stress shielding or stress protection, an effect that happens because although this type of implant stabilizes the fracture, allows weight bearing and patient mobility, the much higher stiffness leads to bone loss as a result of reduced physiologic loading of the bone [39–41]. Specifically, what happens is excessive bone resorption, the process by which the bones are absorbed and broken down by the body [42].

There are two types of bone: cortical (or compact), and trabecular (or cancelous). Cortical bone is a dense tissue containing less than 10% soft tissue and forms the external layer of the bones, while trabecular bone is spongy and is usually found in the interior of the bones [43]. Both types are represented in figure 2.2.

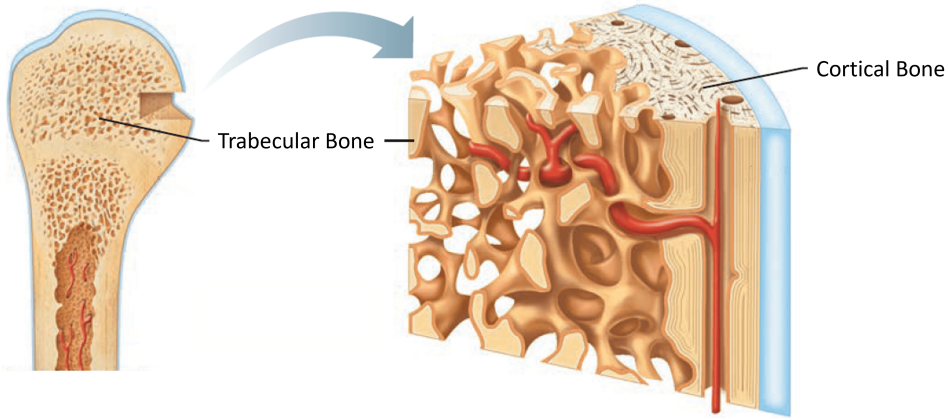

Figure 2.2: Cortical and trabecular bone [44].

The Young's modulus, Y, of the metals usually used in implants and the two types of bone are represented in table 2.2.

Table 2.2: Young's modulus of the two types of bone and the most used PM on bone implants.

Type of material	Young's modulus (GPa)
Cortical bone	3 - 30
Trabecular bone	0.02 - 2
Tantalum	185
CoCrMo alloys	210
Ti6Al4V	110
Stainless Steel	190

So, to prevent the stress shielding effect, when using the bulk permanent metals, that are simple iron specimens with a solid shape, the equivalent Y and yield stress need to be reduced. For example, one of the possible solutions is using implants with porosity [45]. Also, from another point of view, the permanent nature of these metals may require a second surgery for the implant to be removed. This is a necessity because sometimes, when it is left in the body for long periods of time, it can start releasing toxic ions which conduct to bone atrophy and cell death [46], become obstacles to finish the regeneration

of the damaged bone like in the case of teenager bones that are still developing [47], or because it simply becomes uncomfortable for the host.

2.1.1.2 Biodegradable metals

BM implants are made from metals that progressively corrode or degrade in the body, causing an appropriate response in the patient to the implantation and resulting corrosion [27]. During this process, the initial mechanical properties (suitable for load-bearing) should decline over time, so that the bone can withstand the stresses without being damaged, and in the end the implant can be completely corroded by the host body. The essential metallic macronutrients that can be used on BM implants and have been mostly researched are zinc (Zn), magnesium (Mg) and iron (Fe) [32, 48].

Zinc has some advantages when used as a material for bone implants. It has a suitable corrosion rate and biocompatible corrosion products offering a good level of biocompatibility. Also, it is important in multiple physiological functions, like being necessary for the function of hundreds of enzymes involved in diverse physiological processes, such as wound healing and brain development. On the other hand, Zn also owns many issues. Its mechanical properties are rather lower than the other BM, affecting the ability to detain load-bearing functions. In addition, it is less biocompatible than Mg and similar to Fe, but the faster corrosion than Fe makes it more susceptible to cause cytotoxicity in the human cells, and the excess of zinc is neurotoxic and can impair immune function and delay bone development [49, 50].

Concerning magnesium, its benefits are related with having density and elastic modulus similar to the bone [51], promoting osteogenesis [52] and presenting very low levels of cytotoxicity [32]. However, it also has some downsides: 1) it may have traditional manufacturing problems due to its reduced formability at room temperature [53]; 2) it compromises the bone recovery having a large corrosion rate, also in conjunction with hydrogen gas release, that only below a certain concentration is tolerable and does not affect the host [54]; 3) the very low Y when compared to Zn and Fe is an advantage but it also is problematic, as the large corrosion rate means that the already reduced mechanical properties will decay rapidly [32].

Finally, as for iron, this metal has the higher hardness, strength and ductility of these three BM, allowing maintaining proper mechanical properties. Also, iron is very abundant in nature and its homeostasis (condition of optimal functioning for the organism) is fundamental for bone recovery [55]. Investigations concluded that iron has none or little toxicity *in vitro* [56, 57] and *in vivo* [58, 59], and proper uptake can aid in the formation of osteoblasts, the cells that synthesize bone [60, 61], and induce platelet activation, essential for the early healing phase of bone regeneration [62]. However, iron has the disadvantages of having a too slow corrosion rate on the bulk form, its elastic modulus is far superior than that of bone (which can cause stress shielding), and may prohibit magnetic resonance imaging because it is ferromagnetic [63], but negligible if the implant mass is very small.

In table 2.3 it is compared some properties of the three BM presented.

Table 2.3: Mechanical properties and maximum daily intake of zinc, magnesium and iron [32, 64–66].

	Zinc (Zn)	Magnesium (Mg)	Iron (Fe)
Youngs' Modulus (Gpa)	96.5	44	200
Tensile Yield Stress (MPa)	-	21	50
Ultimate Tensile Strength (MPa)	37	90	540
Maximum Daily Intake (mg)	15	700	10-20

So, when it comes to develop Fe bone implants, the mechanical properties need to be adjusted trying to match the ones found in the damaged bone, and the degradation rate must be sufficient in order to not affect the host health. The mechanical properties essential in bone engineering involve tensile strength, elastic modulus, elongation percentage, fracture toughness and fatigue limit resistance. As for the corrosion behaviour, the potentiodynamic polarization curves from the electrochemical tests (immersing the iron in SBF) and the superficial area of the implant is what governs the rate of degradation that the iron will own. Finding a way of adapting all these properties of an iron bone implant reduces the chances of having problems associated to an inappropriate corrosion rate (being close to a PM or too fast, like Mg), stress shielding, osteopenia surgery-derived and consequent re-fracture [29, 30, 67, 68]. Some of the existing options to turn iron into the perfect material for bone implants are using topology optimization, including porosity or alloying with other metals.

Several methods can be used to increase the degradation rate of iron, as it is the main problem in using iron for bone implants. An adequate lifespan for biodegradable implants should be between several months and several years [69], that would translate in a corrosion rate of 0.25-1 mm/year or a lifespan of 0.5-2 years, for a porous scaffold with an interconnected porous structure and a wall thickness of approximately 500 μm, suffering uniform corrosion. Although, it was verified in Schinhammer et al. [70] and Čapek et al. [57] that pure iron has a corrosion rate of approximately 0.1 mm/year. So, to increase the degradation rate of Fe several different methods could be carried out, such as adding alloying elements, modifying the surface properties, and using porous structures. When entering the field of porous structures, the relative density and the definition of porosity need to be introduced, and they are related to each other. The relative density links the weight of a certain part or material to the weight it would have if it was completely solid, and it is usually represented by $\overline{\rho}$. Porosity, P, is defined by the relative density, with the following equation:

$$P = 100 - \overline{\rho} \quad (\%) \tag{2.1}$$

2.2 Iron applications on implants

In this section, some solutions developed in recent years for the high mechanical properties and slow corrosion rate of pure iron will be presented. The common objective in the alternatives met was, generally, to meet similar mechanical properties to the ones of bone present in table 2.4.

Table 2.4: Mechanical characteristics of human bone [71].

Cortical bone			
Density/g·cm^{-3}		~1.5–2	
Porosity/%		~3–12	
	Load direction	Strength/MPa	Modulus of elasticity/GPa
Compressive properties	Longitudinal	~190–245	~14–28
	Transverse	~30–170	
Tensile properties	Longitudinal	~130–190	~7–25
	Transverse	~40–60	
Trabecular bone			
Density/g·cm^{-3}		0.2–0.6	
Porosity/%		~30–95	
	Strength/MPa		Modulus of elasticity/GPa
Compressive properties	~1–12	~0.1–0.4	
Tensile properties	~2	~6–14	

Regarding the choice of using metal alloys, Čapek et al. [71] proved that alloying Fe with paladium (Pd) influences the corrosion behaviour, enhancing the corrosion rate of iron-based alloys. The alloy developed, FePd2, was produced by three different processes: casting, mechanical alloying and spark plasma sintering (SPS), and mechanical alloying and space holder technique (SHT).

The SPS procedure is a pressure-assisted process where the powder samples are loaded in an electrically conducting die and sintered under a uniaxial pressure, where it is applied a high-intensity, low-voltage pulsed current. It makes possible sintering at low temperatures and in short periods, by charging the intervals between powder particles with electrical energy and effectively applying a high-temperature spark plasma [72]. A representative scheme of the process is presented in figure 2.3.

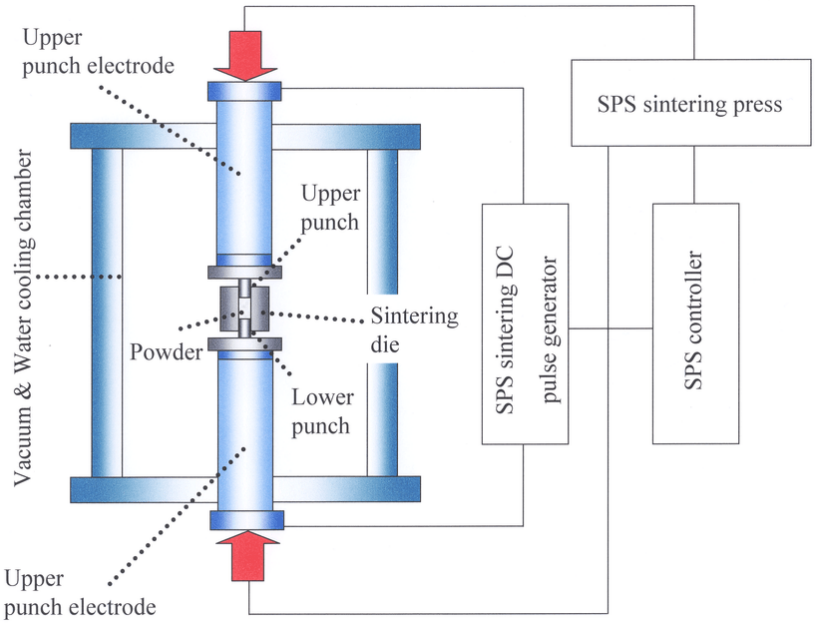

Figure 2.3: Representative scheme of SPS manufacturing process [73].

SHT is a process used to achieve high levels of porosities in a part. It is a simple strategy where the space holders are mixed with the metal powder and then are pressed, and the process may be cold or hot. It is important that the space holders do not react or change during the process, and they must withstand without deforming the pressures applied during the process. Finally, the space holders are

removed, leaving open interconnected pores, and after that the resulting porous material goes through a furnace sintering [74]. A representative scheme of the process is presented in figure 2.4.

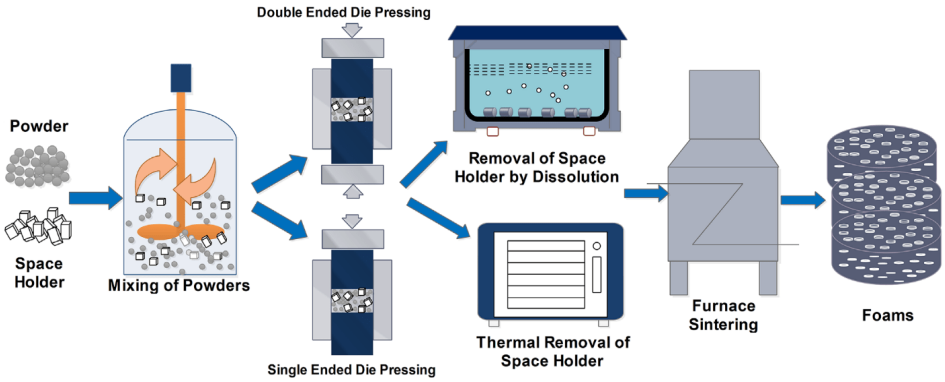

Figure 2.4: Representative scheme of SHT manufacturing process [74].

The mechanical properties obtained in Čapek et al. [71] are presented in table 2.5.

Table 2.5: Compressive Yield Stress and Ultimate Compressive Strength of the prepared materials [71].

	Compressive Yield Stress (MPa)	Ultimate Compressive Strength (MPa)
Casted Fe	73.0 ± 4.5	-
Casted FePd2	279.4 ± 5.7	-
SPS Fe	765.4 ± 23.2	-
SPS FePd2	845.8 ± 35.3	-
Highly porous Fe	10.1 ± 2.1	12.0 ± 2.4
Highly porous FePfd2	14.7 ± 1.6	20.8 ± 2.6

The last process identified was the one that presented higher porosity, therefore it was where the lowest mechanical properties were found, having compressive properties similar to the human trabecular bone, found on table 2.4. The low mechanical properties can be explained by the fact that the pores acted as stress concentrators. Also, the corrosion rates obtained with the SHT process were the highest of the three different methods, explained by the large contact area between the materials and the corrosion environment, being approximately 0.7-1.2 mm/year.

Čapek et al. [71] also studies the cytotoxicity of the developed alloys *in vitro*, that is when a substance or process results in cell damage or cell death. In this study by Čapek et al. [71], the cytotoxicity is evaluated measuring the metabolic activity of L929 cells that are mouse fibroblasts, used for the testing of cytotoxic properties due to their reproducible growth rates and biological responses. These cells are also recommended by international standards for the testing of medical devices on account of the ease to control cell culture conditions [75]. According to ISO 10993-5 standard [76] if the metabolic activity is above the limit of 70% the substance is considered cytocompatible, otherwise it is considered cytotoxic.

In Čapek et al. [71] it was verified that the cast alloys were not cytotoxic, but undiluted extracts of the highly porous FePd2 alloy created with SPS and SHT processes presented cytotoxicity due to the much higher corrosion rates. However, this alloy could be tolerated *in vivo* due to the fact that iron and its alloys present much lower corrosion rates in this condition when compared to *in vitro*. Moreover, the

authors measured the concentration of Fe and Pd in the extracts, and the concentration of Paladium was negligible when compared to that of iron concluding that if there was cytotoxicity, it would be caused by Fe. The results of the cytotoxicity tests are presented in figure 2.5.

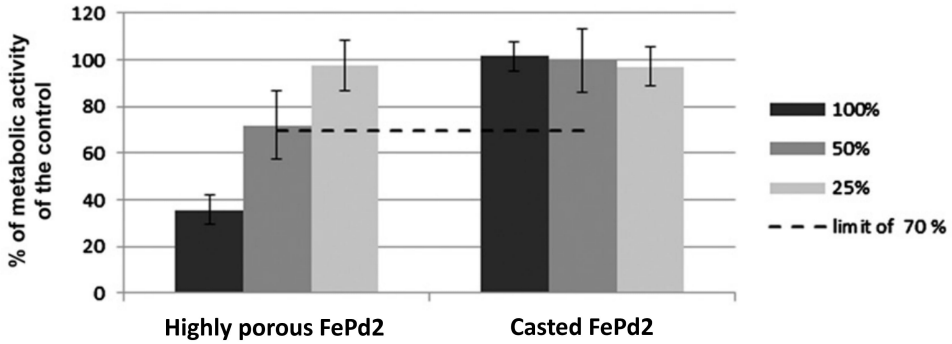

Figure 2.5: Metabolic activity of L929 cells after 1 day incubation with concentrated and diluted (50% and 25%) extracts of tested samples. According to ISO 10993-5 standard [76], the dashed line indicates the cytotoxicity limit of 70% [71].

A previous work by the same authors [57] studied the cytotoxicity of pure Fe while studying the cytotoxicity of Fe-Mn alloys and concluded that pure iron is non-toxic, as the metabolic activity of L929 cells in Fe extract was the same as in the control (sole cultivation medium). This metabolic activity test proves that FePd2 alloy would not cause cytotoxicity due to iron concentrations. The cytotoxicity study in Čapek et al. [57] is presented in figure 2.6.

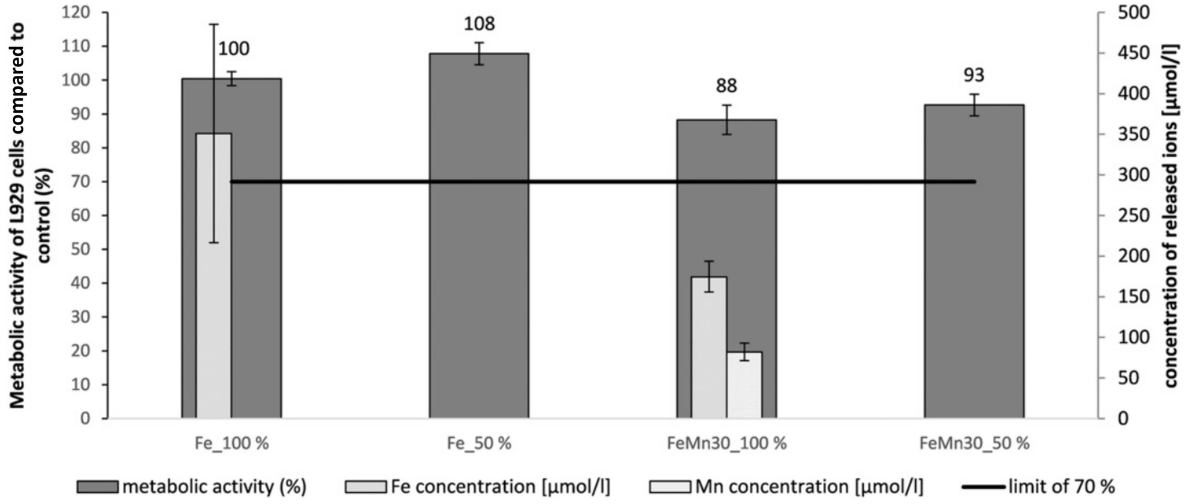

Figure 2.6: Metabolic activity of L929 cells after 1 day of exposition to the extracts (100% undiluted and 50% diluted extract) compared to the control (sole cultivation medium). Black line indicates the cytotoxicity limit of 70% according to ISO 10993-5 standard [57, 76].

Resuming, highly porous FePd2 produced with SHT was concluded to be a worthwhile alloy to use in bone augmentations due to the promising corrosion rate, as an implant with a diameter of 5 mm would completely degrade after about five years. Using the SPS technology could be also a possibility, because while the specimens possessed a lower corrosion rate, the implants could be thinner due to the superior mechanical properties and so the degradation rate could be sufficient.

Alloying iron with manganese (Mn) also influences the corrosion behaviour and would decrease the corrosion potential of iron, enhancing the corrosion rate in dynamic environments, where the conditions of a human coronary artery with blood running are simulated [71]. Hermawan et al. [77] produced, via a powder metallurgy route followed by cold rolling and resintering cycles, four different Fe-based alloys with 20-35 wt.% manganese: Fe20Mn, Fe25Mn, Fe30Mn and Fe35Mn. These alloys corroded at an average rate up to approximately 520 μm/year, about two times the corrosion rate of pure iron, that is 220-240 μm/year. Also, table 2.6 shows the mechanical properties of these specimens produced compared to the properties of the stainless steel SS316L, the reference material for coronary stents.

Table 2.6: Properties of Fe-Mn alloys compared to SS316L. Values in parenthesis refer to the specimen properties after it has been subjected to 20% of plastic deformation [77].

Material	Nominal main composition (wt.%)	Phase at T_{room}	Magnetic susceptibility[a] ($\mu m^3\ kg^{-1}$)	Yield (0.2%) strength (MPa)	Ultimate strength (MPa)	Maximum elongation (%)
Fe20Mn	20 Mn	$\gamma + \varepsilon$	0.2 (1.1)	420	700	8
Fe25Mn	25 Mn	$\gamma + \varepsilon$	0.2 (0.2)	360	720	5
Fe30Mn	30 Mn	γ	0.2 (0.2)	240	520	20
Fe35Mn	35 Mn	γ	0.2 (0.2)	230	430	30
SS316L	18 Cr, 14 Ni	γ	0.5 (1.7)	190	490	40

The table 2.6 also presents the magnetic susceptibility of the iron-alloys and stainless steel. The magnetic susceptibility is the magnetic response to a magnetic field of a certain substance, and can lead to signal loss and local magnetic field inhomogeneities. The alloys possess an antiferromagnetic behaviour, giving the same non-magnetic nature as that of SS316L, thus there would no longer exist the problem of iron implants prohibiting magnetic resonance imaging.

Lastly, cell viability tests were performed to analyse the cytotoxicity levels of the alloys developed, but this time with 3T3 fibroblast cells (an alternative to L292 cells, with the same principles), and are represented on figure 2.7. The variation of the manganese quantity in Fe-Mn alloys did not influence much the relative metabolic activity, probably related to the fact that cell viability test only lasted 48 hours.

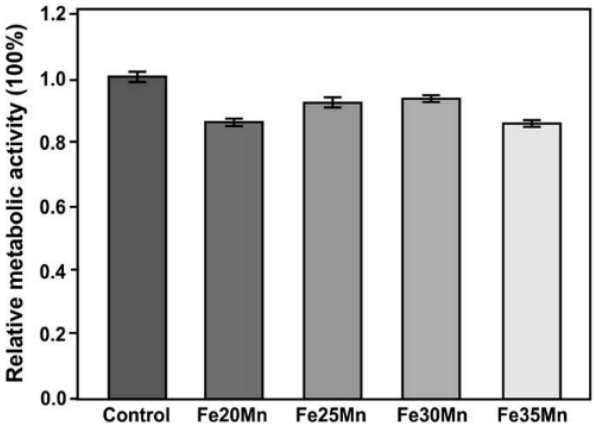

Figure 2.7: Relative metabolic activity of 3T3 fibroblast cells in presence of Fe-Mn alloys powders with different manganese content [77].

To summarize, the Fe-Mn alloys developed by Hermawan et al. [77] degraded approximately two times faster than pure iron, while also were cytocompatible as the iron and manganese released to the

solution was reduced and did not affect drastically the metabolic activity. So, it was concluded that the study demonstrates the potentiality of Fe–Mn alloys to be a BM.

When it comes to reduce the degradation rate and mechanical properties of iron, several researches showed that using topology optimization and porous structures obtained good results [1, 23, 78–80].

Using topological optimization of additively manufactured (AM) porous biomaterials can replicate the mechanical properties of bone. Doing so, the cell proliferation and differentiation are facilitated, while enhancing regeneration of the bone tissue. Recent studies shown that the bone substitutes must exhibit high porosity levels in order to facilitate cell viability and nutrient perfusion.

Wang et al. [23] developed an iron-matrix composite with calcium silicate (CS) bioceramic as the reinforcing phase using powder metallurgy processes. This bioceramic was the one chosen amongst other calcium phosphate-based bioceramics like HA and TCP because CS has superior biodegradability and bioactivity and it has the simplest chemical composition of the three.

Comparing to pure iron, the composites possessed decreased compressive and bending strengths as represented in figure 2.8. The decrease in the compressive strengths can be due to the brittle nature of CS and its large amounts in the composite.

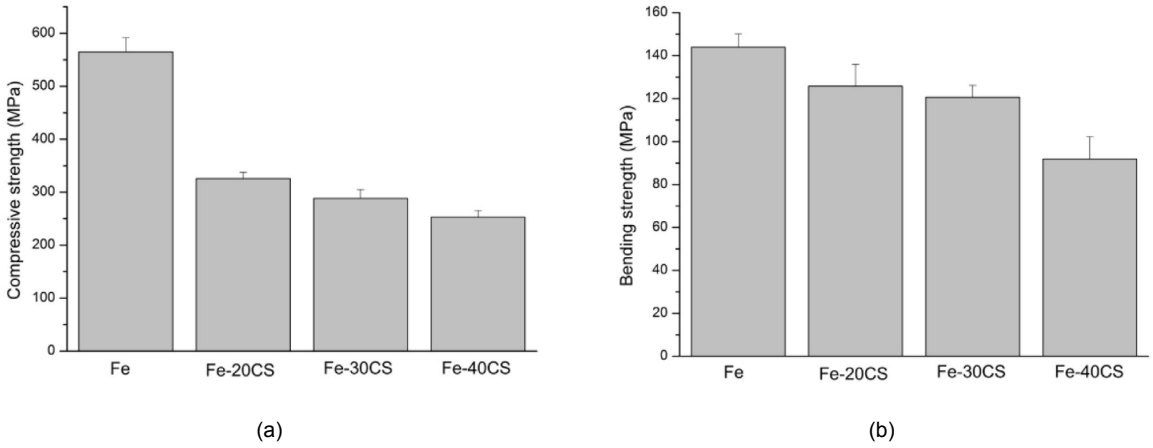

Figure 2.8: Mechanical properties of Fe and Fe-CS composites with different percentages of CS: (a) compressive strength; (b) bending strength [23].

In human compact bone the compressive strength is in the range of 130 to 240 MPa [81] and the bending strength is from 103.5 to 225.0 MPa [82], meaning that some of the composites developed are adequate to repair bone damage in load-bearing locations. Namely, Fe-20CS and Fe-30CS are ideal for this application because their compressive strength and bending strength are greater than that of bone.

Regarding the corrosion behaviour, figure 2.9 represents the degradation rates of Fe-CS composites compared with pure Fe after an immersion test in SBF. Both type of materials kept the structural integrity over the whole period after one month. For the Fe-40CS composite, the degradation rate was almost 8 times that of iron, however this type of specimen should not be used to the lack of mechanical properties. So the Fe-30CS composite was the iron-alloy that shown a better performance for bone implants, since it is the one with sufficient mechanical properties and higher corrosion rate.

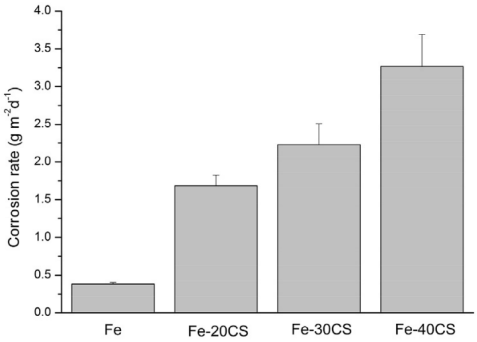

Figure 2.9: Degradation rates of pure Fe and Fe-CS composites [23].

These Fe-CS composites also shown good cytocompatibility behaviour, as all the specimens supported the proliferation of cells, and Fe-20CS even exhibited a higher stimulatory effect than pure Fe.

Feng et al. [83] developed porous Fe-30Mn6Si1Pd alloys with different weight percentages of NaCl (none, 10%, 20% or 40%) to obtain different levels of porosity. The mechanical properties of the alloys before and after being immersed were measured using nanoidentation with a Berkovich indenter, an adequate technique to obtain mechanical properties of bulk materials and films, including porous. Rother et al. [84] compared the Berkovich indenter with the more known Vickers indenter experimentally with different materials, specifically silver, aluminium, gold, nickel and titanium. It was concluded that for the hardness values obtained with the two indenters were equivalent. The two indenters are shown on figure 2.10. Also, the values of the reduced Y, Y_r, and Berkovich hardness, H, of Fe-30Mn6Si1Pd-20%NaCl through time are represented in figure 2.11.

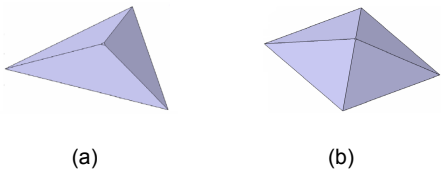

(a) (b)

Figure 2.10: Indenters geometry: (a) Berkovich; (b) Vickers [85].

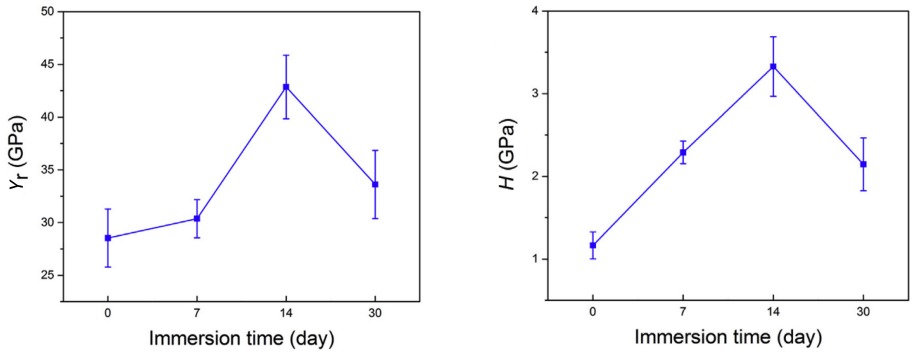

(a) (b)

Figure 2.11: Fe-30Mn6Si1Pd-20%NaCl mechanical properties in function of immersion in time: (a) reduced Young's modulus; (b) hardness [83].

Observing the evolution of Y_r and H through time, it can be stated that the increase in both of these properties should be due to the harder and stiffer nature of the products of the corrosion process that start filling the pores of the specimens. However, with long periods of time, the alloy and the corrosion products start losing their integrity, causing a decrease in Y_r and H. The final Y_r of the alloys were always recorded being closer to 20 GPa after the corrosion processes, being close to the value of human bones (3-7 GPa). With this, the stress shielding problems are excluded. Consequently, this feature causes good biomechanical compatibility.

On corrosion behaviour and mechanisms, the electrochemical data is presented in table 2.7, where are tabulated the values of average current density ($i_{average}$), corrosion resistance (R_p) and corrosion potential or equilibrium potential (E_{eq}). The values were taken out from the polarization curves, in the case of $i_{average}$ and E_{eq}, or measured experimentally, in the case of R_p. For further understanding, these concepts will be introduced in Section 2.3, where the literature review related to corrosion processes necessary for this dissertation is introduced.

Table 2.7: Electrochemical data calculated from the potentiodynamic polarization solution at 37 ° C, adapted from Feng et al. [83].

Wt.% NaCl	$i_{average}$ (A/cm^2)	R_p (Ω.cm^2)	E_{eq} (V vs. SCE)
Fe-30Mn6Si1Pd	1.865 x 10^{-6}	28380	-0.706
Fe-30Mn6Si1Pd-10NaCl	4.466 x 10^{-6}	21390	-0.737
Fe-30Mn6Si1Pd-20NaCl	2.918 x 10^{-5}	12570	-0.795
Fe-30Mn6Si1Pd-30NaCl	4.191 x 10^{-5}	11820	-0.846

Average current density can be used to evaluate the kinetics of a corrosion process because they are usually proportional. So, looking at table 2.7, the alloys are in order from the lowest to the highest corrosion rate, top to bottom.

For a global measurement of the potential cytotoxicity, cell viability and proliferation were both taken into account, where another type of cytocompatibility evaluation cells, the human osteosarcoma cell line Saos-2 cells, were used. The results are shown on figure 2.12.

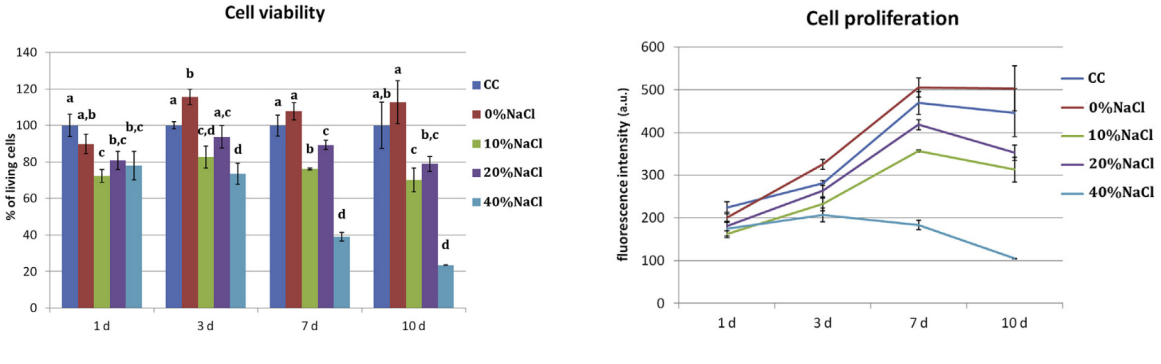

(a) (b)

Figure 2.12: Saos-2 cells during 10 days of culture with conditioned media: (a) Cell viability; (b) cell proliferation [83].

The conclusions obtained by Feng et al. [83] were that the bulk specimen Fe-30Mn6Si1Pd-0%NaCl is not cytotoxic neither in cell viability not in proliferation, the intermediate specimens Fe-30Mn6Si1Pd-10%NaCl and Fe-30Mn6Si1Pd-20%NaCl cannot be considered cytotoxic according to ISO 10993-5 [76], and Fe-30Mn6Si1Pd-40%NaCl is cytotoxic. The major conclusion in this parameter is that the higher corrosion and ion release from specimens possessing high porosity can compromise the biocompatibility of the specimens.

Sharma and Pandey [78] developed specimens to evaluate the influence of porosity on the corrosion behaviour of porous iron scaffolds, using a new process based on amalgamation of 3D printing and pressureless microwave sintering. Two different types of specimens were designed: random porous iron scaffolds (RPIS) using only the microwave sintering where the random porosity is attributed to the absence of pressure during the process, and topologically ordered porous iron scaffolds (TOPIS) using both microwave sintering and 3D printing. Porous Fe scaffolds with predesigned topologically ordered interconnected porous structure were developed, to evaluate the influence of inter-connected porosity. The computer-aided design (CAD) of these designed porous structure is presented on figure 2.13.

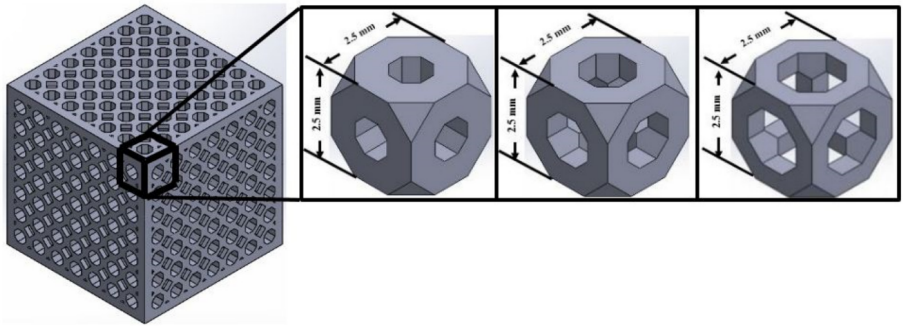

Figure 2.13: Designed CAD model of TOPIS samples. In detail, the three levels of porosity with the pore size of 1.0, 1.25 and 1.5 mm [78].

Additionally, later in 2019, the same authors published another article [86], continuing the previous work [78], designing new specimens of TOPIS type with new unit cell structures, and with all RPIS and TOPIS having higher levels of porosity. The new interconnected unit cell structures for TOPIS samples were three and are represented in figure 2.14, with a range of porosity from 45.63 to 86.90 %. The RPIS had a range of porosity of 12 until 53 %. The porosity level in the new RPIS and TOPIS was attributed to the scaffolds as in Sharma and Pandey [78].

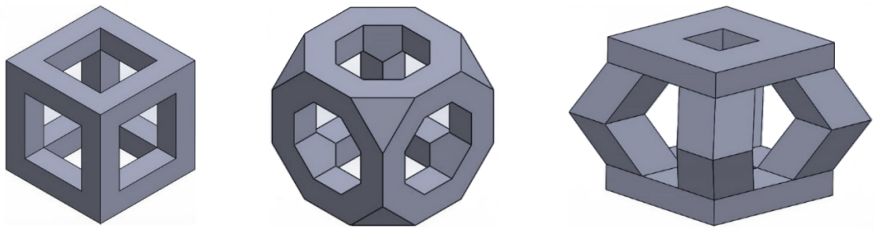

(a) (b) (c)

Figure 2.14: CAD model of unit cell structures used for preparation of TOPIS samples: (a) cubic; (b) truncated octahedron; (c) pyramid shaped [86].

Electrochemical tests were performed for every specimen in the RPIS group, immersing the samples in SBF at 37 ◦ C. The results of these tests are on table 2.8. In the table are E_{eq} measured in milivolts with saturated calomel electrode, SCE, as a reference electrode, the $i_{average}$ normalized with the surface area of the samples and measured in microampere per square centimeter, and lastly the corrosion rate, measured in thickness, in mm, corroded per year.

Table 2.8: Corrosion parameters for RPIS samples in prepared SBF solution at 37 ◦ C determined using Tafel analysis, adapted from Sharma and Pandey [86].

Porosity (%)	E_{eq} (mV vs. SCE)	$i_{average}$ (A/cm^2)	Corrosion rate (mmpy)
12.20	-595.2 ± 28.3	27.46 ± 3.10	0.275 ± 0.04
16.83	-608.9 ± 22.1	42.96 ± 3.34	0.501 ± 0.04
21.06	-638.9 ± 20.3	52.99 ± 1.44	0.615 ± 0.03
26.10	-684.1 ± 16.3	64.82 ± 0.91	0.753 ± 0.02
29.80	-693.6 ± 18.4	65.51 ± 1.20	0.760 ± 0.03
35.10	-725.3 ± 33.2	80.21 ± 2.23	0.932 ± 0.10
39.60	-737.6 ± 36.1	83.97 ± 0.61	0.980 ± 0.10
44.01	-761.1 ± 29.4	85.30 ± 4.11	0.991 ± 0.20
49.20	-704.1 ± 35.4	83.41 ± 1.82	0.969 ± 0.10
53.20	-731.1 ± 40.1	83.78 ± 2.42	0.962 ± 0.14

As for the RPIS, electrochemical tests were performed for the specimens in the TOPIS group, with the same experimental method. The results of these tests are on table 2.9.

Table 2.9: Corrosion parameters for TOPIS samples in prepared SBF solution at 37 ◦ C determined using Tafel analysis, adapted from Sharma and Pandey [86].

Porosity (%)	E_{eq} (mV vs. SCE)	$i_{average}$ (A/cm^2)	Corrosion rate (mmpy)
45.63	-759.6 ± 31.1	193.34 ± 3.22	1.640 ± 0.04
50.79	-706.5 ± 28.4	170.00 ± 4.13	1.474 ± 0.10
54.89	-747.1 ± 21.2	135.10 ± 2.20	1.191 ± 0.03
59.99	-690.7 ± 24.3	115.87 ± 2.51	1.031 ± 0.02
71.89	-691.2 ± 19.1	87.75 ± 1.40	0.795 ± 0.02
80.97	-668.6 ± 18.0	73.34 ± 2.01	0.710 ± 0.04
86.9	-684.7 ± 15.4	62.95 ± 1.52	0.625 ± 0.02

These results obtained in the most recent article by Sharma and Pandey [86] were similar to the results obtained in the older one Sharma and Pandey [78], with conclusions being added to the results for specimens with higher porosity levels. Looking at tables 2.8 and 2.9, some conclusions can be taken: 1) in RPIS, with the increase in the microporosity, the corrosion rate increases, due to the increase in the exposed surface of the specimens and the increased susceptibility to pitting corrosion; 2) higher levels of microporosity lead to a higher interconnectivity and greater size of the pores, so fewer sites for pitting corrosion would exist due to the free flow of the SBF solution; 3) the same reasoning of the last point is applicable to TOPIS, so an adequate arrangement of random microporosity and designed macroporosity is required for successful application of pure iron scaffolds in biodegradable implants.

These consequences cause the iron to have a greater loss of mass in the same period of time.

Investigations reported in Li et al. [79] verified that functionally graded porous structures, never produced until then, exhibit enhanced strength, ductility and energy absorption ability when compared with uniform porous structures. The denominations of the different types of specimens based on a 1.4 mm diamond unit cell includes a uniform structure with a 0.2 mm strut thickness (S0.2), a functionally graded porous structure with a strut thickness changing from 0.2 mm on the periphery to 0.4 mm in the center (Dense-in), a functionally graded porous structure with the strut thickness starting from 0.4 mm on the periphery and decreasing to 0.2 mm in the center (Dense-out), and a uniform porous structure with a strut thickness of 0.4 mm (S0.4). The samples were produced using selective laser melting (SLM), a powder bed-based technique of AM. The process is started layering a 3D drawing based on the defined layer thickness. Then, a roller pushes the powder to the substrate plate with the layer thickness previously defined, and the selected areas from the layering process are melted with a high-power laser, fusing the powder together. To avoid impurities in the part being produced, the chamber is filled with an inert gas like nitrogen or argon [87]. A schematic of the SLM process is shown on figure 2.15.

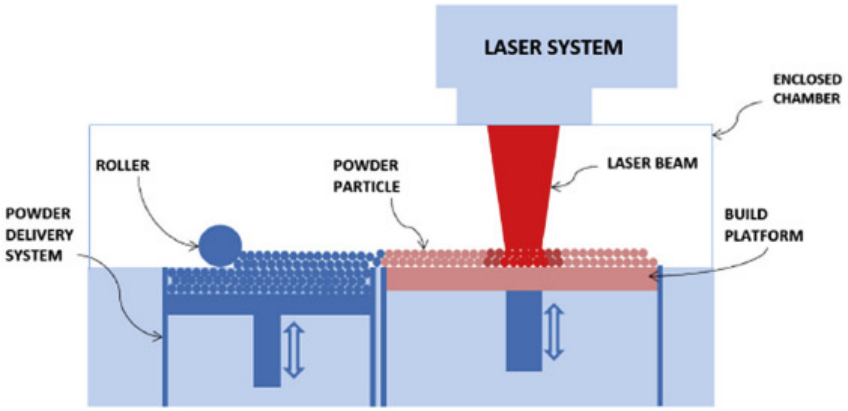

Figure 2.15: Schematic of the selective laser melting process [87].

These four types of samples, direct printed using SLM are represented in figure 2.16.

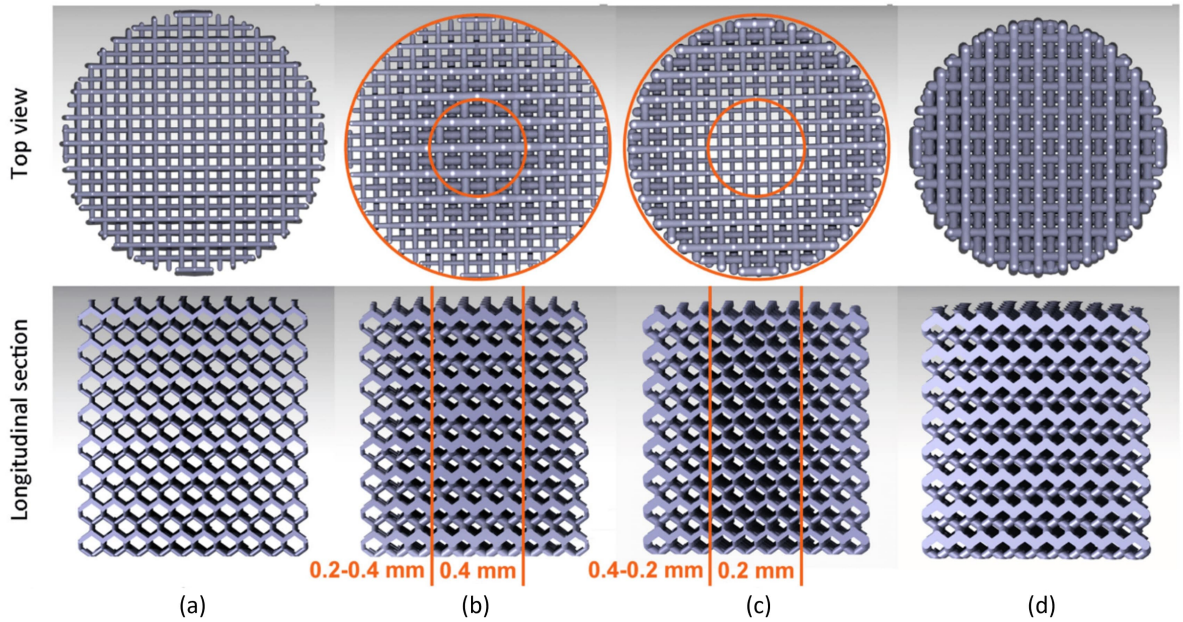

Figure 2.16: Longitudinal and top views of the CAD models of: (a) S0.2; (b) Dense-in; (c) Dense-out; (d) S0.4 [79].

The specimens designed by Li et al. [79] had the weight loss and the mechanical properties before degradation presented in table 2.10.

Table 2.10: Mechanical properties and weight loss of the SLM produced samples [79].

	Weight loss (%)	Compressive Yield Stress (MPa)	Youngs' Modulus (GPa)
S0.2	16.7 ± 3.3	10.7 ± 0.4	0.9 ± 0.1
Dense-in	8.9 ± 0.4	32.9 ± 1.6	1.8 ± 0.1
Dense-out	10.3 ± 0.3	30.5 ± 0.3	1.8 ± 0.0
S0.4	5.1 ± 0.9	53.1 ± 0.9	2.8 ± 0.1

Overall, an increase in the porosity caused a faster weight loss, and the mechanical properties after four weeks under immersion in simulated body fluids were adequate for implants. The stress-strain curves of uniaxial compression before and after the biodegradation tests are presented in figure 2.17.

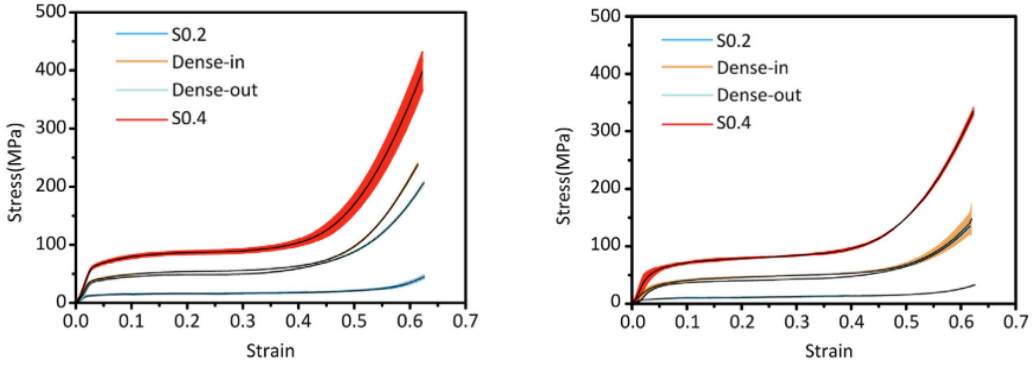

Figure 2.17: Mechanical properties of the AM porous iron specimens before and after biodegradation for 28 days: stress-strain curves (a) before biodegradation; (b) after biodegradation [79].

Also, the results shown that, in all of the AM porous iron specimens, the Y was 0.5-2.1 GPa and the yield stress was 8-48 MPa, being those similar values to the trabecular bone (see table 2.4).

Cytocompatibility tests in Li et al. [79] were performed using extracts from different types of iron scaffolds developed and put into comparison to a control of extracts from bio-inert Ti-6Al-4V. The results are presented in figure 2.18.

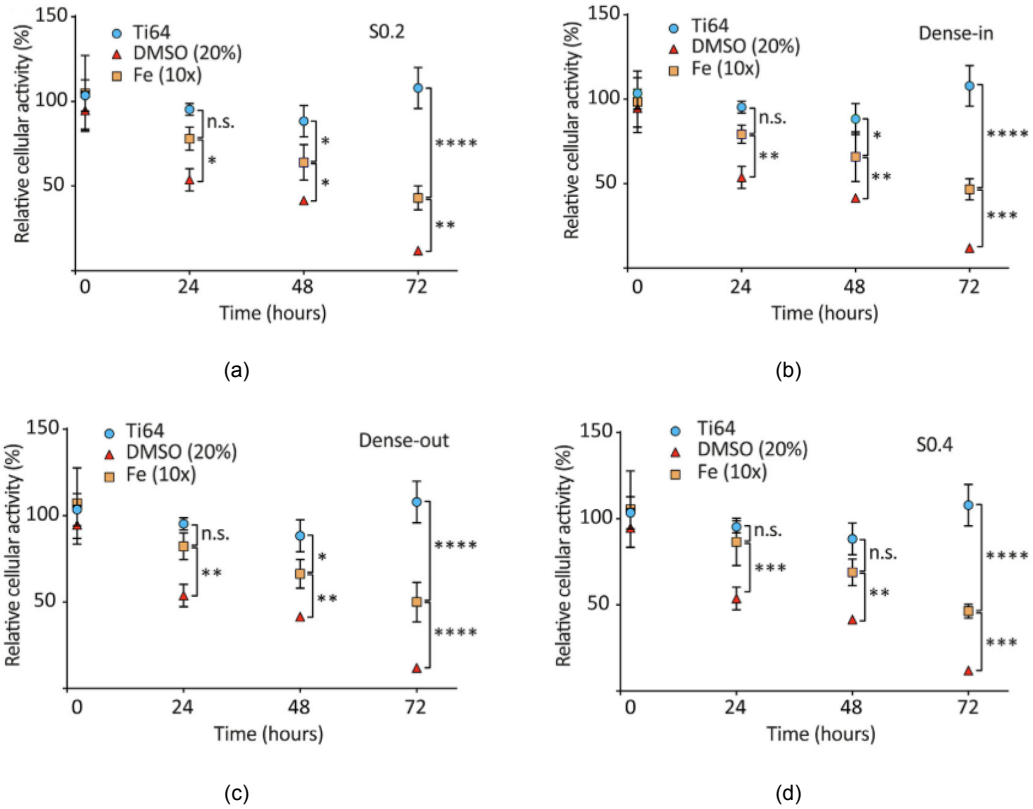

Figure 2.18: Relative cytocompatibility, in percentage, of different iron scaffolds against titanium controls: (a) S0.2; (b) Dense-in; (c) Dense-out; (d) S0.4 [79].

The results from figure 2.18 were put into the table 2.11.

Table 2.11: Relative cytocompatibility (%) of different iron scaffolds against titanium controls, after 24, 48 and 72 hours [79].

	Relative cellular activity (%) after		
	24h	48h	72h
S0.2	77.8	63.8	42.6
Dense-in	79.2	65.8	46.5
Dense-out	82.2	66.4	50.0
S0.4	86.5	68.8	46.1

Figure 2.18 and table 2.11 shown that a 24 hours test lead to a cytocompatibility higher than 75% (non-cytotoxic) for all the specimens. After 48 hours, only S0.4 remained at almost 70% (limit of cytotoxicity) and it did not significantly differ from the Ti-6Al-4V controls; however, all specimens extracts revealed cellular activity higher than 63%, considered slightly cytotoxic. Lastly, after the 72 hours extraction, three of the four specimens were considered moderately cytotoxic, with a cellular activity lower than 49%. Moreover, with *in vitro* condition the released ions can accumulate and result in high concentrations, and when *in vivo* are quickly diluted, reducing the chances of happening cytotoxicity. Lastly, it was found that graded porous scaffolds produced with AM processes resulted in high cell seeding efficiency and in an acceleration of the bone deformity regeneration.

Salama et al. [1] confirmed that increasing the porosity amount causes lower mechanical strength, and that the topological design also had influence on specimens' mechanical properties and on the biodegradation behaviour.

Three different porous samples that were designed and manufactured in iron in Salama et al. [1] are shown in figure 2.19. Bulk specimens were also submitted to a corrosion analysis. The external dimensions and porosity of all the specimens are presented in table 2.12. The designation of the specimens means that they have bidisperse holes with different dimensions (2 and 4 mm diameter holes) and the percentage in the end of the name indicates the porosity of the specimen.

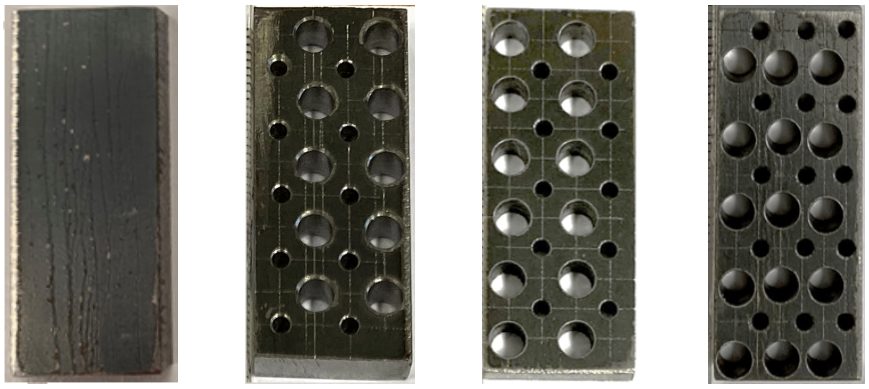

(a) (b) (c) (d)

Figure 2.19: Iron specimens: (a) Bulk; (b) A4_2_20%; (c) A4_2_23%; (d) A4_2_30% [1].

Table 2.12: Specimen dimensions.

Designation	External Dimensions (mm)	Porosity (%)
Bulk	23.55 x 9.65 x 5	-
Bidisperse A4_2_20%	44 x 18 x 5	20
Bidisperse A4_2_23%	44 x 18 x 5	23
Bidisperse A4_2_30%	44 x 18 x 5	30

For the *in vitro* immersion tests, SBF solution was prepared according to Kokubo and Takadama [88], and the immersion tests were performed at 37 ° C ± 1 ° C to evaluate the degradation behaviour, principally the weight loss. The porous samples were separately immersed in 50 mL of SBF solution and had two different experimental methods: 1) the solution was replaced every 7 days until 28 days, and on the method 2) the Fe specimen experiences a continuous corrosion until six weeks (42 days). The bulk specimens only were submitted to a 28 days experiment, with mass analysis and SBF replacement every 7 days. The experimental process is schematized in figure 2.20.

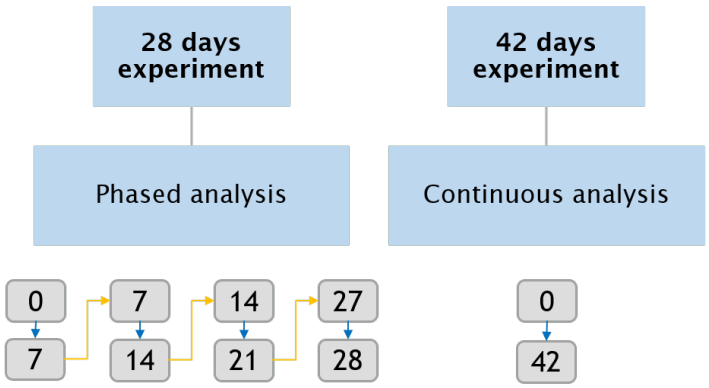

Figure 2.20: Procedure of the experimental corrosion tests in Salama et al. [1].

After the corrosion test, the Fe samples were rinsed with deionized water, and dried. Then, the weight loss was evaluated, and it is presented in figure 2.21. It was concluded that the weight loss increased with immersion time. For the period of 42 days, the weight loss was different for samples with different porosity, but no significant difference was observed.

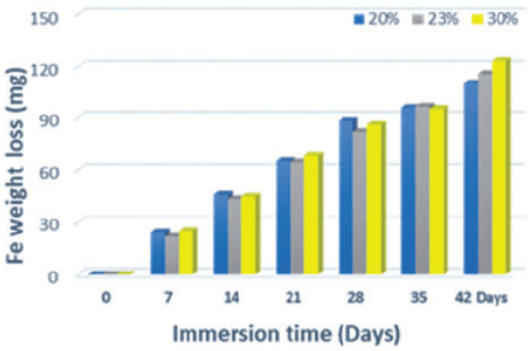

Figure 2.21: Porous iron weight loss as a function of SBF immersion time, in Salama et al. [1].

The specimen's stiffness was tested through a three-point bending (3PB). The experimental results of the stiffness values for the bidisperse specimens before and after the immersion tests are shown on table 2.13.

Table 2.13: Experimental results for 3PB tests of samples before and after immersion in SBF solution: stiffness *K*, adapted from Salama et al. [1].

Arrangement	K (N/mm)		
	Initial	28 days	42 days
Bulk	12.3×10^3	-	-
A4_2_20%	11.1×10^3	11.2×10^3	9.9×10^3
A4_2_23%	9.0×10^3	9.4×10^3	8.2×10^3
A4_2_30%	8.8×10^3	5.2×10^3	5.4×10^3

It was concluded that lower porosity samples show a decrease of stiffness with the increase of the immersion period, and that higher porosity samples exhibit a decrease in stiffness equal for 28 and 42 days, that is, independent of the immersion period. Summing up, the amount of porosity affects the degradation behaviour of samples evaluated by 3PB tests.

2.3 Corrosion

Since this dissertation involves mechanical characterization of iron combined with FEA to predict the corrosion behaviour of Fe in contact with SBF, some concepts and variables of corrosion processes need to be introduced. In figure 2.22 it is presented the uniform corrosion process of iron, in the specific case of this dissertation, when in contact with SBF.

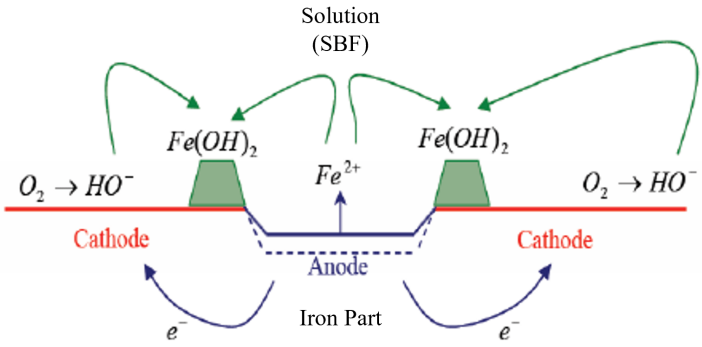

Figure 2.22: Uniform corrosion process of iron, adapted from [89].

The SBF serves the purpose of simulating blood and, in this case, simulating the corrosion caused by it. SBF is one in a large amount of physiological solutions already created, for example, Ringer's solution, Hanks' Balanced Salt Solution, 199-medium, revised-SBF and modified-SBF. The SBF and its derivative evolutions are the ones that presented better results [90].

The following sections serve to elaborate and explain some topics of this branch of physics and chemistry, specifically about what physical properties influence the corrosion rate in this corrosion process.

2.3.1 Electrical conductivity

The electrical conductivity, κ, is one of the important parameters in corrosion, and it is the reciprocal process of electrical resistivity. It measures the ability of a certain material to conduct electrical currents. Higher levels of conductivity make an environment more corrosive [91]. According to Magyari et al. [92], κ of SBF varies through time as shown on figure 2.23. The values of x in the figure are related to the samples used to measure the SBF electrical conductivity used by Magyari et al. [92], with the chemical composition (80-x)SiO_2.20Al_2O_3.xFe_2O_3. The value of x can be 5, 10 or 15, being referred to the value of the samples mol%.

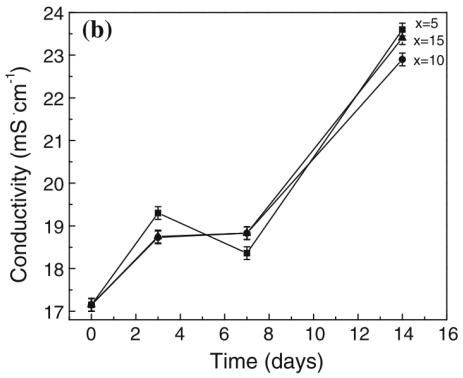

Figure 2.23: Electrolyte conductivity values in Magyari et al. [92].

2.3.2 External Electric Potential

The external electric potential is the voltage that is constantly applied on the specimen boundaries that are in contact with the electrolyte. Also, the concept of open circuit potential (OCP) needs to be introduced, that is the potential between the working electrode (in this case, Fe) and the environment (the SBF), with respect to a reference electrode [93], when there is no external load applied. According to the graphic presented in Wagener et al. [94], shown on figure 2.24, the OCP obtained with a reference electrode of silver chloride (Ag/AgCl) with pure iron on SBF is -0.68 V. The Ag/AgCl reference electrode differs from the SCE reference electrode used in other works [71, 78]. This results in a OCP for SCE that had the value -0.636 V.

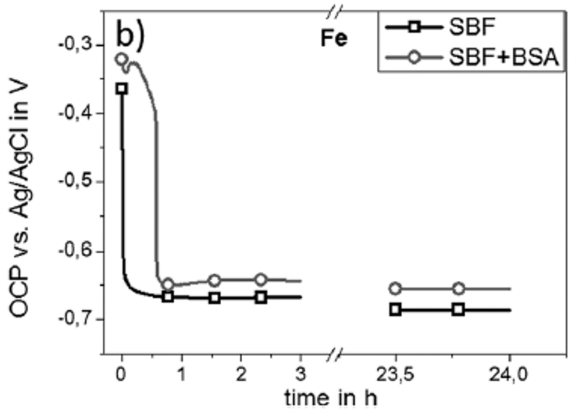

Figure 2.24: OCP vs. time graphic in Wagener et al. [94].

2.3.3 Polarization curves

According to Fontana [95], polarization curves, or Tafel curves, are plots of the current, i, needed to maintain the metal (working electrode) at the applied potential, E, for a specific electrode-electrolyte combination, or the voltage (V) output for a given current density (current per superficial area, A/m^2).

To obtain this polarization curves, it is necessary to perform an electrochemical analysis. According to Fontana [95], the schematic diagram presented in 2.25 represents a simplification of an electric circuit that could be used to obtain a polarization curve. However, further explanation of a fully working electric circuit that could generate an accurate polarization curve is available in Legault and Walker [96].

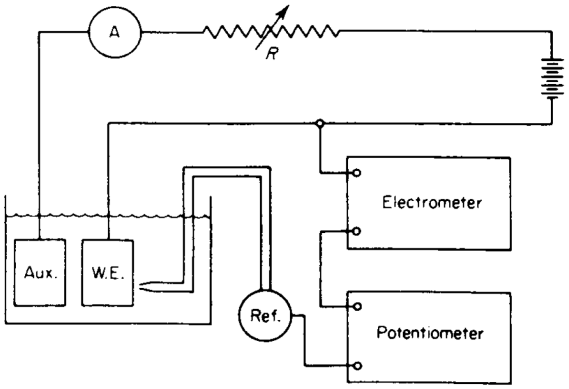

Figure 2.25: Electric circuit to perform an electrochemical analysis [95].

The procedure to obtain the polarization curve with the equipment shown on 2.25 is described as follows. The metal sample is defined as working electrode W.E., and the current is supplied by means of an auxiliary electrode Aux., being this of some inert material, like platinum. The current is measured with an ammeter A, and the potential of the working electrode is measured in relation to the reference electrode, using a potentiometer-electrometer circuit. Reducing the value of the variable resistance R, the current is increased. Then, the potential and current at different settings are simultaneously measured, obtaining the polarization curve [95].

This type of plot gives two very important properties, that are the $i_{average}$ and the E_{eq}.

The SBF made with the processes from Kokubo and Takadama [88] had already been put in contact with iron in Sharma and Pandey [78], where an electrochemical analysis was performed and a polarization curve between the electrolyte SBF and the electrode pure Fe was created. In the present work, polarization curves by two different authors were used, one achieved by Sharma and Pandey [78] and the another obtained by Čapek et al. [71]. However, this second polarization curve was obtained with a SBF created with a different process from the one used by Salama et al. [1] and Sharma and Pandey [78]. The two polarization curves are shown on figure 2.26.

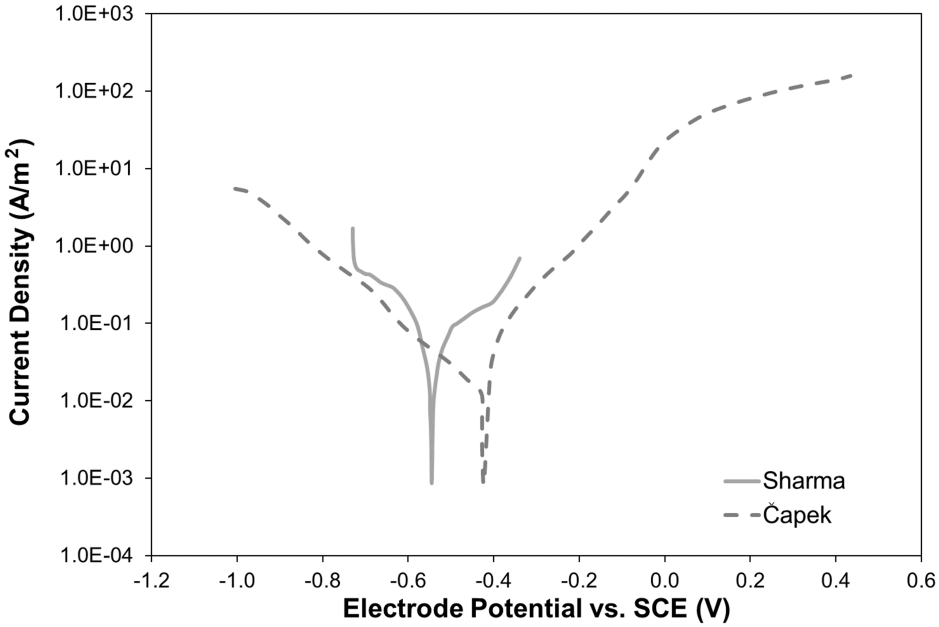

Figure 2.26: Sharma and Pandey [78] and Čapek et al. [71] polarization curves.

In order to get the two variables presented, $i_{average}$ and E_{eq}, a Tafel extrapolation, or Tafel analysis, is performed on the polarization curves. Usually, these values are computed with specialised softwares when an electrochemical analysis is performed. The value of E_{eq} is easily obtained, as it is corresponds to the electrode potential that causes the lowest current density. The value of $i_{average}$ is a little more difficult to obtain, but according to Fontana [95] there are some simple rules to take $i_{average}$ value from a polarization curve:

1. The anodic part of the curve (more negative) is more relevant than the cathodic part;
2. Mark a constant line corresponding to E_{eq};
3. Search for a linear segment (around 15 to 30 mV) in the Tafel curve;
4. Try to find linear segments as close to the E_{eq} as possible;
5. The intersection of the prolongation of the linear segments with E_{eq} line will dictate the value of $i_{average}$.

The representation of the Tafel extrapolation procedure according to Fontana [95] is presented in figure 2.27.

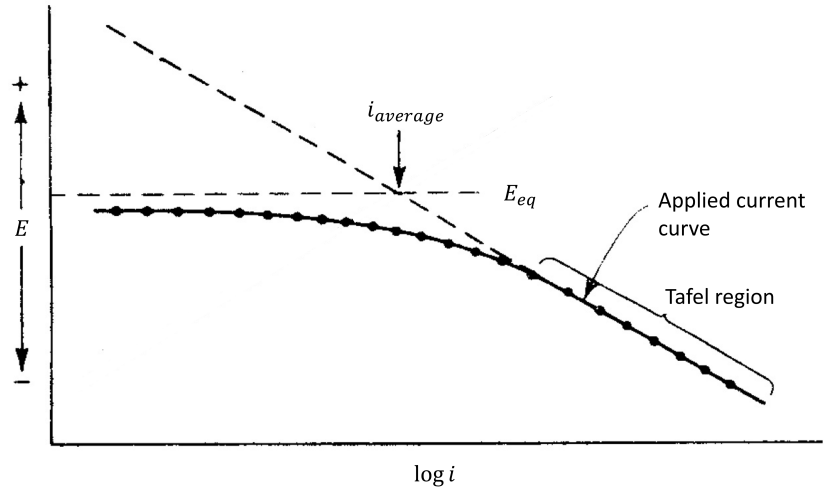

Figure 2.27: Representation of the Tafel extrapolation, adapted from [95].

The values of E_{eq} and $i_{average}$ in Sharma and Pandey [78] and Čapek et al. [71] are presented in table 2.14.

Table 2.14: E_{eq} and $i_{average}$ from electrochemical analysis [71, 78].

Polarization Curve	Equilibrium Potential (V)	Average Current Density (A/m^2)
Sharma 2019	-0.545	0.1153
Capek 2017	-0.422	-

Chapter 3

Materials and Methods

According to the literature review, the fact that iron is one of the most promising materials to be used on bone implants and to the work developed previously by Salama et al. [1], the material that is going to be used on this dissertation is Fe.

The aim of this dissertation is to evaluate the iron corrosion behaviour through FEA, validating the models created with previous experiments by Salama et al. [1]. For this, tensile and compression tests were performed to obtain mechanical properties of the material, to be inserted in the FEM software for the corrosion analysis, as the mechanical behaviour of Fe could influence the implant performance, for example, with stress assisted corrosion.

In this chapter, the experimental and numerical procedures will be described. The mechanical properties of the iron were obtained through tensile and compression tests input the numerical simulations of the corrosion behaviour with the *COMSOL* software, and the numerical model was calibrated with the experimental results from Salama et al. [1].

3.1 Material characterization

Iron rods with a diameter of 19 mm and a length of 1000 mm, commercially available with 99.8% purity were purchased from *Goodfellow Inc.*, Cambridge, UK.

3.1.1 Tensile Tests

The tensile specimens were designed with software 3D CAD Solidworks® according to ASTM E8/E8M - 21 [97], Standard Test Methods for Tension Testing of Metallic Materials, where the round specimen type 2 with gauge length four times the diameter (E8) was used. The machining of these specimens was performed in a CNC lathe by NOF, in IST. The tensile specimen geometry and technical drawing are represented in figure 3.1. After the machining, the specimens were stored in oil to prevent oxidation until the testing day. Before testing, the specimens were cleaned with acetone to degrease the surface.

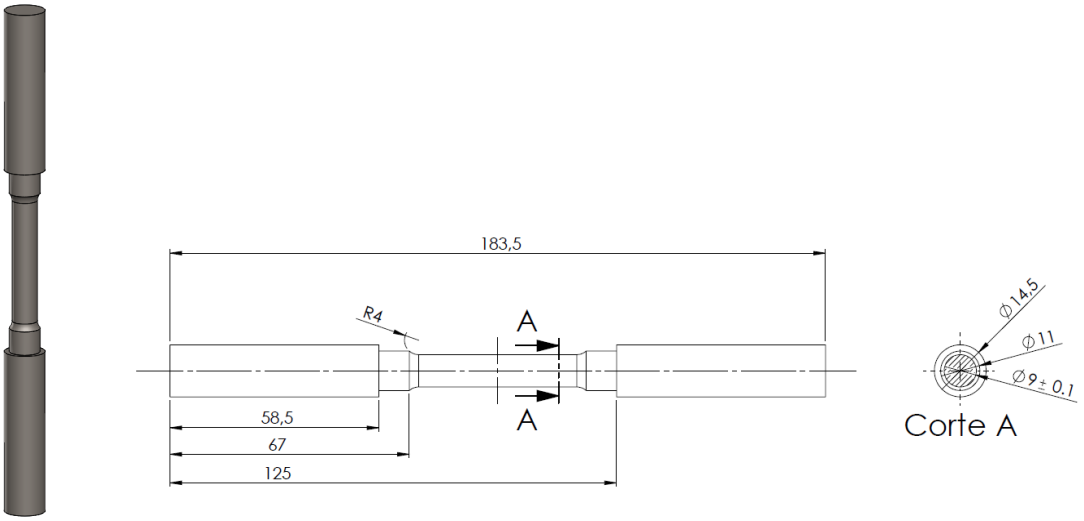

Figure 3.1: Tensile specimen (a) Render; (b) Technical drawing.

The tensile tests were conducted at room temperature on a universal testing machine, Instron 5900R, with a load cell of 200 kN. The test parameters are in accordance with the ASTM E8 / E8M-21 [97] standard, using the *Bluehill Software* for recording the test data. Figure 3.2 shows the tensile test machine used for the tests.

Figure 3.2: Tensile test machine.

In total, five specimens were tested until fracture occurred. Load-displacement curves were obtained for each test, being the load measured by the machine load cell, and the displacement was taken from the equipment of Digital Image Correlation (DIC), that will be further explained on Section 3.1.3. The

displacement used was the one recorded from the DIC equipement and not from the INSTRON machine, because in the latter one the displacement is measured by the crosshead displacement, inducing in error, since the focus area is in the middle of the specimen.

Having the force-displacement values and the initial gauge length and cross section area of the specimen it is possible to compute firstly the engineering strain and engineering stress, e and S, and then the true strain and true stress, ε and σ. These mechanical properties are obtained with the equations:

$$\mathrm{e} = \frac{\text{Displacement}}{\text{Initial Length}} \tag{3.1}$$

$$\mathrm{S} = \frac{\text{Force}}{\text{Initial Cross-Sectional Area}} \tag{3.2}$$

$$\varepsilon = ln(\mathrm{e} + 1) \tag{3.3}$$

$$\sigma = \mathrm{S}(\mathrm{e} + 1) \tag{3.4}$$

3.1.2 Compression Tests

Compression specimens were designed with the software 3D CAD Solidworks® following the designs performed in Magrinho et al. [98], that are according to ASTM E9-19 [99], Standard Test Methods of Compression Testing of Metallic Materials at Room Temperature: C1 specimens alike were reproduced, where the diameter was of 18 mm instead of 20 mm, due to the dimensions of the iron rods purchased. These specimens and the technical drawing are presented in figure 3.3. The machining of this specimen was performed in a conventional lathe in *Laboratório de Tecnologia Mecânica*. As described in Section 3.1.1, the specimens were stored in oil to prevent oxidation until the testing day and, before testing, were cleaned with acetone to degrease the surface.

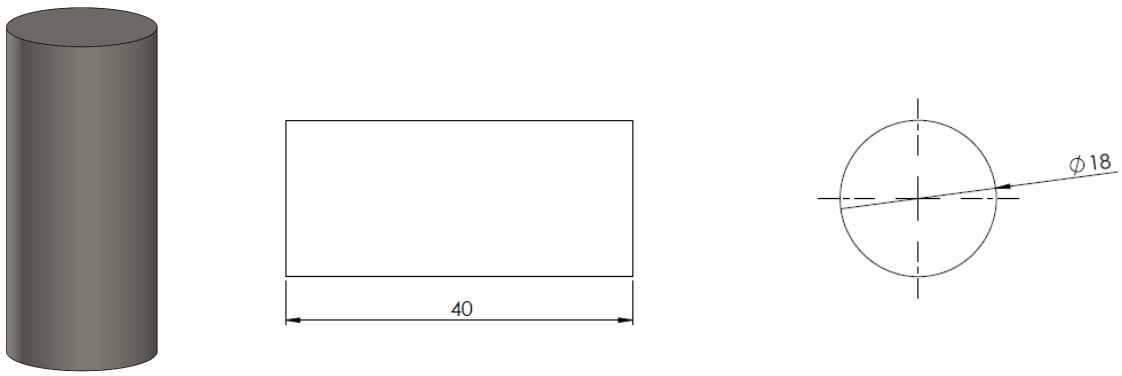

Figure 3.3: Compression specimen (a) Render; (b) Technical drawing.

The compression tests were performed at room temperature on a hydraulic testing machine, the

Instron SATEC 1200, with a load cell of 1200 kN, shown on figure 3.4. The test is performed at constant speed according to ASTM E9-19 [99], using *Bluehill Software* for data interpretation and recording. Teflon® (polytetrafluoroethylene) sheets with thickness of 0.25 mm were used on top of the specimens with lubrication purposes and to guarantee very low friction [98].

Figure 3.4: Hydraulic testing machine *Instron SATEC 1200* [100].

As the structure of the compression machine is very tall, the shaft causing compression is long and can be a little compressed while it should be rigid, suffering elastic deformation, altering the displacement results. So, a dry-run testing, with no specimen between the plates of the setup was performed, in order to analyse that behaviour. After this procedure, it was possible to correct the displacement values in the mechanical curves.

Three specimens were tested in total. The displacement was, at least, 50% of the initial height of the sample. or according to the technical drawing shown on 3.3, 20 mm.

Load-displacement curves were obtained for each test, where both groups of values were taken from the *Bluehill software*.

As described in Section 3.1.1, the values for e, S, ε and σ are computed with the equations 3.1 to 3.4, in order to then plot the stress-strain curves. Lastly, the DIC equipment was used to obtain strain measurements.

3.1.3 Strain Measurement

The strain and displacement measurements of the tensile and compression tests performed on the universal testing machines *Instron 5900R* and *Instron Satec 1200* were obtained with a DIC system: model *Q-400 3D* from *Dantec Dynamics*. This equipment has two cameras with 6 megapixels of

resolution and 50.2 mm of focal length with an aperture of f/8. The surface of the specimens was painted firstly with white spray, and then sprayed with stochastic black droplets, presenting a dotted pattern. A representation of the DIC system and of the preparing process is shown on figure 3.5.

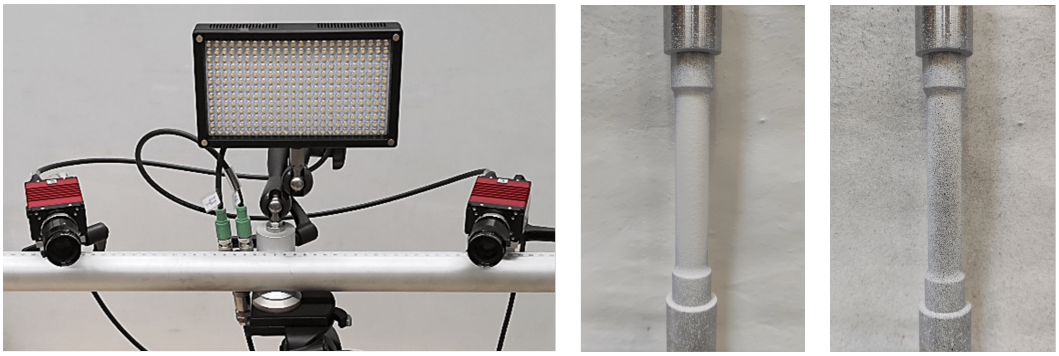

(a) (b) (c)

Figure 3.5: Strain measurement equipment and preparing (a) *Q-400 3D* model from *Dantec Dynamics* [100]; (b) first layer of white spray on tensile specimen; (c) final aspect of painted tensile specimen.

The painted, measuring area, was illuminated with one to three spotlights in order to provide a larger measuring section of the specimens. There is one spotlight in the middle of the cameras that is always part of the setup, and the other two are additional, only used if more light is necessary for the proper functioning of the system. The image acquisition was made with a frequency of 10 frames per second, and the correlation algorithm was performed with the *ISTRA 4D* software. The setup for the tensile and compression tests are shown on figures 3.6 and 3.7, respectively.

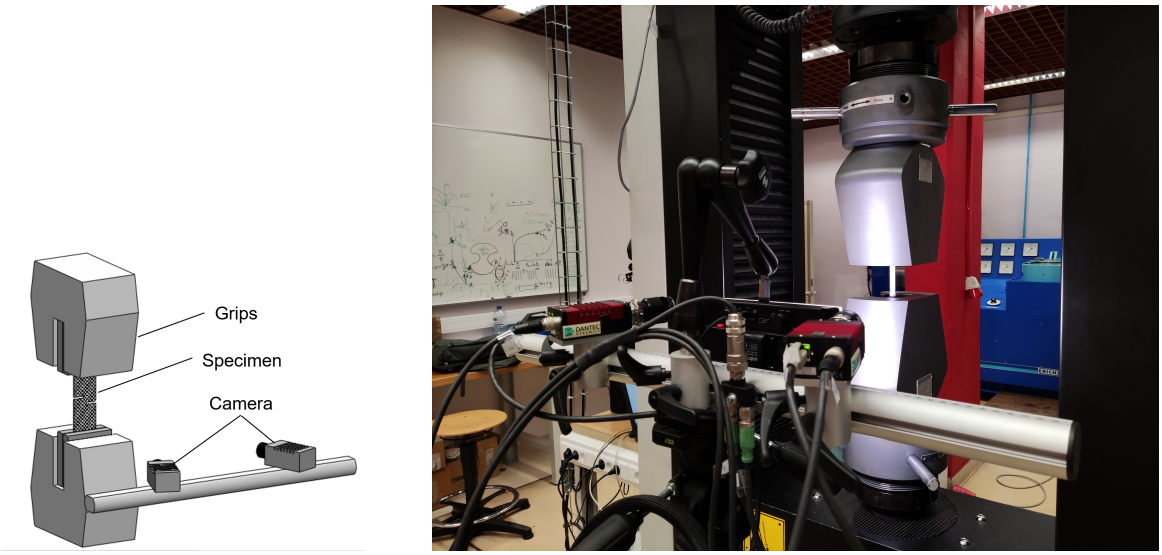

(a) (b)

Figure 3.6: Tensile test DIC system setup (a) schematic representation [100]; (b) system setup in the experimental tests.

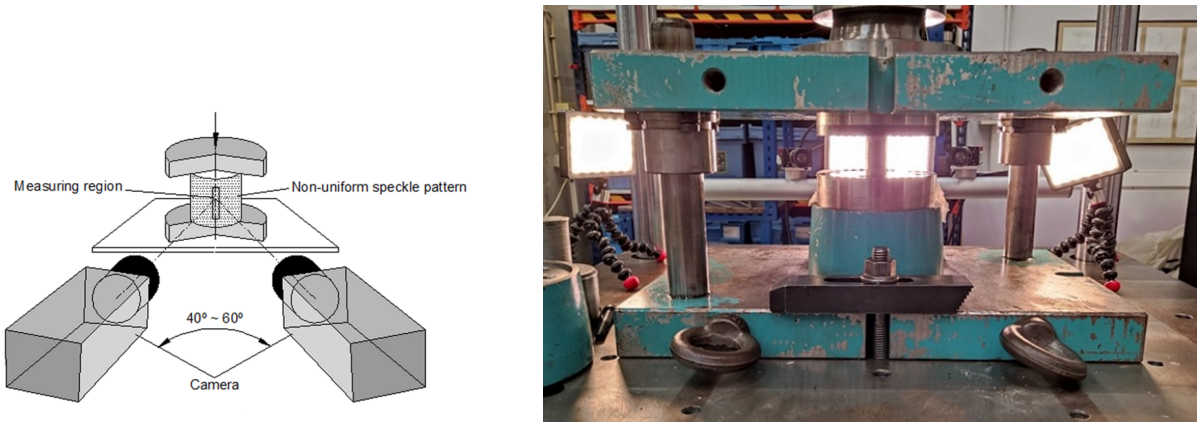

(a) (b)

Figure 3.7: Compression test DIC system setup (a) schematic representation [98]; (b) system setup in the experimental tests.

3.2 Finite Element Modelling of iron degradation

As already mentioned in Chapter 1, this work relies on previous results obtained by Salama et al. [1], where the purpose of the study was to evaluate the degradation behaviour and the mechanical properties of porous iron samples with porosities from 20 to 30%.

For the numerical simulations of the corrosion behaviour the FEM software *COMSOL Multiphysics* version 5.6 and one of its available modules, the *Corrosion Module*, was used. This *COMSOL* module mainly uses implicit solutions, and it offers the possibility to use elements from first up to fifth order and different nonlinear methods to compute the solution. In this case, first order elements and an Automatic Newtonian Nonlinear method, where the solver automatically determines a damping factor in each iteration of Newton's method, were used [101, 102].

The Corrosion Module has many physics features available, such as chemical species transport, electrochemistry and corrosion interfaces. All of them describe the potential and current distribution in the electrolyte and in the corroding or protected metallic structure, allowing to include the influence of mass transport and heat transfer. Lastly, the ability to account for mass transport in the electrolyte allows for modeling the corrosion caused by variations in, for example, salt concentration, oxygen concentration, and pH [102]. Despite offering all these functionalities, only the basic physics features were used in this dissertation, in order to have a solid model as baseline.

In the Secondary Current Distribution interface model the rate of the electrochemical reactions can be described relating the reaction rate to the activation (or reduction) overpotential, η , defined in an electrode reaction as:

$$\eta = \phi_s - \phi_l - E_{eq} \tag{3.5}$$

where ϕ_s is the electric potential in the electrode , ϕ_l the electrolyte electric potential and E_{eq} is the already introduced equilibrium potential [102].

This physics interface, with the electrochemical corrosion being described by the reaction of iron

dissolution reaction $Fe - 2e^- \rightarrow Fe^{2+}$, uses several relations for the charge transfer current density and the overpotential, such as Butler-Volmer and Tafel expressions. The general expression is of Butler-Volmer type:

$$i_{loc} = i_0\left(\exp\left(\frac{\alpha_a F\eta}{RT}\right) - \exp\left(\frac{-\alpha_c F\eta}{RT}\right)\right) \tag{3.6}$$

where i_{loc} denotes the local charge transfer current density, i_0 the exchange current density, α_a the anodic transfer coefficient, α_c the cathodic charge transfer coefficient, F is the Faraday's constant, R the universal gas constant, and T the temperature [102].

Assuming high anodic overpotencials for a given current, as it is the case for iron in SBF, where the kinetics are slow, the cathodic therm for the original Butler-Volmer expression can be neglected. So, the anodic Tafel equation is as follows:

$$i_{loc} = i_0 \cdot 10^{\eta/A_a} \tag{3.7}$$

where A_a, in V, is the Tafel slope [102].

Lastly, for the Corrosion with Deformed Geometry, the deposition rate and electrode growth velocity are defined by the Current DIstribution interface between the electrolyte and the electrode. In the electrode surface it is specified which species participate in the electrode reactions, the reaction kinetics and the stoichiometry. The surface concentration variables of the deposited species are used to calculate the thickness of the deposited layer, and the depositing rate sets the boundary velocity for the deforming geometry. The dissolution (or deposition) is always assumed to occur in the normal direction to the electrode boundaries, with the velocity directed to the electrolyte domain: $\frac{\partial x}{\partial t} \cdot n = v_{dep,tot}$, where $v_{dep,tot}$ is the total growth velocity, the sum of the velocity contributions for all species and electrode reactions, according to:

$$v_{dep,tot} = \sum_i \frac{M_i}{\rho_i} \sum_m \frac{v_{i,m} i_{loc,m}}{n_m F} \tag{3.8}$$

where M_i is the molar mass in kg/mol, ρ_i is the density of the species in kg/m^3, $v_{i,m}$ is the stoichiometric coefficient of species i with respect to reaction m, and n_m is the number of electrons transferred [102].

Firstly, the Bulk iron specimen was used for validation of the numerical model comparing the numerical results with the experimental ones from Salama et al. [1], and a sensitivity analysis of parameters was performed. Only then the porous specimens from that article were analysed, in order to verify if the conclusions were general or not.

Lastly, a *COMSOL* tutorial was developed, explaining how a model like the one used in this work is created and how the results are evaluated. Some slides of this tutorial are presented in Appendix A.

3.2.1 Numerical model

3.2.1.1 Physics and Study

COMSOL Multiphysics has a *Model Wizard* that helps building the model, choosing the space dimension, physics interfaces, and the type of analysis. Several parameters must be selected in the model. For the numerical model it was considered:

- Space dimension: 3D dimension.
- Physics: ”Corrosion with Deformed Geometry and Secondary Current Distribution”. It computes the deformation of a part into a corrosive medium and describes a corrosion cell, assuming that the variations in the composition of the electrolyte are negligible.
- Study: ”Time Dependent with Initialization”. It is ruled by secondary current distribution equations, and consists of two steps:
  1. Current Distribution Initialization study: solves for the potential fields only;
  2. Time Dependent study: field computed by the first step is used as initial condition.

3.2.1.2 Specimen

COMSOL allows geometry drawing inside the software, but it is relatively limited, thereby only very simple steps were performed there - such as creating the cylinder for the total volume, some rotations and translations.

Firstly, the specimen (bulk or porous) was imported to *COMSOL* in .STL format. These specimens were designed in Solidworks® according to the specimens in Salama et al. [1], and they are shown in figure 3.8.

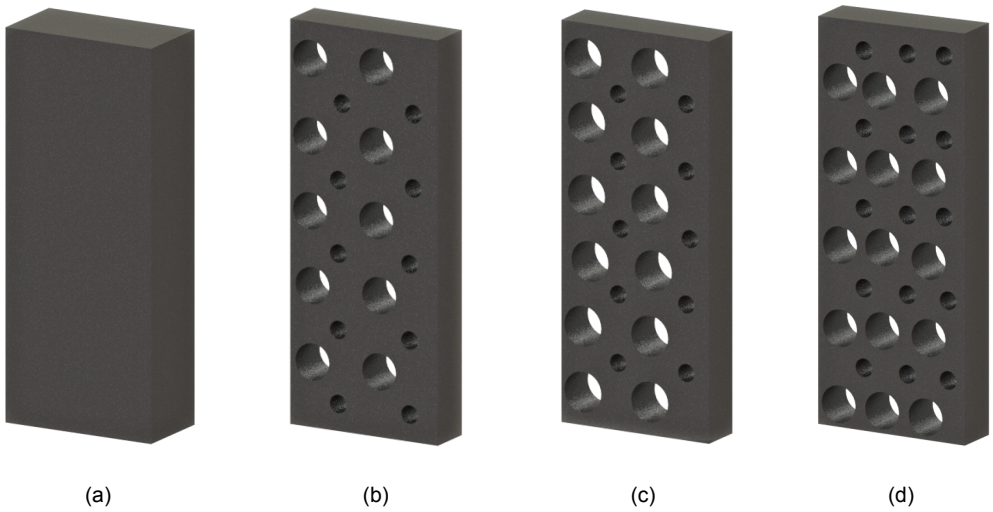

Figure 3.8: Specimens drawn on Solidworks® (a) bulk specimen; (b) A4_2_20% specimen; (c) A4_2_23% specimen; (d) A4_2_30% specimen.

Then, if it was desired that they should be inclined, a rotation was applied. After this, a cylinder around the specimen must be created to represent the electrolyte and specimen volume. Finally, a difference between the cylinder and the specimen must be performed, so the geometry left is the volume of the electrolyte, which is the domain that will be analysed, represented in figure 3.9. The recipient had a diameter of 35 mm and a height of also 35 mm.

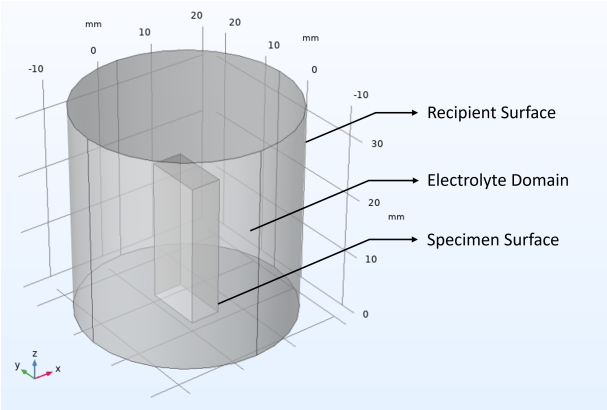

Figure 3.9: *COMSOL* model - vertical bulk specimen.

3.2.1.3 Material Properties

Now that the geometry is created, the model is ready to receive the materials inputs. In the corrosion analysis, they are attributed to the surfaces of the part that are in contact with the electrolyte - where the chemical reactions occur. For this type of analysis, the properties inserted in the model are the local current density expression, the equilibrium potential and the mechanical properties of the specimen.

The rules given by Fontana [95] described in Section 2.3.3 were used to take $i_{average}$ value from Čapek polarization curve. As it was not explicit how the values of $i_{average}$ were determined, the methodology presented in Fontana [95] in the Section 2.3.3 was applied to validate the values obtained by Sharma and Pandey [78], and also to identify new values to be used for the sensitivity analysis. The figure 3.10 represents the Tafel Extrapolation used on the Sharma polarization curve, for better understanding of how the rules are applied. The numbers in the figure are related to the enumeration of the rules in Section 2.3.3.

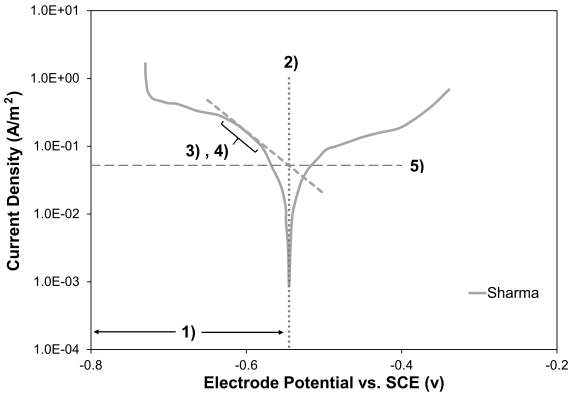

Figure 3.10: Rules by Fontana [95] applied on the Sharma polarization curve.

The Tafel analysis applied on the two polarization curves are shown of figure 3.11.

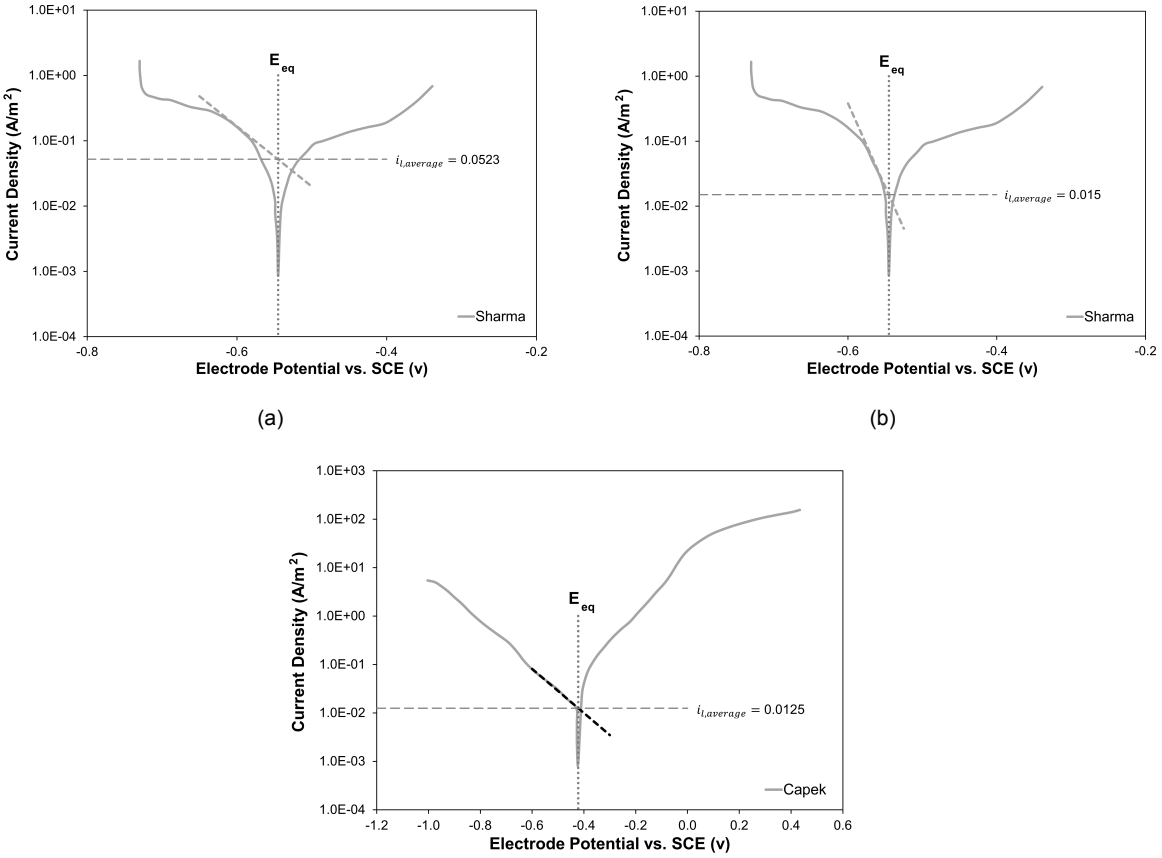

Figure 3.11: New values obtained with Tafel Extrapolation for Average Current Condition (a) Sharma additional $i_{average}$ 1; (b) Sharma additional $i_{average}$ 2; (c) Čapek $i_{average}$.

The data obtained with the Tafel extrapolation is summarized in table 3.1.

Table 3.1: Polarization curves data [71, 78].

Polarization Curve	Equilibrium Potential (V)	Average Current Density (A/m^2)
Sharma et al. (2019)	-0.545	0.1153 | 0.0523 | 0.015
Čapek et al. (2017)	-0.422	0.0125

3.2.1.4 Current Distribution and Boundary Conditions

When it comes to Current Distribution and Boundary Conditions, there is a need to define the current distribution condition. There were three types of current distribution available: Primary, Secondary or Tertiary. According to the *COMSOL* Multiphysics Reference Manual [101] and following the flow chart found on *COMSOL* Corrosion Module User's Guide [103] presented in figure 3.12, the Secondary Current Distribution was the most suitable for the primary simulations performed on this dissertation. In this same branch, it is also defined the reference electrode used in material previously established (on the polarization curves and on the equilibrium potential), that is used as a global electric reference potential.

Both in Sharma and Pandey [78] and Čapek et al. [71] the reference electrode was the SCE.

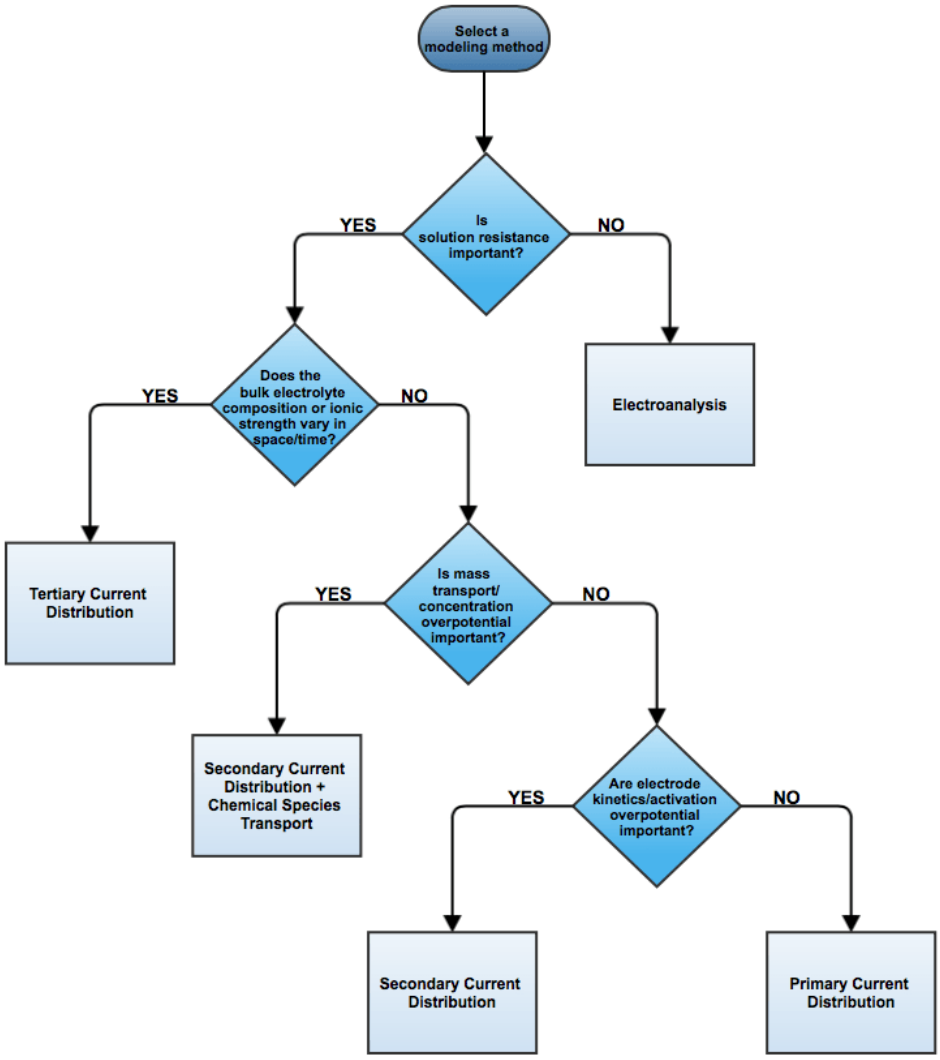

Figure 3.12: *COMSOL* - modelling method choice flow chart in *COMSOL* Corrosion Module User's Guide [103].

3.2.1.5 Other parameters

Other parameters that need to be set are the temperature, T, and the Electrolyte Conductivity, κ. T value was initially used as 310.15 K, or 37 $^{\circ}$ C, as this is the approximate body temperature and at which the experimental tests were performed [1]. As to κ value, experimental tests reported in Magyari et al. [92] studied the conductivity of Fe in SBF through time. A sensitivity analysis of this parameter was undertaken and the iterated values will be presented on Section 3.2.2.

Lastly, as for the boundary conditions, two options were applied: *External Electric Potential* (EEP) boundary condition, imposing constant voltage on the part external boundaries and setting the potential directly; *Average Current Density* (ACD) boundary condition, imposing constant current on the part surfaces, setting a constant electrolyte potential along the given boundary that satisfies the current value setting.

3.2.1.6 Mesh Creation

The meshes were created with predefined sizes of mesh elements that are tetrahedrons, given by the software. The tetrahedrons are the standard type of 3D elements in *COMSOL*, providing nine mesh predefined sizes, with the characteristics shown on table 3.2.

Table 3.2: Mesh elements properties.

Mesh Quality Index		Element size (mm)	
		Minimum	Maximum
Extremely Coarse	(1)	2.45	17.5
Extra Coarse	(2)	1.89	10.5
Coarser	(3)	1.4	6.65
Coarse	(4)	0.98	5.25
Normal	(5)	0.63	3.5
Fine	(6)	0.35	2.8
Finer	(7)	0.14	1.93
Extra Fine	(8)	0.0525	1.23
Extremely Fine	(9)	0.007	0.7

The indexes presented in table 3.2 (1) to (9) are introduced to be used later when the convergence of results is evaluated.

3.2.2 Sensitivity Analysis

Firstly, in order to get reliable results, a mesh refinement was performed, in order to verify with which size of elements a convergence of the results would be obtained. Then, the next variants were iterated: external electric potential, average current density, electrolyte conductivity and temperature. The experimental results obtained by Salama et al. [1] were used to validate the models where the parameters of the FEA software *COMSOL – Corrosion Module* were iterated and, doing that, indicate what models should be selected to continue on the sensitivity analysis. Therefore, it would be obtained a good correlation between simulations and experiments. This sensitivity analysis was performed as demonstrated in the scheme in figure 3.13, where the first step of the analysis is, as already stated, the mesh refinement. Then the next steps were iterating the values for the EEP and ACD boundary condition, the Electrolite Conductivity, and lastly, the Temperature.

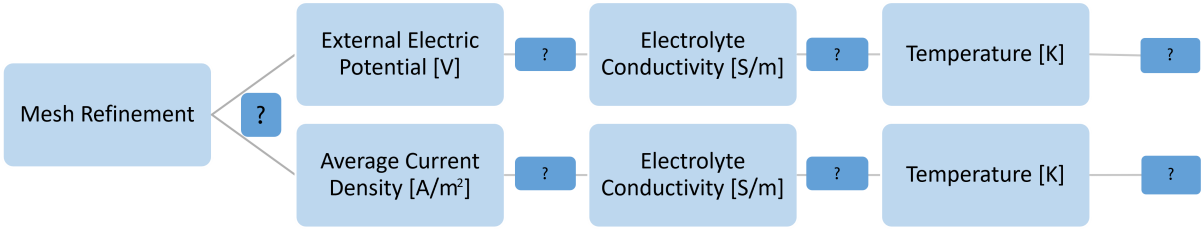

Figure 3.13: Sensitivity analysis scheme.

Also, the positioning of the specimen and the volume of the electrolyte were analysed to identify their

implications in the results. The simulations data gathered in this work can be further applied, for example, on the analysis of specimens with complex geometries which are difficult to manufacture.

3.2.2.1 Mesh Refinement

COMSOL allows for two types of mesh refinement: 1) on boundaries, refining the mesh on the boundaries selected and creating a normal mesh (quality index 5 from table 3.2) on the rest of the domain, also named as ”Local refinement mesh”, where the mesh was refined at the boundary of the iron sample; 2) on the domain, creating a mesh with equal properties all over the domain, also denoted by ”Global refinement mesh”, where every element of the mesh including the electrolyte was refined. Both of the processes were used to evaluate the mesh refinement. The Local Refinement meshes are represented in figure 3.14, only showing the mesh in the bulk surface for better analysing.

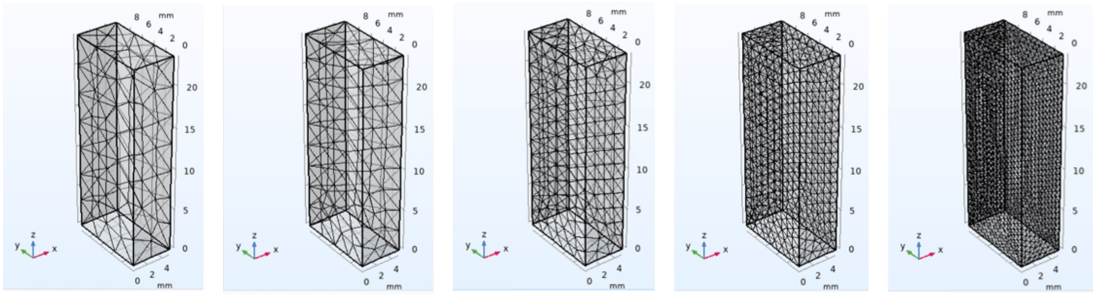

Figure 3.14: Local refinement meshes (a) Mesh Quality: Normal (5); (b) Mesh Quality: Fine (6); (c) Mesh Quality: Finer (7); (d) Mesh Quality: Extra Fine (8); (e) Mesh Quality: Extremely Fine (9).

For the *Local Refinement Mesh* in figure 3.14, the mesh with *Normal* quality is the first mesh presented because *COMSOL* could not create a coarser mesh in the bulk specimen boundaries - specifically, for the mesh quality indexes (1) to (5), the mesh created always had the element size from the quality index (5). So, from *Extremely Coarse* (1) until *Coarse* (4) quality, from the mesh quality indexes on table 3.2, the mesh is always the same. Additionally, in figure 3.15 it is shown the entire mesh of the mesh qualities *Normal* (5), *Finer* (7) and *Extremely Fine* (9), where it is possible to verify that the mesh in the domain is always the same.

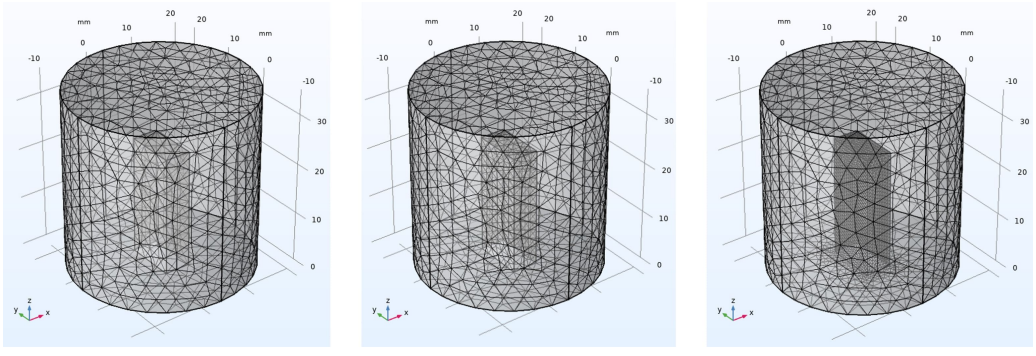

Figure 3.15: Local refinement entire meshes (a) Mesh Quality: Normal (5); (b) Mesh Quality: Finer (7); (c) Mesh Quality: Extremely Fine (9).

The Global Refinement meshes are represented in figure 3.16.

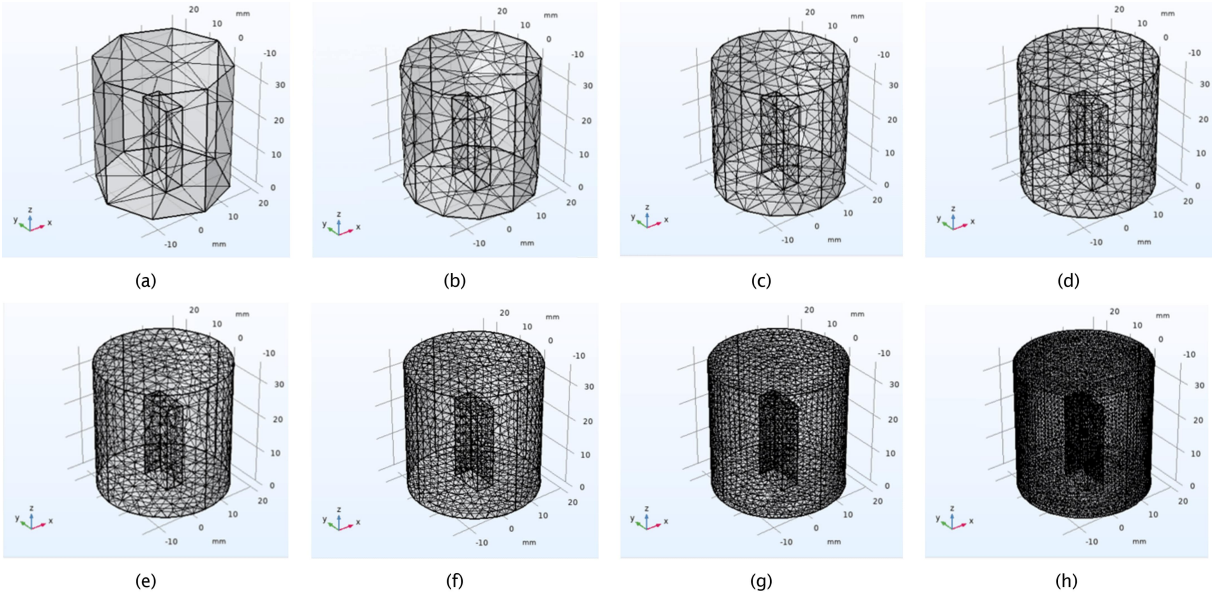

Figure 3.16: Global refinement meshes (a) Mesh Quality: Extremely Coarse (1); (b) Mesh Quality: Extra Coarse (2); (c) Mesh Quality: Coarser (3); (d) Mesh Quality: Coarse (4); (e) Mesh Quality: Normal (5); (f) Mesh Quality: Fine (6); (g) Mesh Quality: Finer (7); (h) Mesh Quality: Extra Fine (8).

As it is possible to verify observing figures 3.16(a) to 3.16(h), when refining all the domain all the elements change equally. This contrasts with what happened in figure 3.15, where only the mesh close to the bulk surfaces were refined.

The study of mesh refinement for results convergence was performed with a corrosion analysis for the bulk specimen during 28 days.

3.2.2.2 Mechanical Properties

As the type of study defined for the iron corrosion analysis in Section 3.2.1.1 mainly involves chemistry equations, two different models were used to verify if the mechanical properties of the iron would influence or not the results, 1) with the mechanical properties inserted in the model, and 2) without mechanical properties in the model. To evaluate the difference, an analysis up to 730 days (two years) was performed.

3.2.2.3 Influence of changes in time

In order to evaluate the influence of time in the numerical simulations, some variations were made in the time at which the results were observed, specifically, instead of looking at the results only after 168 hours (7 days). It was checked what would happen if the results of mass change were compared with 4 hours before or 4 hours after those 168h. This 4 hour interval was chosen based on possible unexpected events that would change the time at which the specimens were taken out of the SBF in the experimental tests.

3.2.2.4 Sharma and Čapek polarization curves

Before starting to analyse the influences of changing the parameters in the EEP and ACD boundary conditions, some models were created to evaluate the differences in using these two different polarization curves, and understand if it would be worth it to use both. Consequently, four models were created: two for each polarization curve, being one of the models regulated by ACD boundary condition, and the other by EEP boundary condition.

For both of the models with the two different polarization curves, the OCP value used in EEP boundary condition was -0.636 V, from Wagener et al. [94], as seen on Section 2.3.2. Regarding the average current density applied in the ACD models, in the model of the Čapek polarization curve was applied the value taken from the curve, 0.0125 A/m^2, and in the Sharma polarization curve was applied 0.0523 A/m^2. This was the value chosen for the Sharma polarization curve in order to have applied two $i_{average}$ taken with Tafel extrapolation rules from the curves, as stated in Section 2.3.3, and this value was closer with the one in Sharma and Pandey [78].

3.2.2.5 External Electric Potential (EEP) boundary condition

As previously mentioned two models were studied, specifically External Electric Potential (EEP) boundary condition and Average Current Density (ACD) boundary condition. For the former model, it was necessary to find the value of voltage applied on the specimen boundaries, $\phi_{s,ext}$, that would result on similar values of mass change on the experimental tests. As seen on Section 2.3.2, from Wagener et al. [94] two different values were used to verify the influences in the results: -0.68 and -0.636 V. Also, this variable value was iterated until the numerical results were similar to the experimental ones. In order to easily compare the numerical results with the experimental ones, the deviation value computed in this dissertation is given by:

$$\text{Deviation}(\%) = \frac{\text{Numerical result - Experimental result}}{\text{Experimental result}} \times 100(\%) \tag{3.9}$$

3.2.2.6 Average Current Density (ACD) boundary condition

For the model of average current density, $i_{average}$, in the boundaries, adequate values for the current density needed to be found, in order to get similar values to the mass change verified in the experimental tests. The values iterated are the ones presented in Section 3.2.1.3. From Sharma polarization curve the values obtained were 0.1153, 0.0523 and 0.015 A/m^2, while with the Čapek's polarization curve the value chosen was 0.0125 A/m^2. Also, following the values from the literature, those were iterated until similar results to the experimental ones were obtained.

3.2.2.7 Electrolyte conductivity, κ

According to the plot in figure 3.17 and as referred on Section 3.2.1.4, the electrolyte conductivity was iterated to observe its influence in the results. The three values used are represented in figure 3.17.

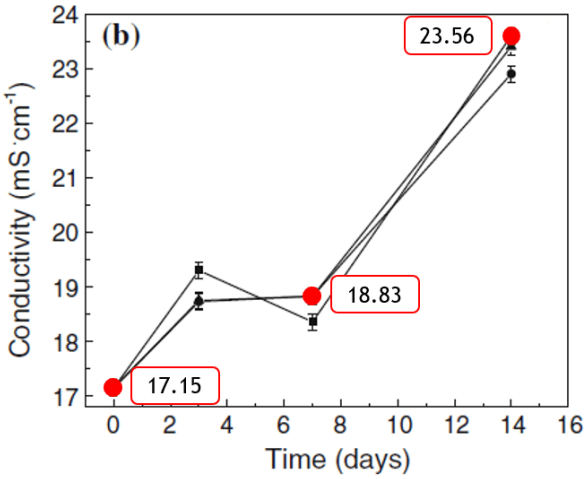

Figure 3.17: Electrolyte conductivity values. Adapted from Magyari et al. [92].

The three different values in time considered were converted to SI units, and are therefore 1.715, 1.883 and 2.356 S/m.

Following the statements made and the values, simulations were made with the conclusions taken out from Section 3.2.2.5. So, the EEP boundary conditions concluded from Section 3.2.2.5 were used to iterate κ (following the sensitivity analysis scheme in figure 3.13 in Section 3.2.2).

3.2.2.8 Temperature, T

Additionally to the value considered and already presented in Section 3.2.1.3, which is $T = 37\ ^\circ$C, a variation of this value was also considered to understand if it would change the results. In Section 2.2 it is referred that in Salama et al. [1] the temperature had a variation of $\pm\ 1\ ^\circ$C, being that the variation of the thermocouple in the equipment used. So, an excessive variation of $\pm 2^\circ$ C to the reference temperature was implemented, to guarantee that the model would be well validated.

The simulations performed to iterate the temperature value were according to the scheme in figure 3.13.

3.2.3 Sample Positioning

The positioning of the specimen in the electrolyte recipient was subsequently analysed. In the experimental conditions of Salama et al. [1], the specimen was inclined and leaned on the recipient wall. Three different positions, represented in figure 3.18, namely vertical, inclined and horizontal, were taken into account. The objective was to understand the influence of this variation in numerical results.

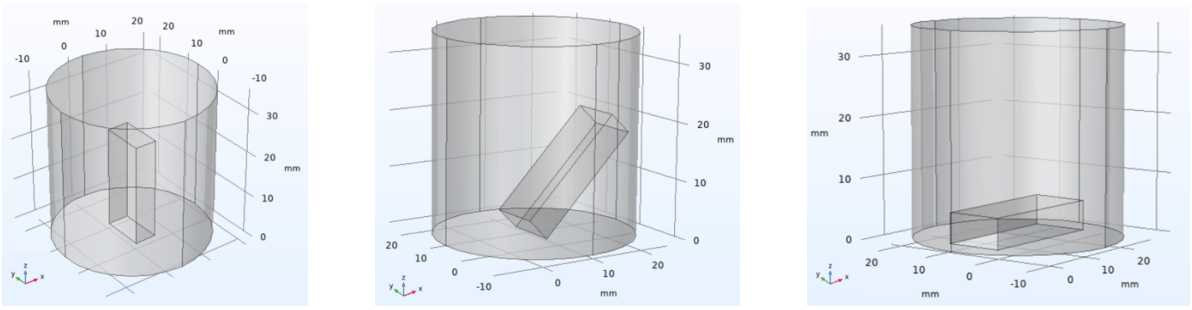

(a) (b) (c)

Figure 3.18: Specimen positioning in the electrolyte recipient (a) Vertical; (b) Inclined; (c) Horizontal.

3.2.4 Electrolyte volume

Lastly, the electrolyte volume was iterated in order to observe the influences of this variation in the mass change numerical results, developing three different configurations that are shown on figure 3.19. The original approximated volume was 32490 mm^3, while the two variations of the original recipient had the volume of 23556 and 42786 mm^3.

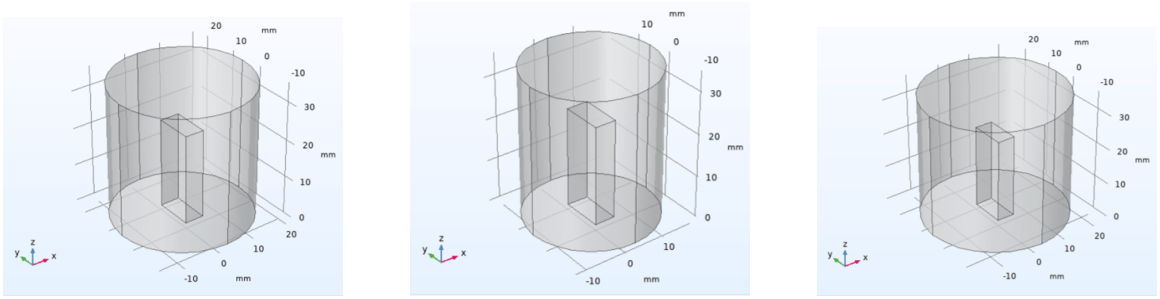

(a) (b) (c)

Figure 3.19: Variations in the electrolyte volume (a) Smaller recipient, $Volume = 23556$ mm^3; (b) Original recipient, $Volume = 32490$ mm^3; (c) Bigger recipient, $Volume = 42786$ mm^3.

For the analysis of the influence of the electrolyte volume variation, only the EEP boundary condition with $\phi_{s,ext}$ concluded from the EEP boundary condition sensibility analysis was applied.

3.2.5 Porous Specimens

After calibrating the model with the experimental results of weight loss obtained for the bulk iron specimen, the achieved parameters were applied on the porous specimens' simulations (as already mentioned in the beginning of Section 3.2), to confirm if the numerical results with small relative deviations where global. The porous specimens in *COMSOL* software are shown on figure 3.20.

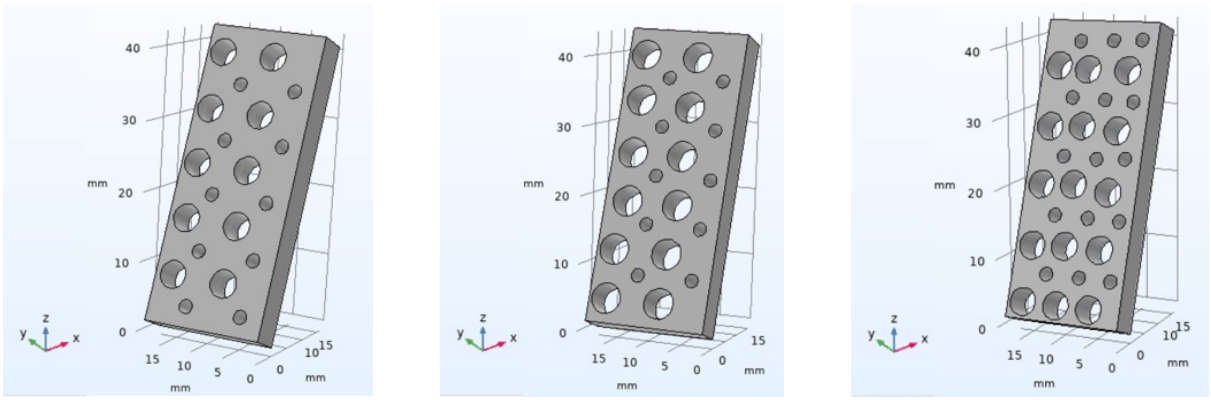

(a) (b) (c)

Figure 3.20: Porous specimens' models on *COMSOL* (a) A4_2_20 specimen; (b) A4_2_23 specimen; (c) A4_2_30 specimen.

Also, remembering the experimental procedure done in Salama et al. [1] schematized on figure 2.20, for which the amount of mass lost was measured, three different methods of performing numerical analysis were carried out (it is also shown in figure 3.21):

- (A) Continuous analysis of 28 days: equivalent of measuring the weight of the samples every 7 days, in a hypothetical case where the mass could be measured without taking the specimen out of the electrolyte medium;
- (B) Phased analysis of 28 days: involving 4 different analysis, where the mesh at the 7th day (and then 14th and 21st) is exported, to run a new analysis (similar to the experimental method);
- (C) Analysis of 42 days: only computing the volume at the 42nd day, without ever changing the electrolyte.

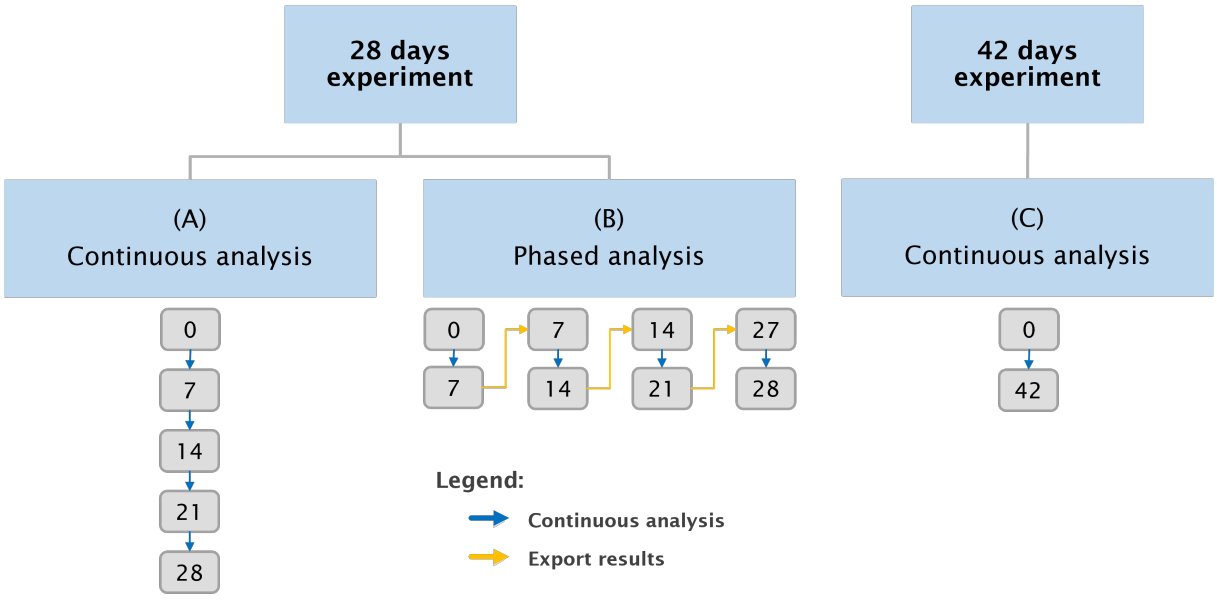

Figure 3.21: The three different methods to analyse the porous specimens.

Chapter 4

Results and Discussion

This chapter presents the results obtained for the mechanical tests, tensile and compression tests, and the results for the numerical simulations, including the results from the calibration analysis which conclusions are then used on the porous specimens.

The results obtained are also discussed. For the mechanical tests, the results are compared to the available data in the literature. The numerical tests are compared with the experimental results by Salama et al. [1]. In the next tables, the deviation or percentage error between the simulation and the experimental values will be presented.

4.1 Mechanical Characterization

In this section, firstly the force-displacement evolution and then the true stress-true strain curves are obtained for each of the tests, tensile and compression. Then, with the strain data acquired by the DIC equipment, the results are plotted in the principal strain plane. This results could be used for further investigation on bone scaffolds, for example, to perform structural analysis or in order to try to predict failure on this type of structures.

4.1.1 Tensile Tests

The figure 4.1 shows a tensile specimen after being tested. It should be noted that the ductility of the iron was verified in a very visual way, with the presence of both the cup and cone shapes after the complete failure of the specimen.

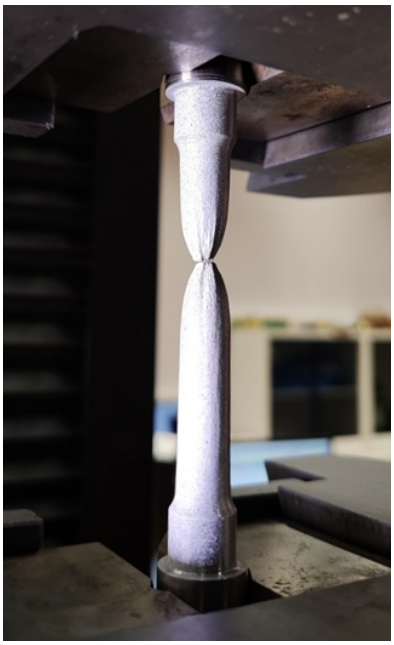

Figure 4.1: Tensile specimen after being tested.

Using the force values from the data acquired with the *Bluehill* software and the displacement values from the DIC equipment for each of the specimens, the force-displacement plot is created. To fit together the displacement and force data, since they have different origins, the last instant before failure was used as reference. It is not used the beginning of the test because the two machines could be started at different instants in time. The force-displacement evolution of the specimens is presented on figure 4.2. Unfortunately, only in two specimens the DIC equipment analysis worked until the end of the test, and consequently only two plots will be represented in the tensile results. This happened due to the high ductility of the material, and the DIC system was unable to acquire deformation points near the fracture in the other 3 specimens.

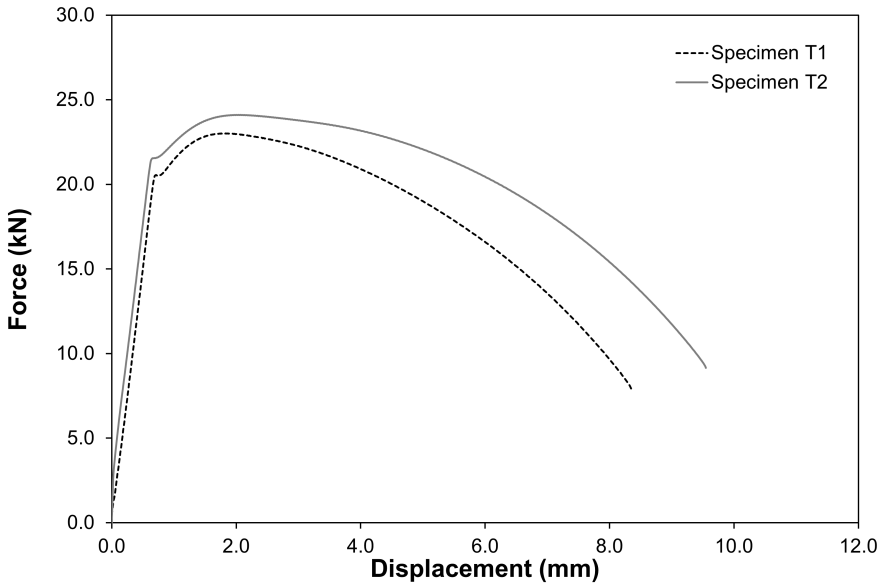

Figure 4.2: Force-displacement evolution for the two tensile specimens.

The True Stress-True Strain curves are represented in figure 4.3.

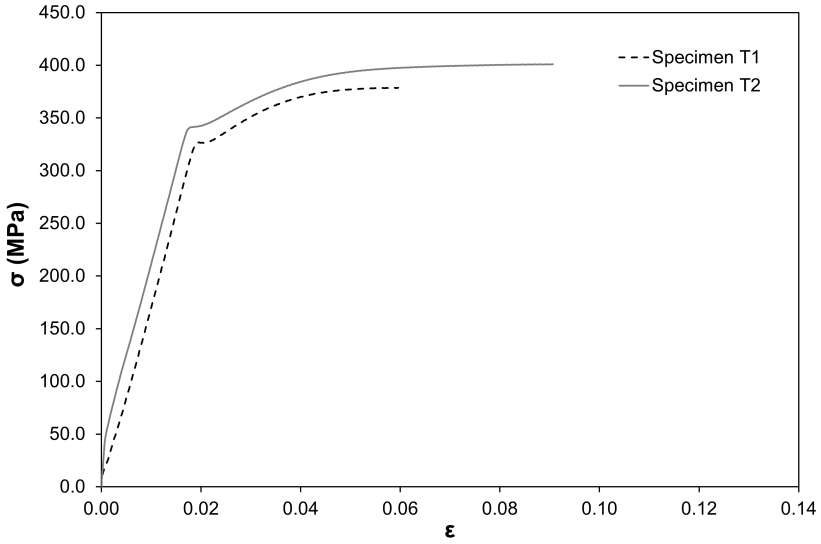

Figure 4.3: True Stress-True Strain evolution for the two tensile specimens.

Although the evolutions in the force-displacement and in the σ-ε plots of the two tensile specimens, T1 and T2, do not present a perfect coincidence, their form is similar and according to the curve available in the literature for pure iron [104].

In figure 4.4 it is represented in 2D the strain data gathered with the DIC equipment and processed with *Istra4D* for one of the tensile tests. The physical specimen is in the background, where it is easily observable the existing deformation.

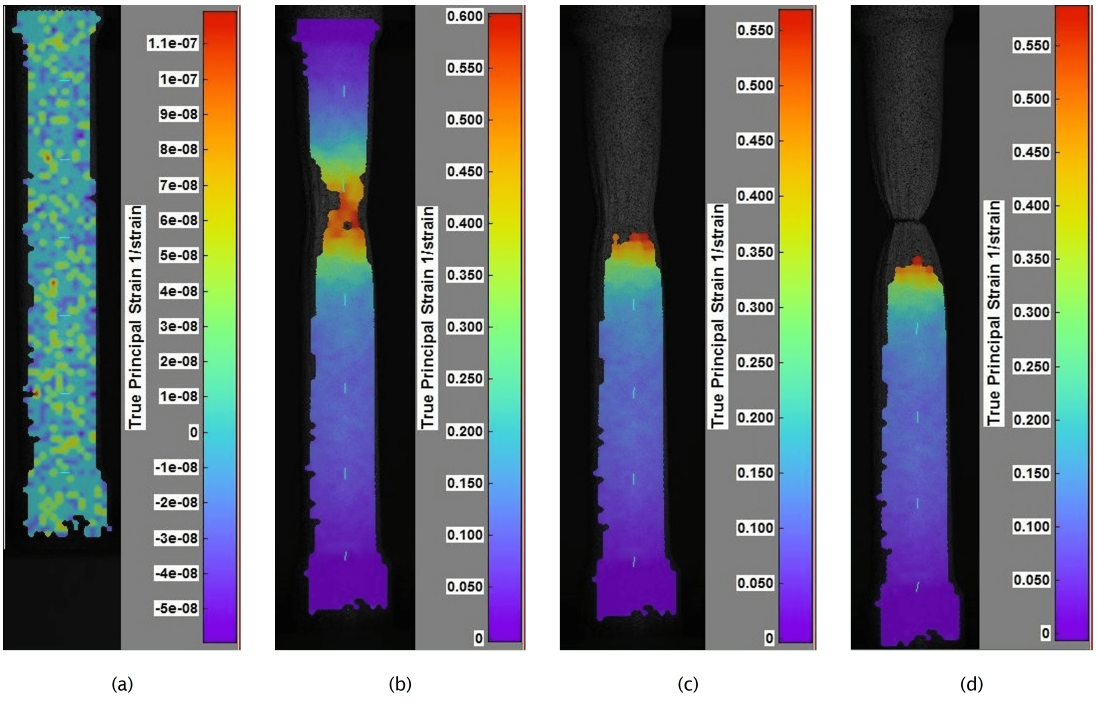

(a) (b) (c) (d)

Figure 4.4: Strain data acquired with DIC in several moments of the tensile test, 2D results: (a) beginning of the test; (b) halfway through the test, before losing data of half of the specimen; (c) after losing data of half of the specimen; (d) end of testing.

In figure 4.5 are shown the results in a 3D way that is available in *Istra4D*.

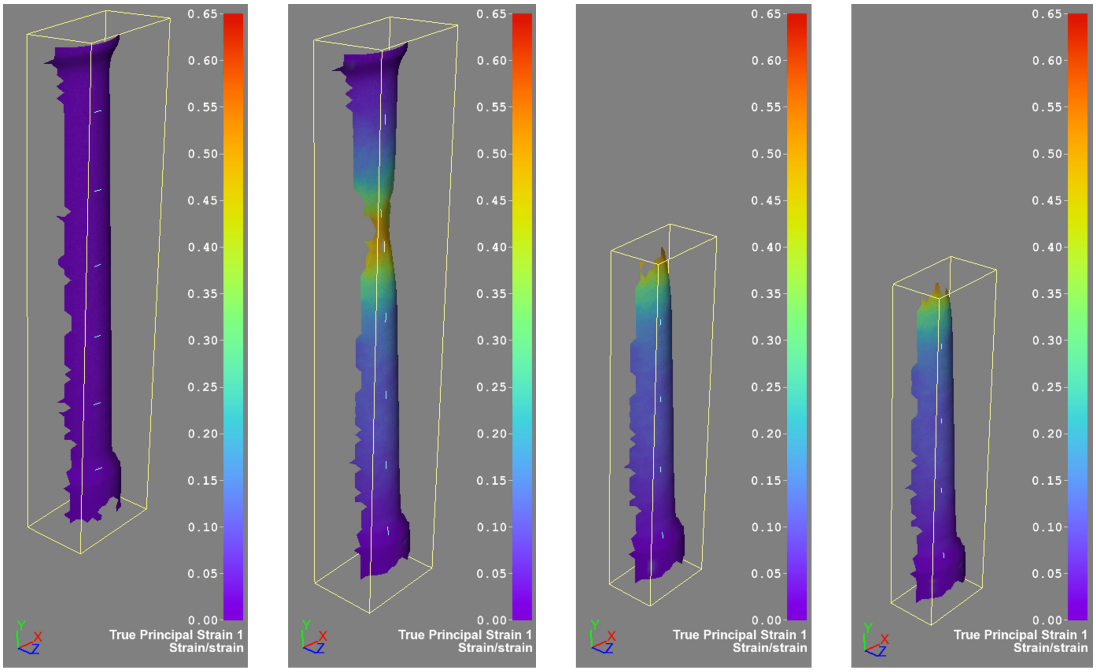

Figure 4.5: Strain data acquired with DIC in several moments of the tensile test, 3D results: (a) beginning of the test; (b) halfway through the test, before losing data of half of the specimen; (c) after losing data of half of the specimen; (d) end of testing.

The same issues reported earlier in this section were responsible for not being possible to obtain data of the entire specimen through the whole process. Also, this loss of data can influence the results, as the displacement and strain values in the middle of the specimen are not acquired.

4.1.2 Compression Tests

The figure 4.6 shows the compression specimens after being tested. It is observable that, although the Teflon® sheets were used, every specimen showed a slight barrel effect.

Figure 4.6: Compression specimens after being tested.

The force-displacement plot of the dry-run test is presented in figure 4.7, plotted to provide the trend

line function and the coefficient of determination, R^2, there represented.

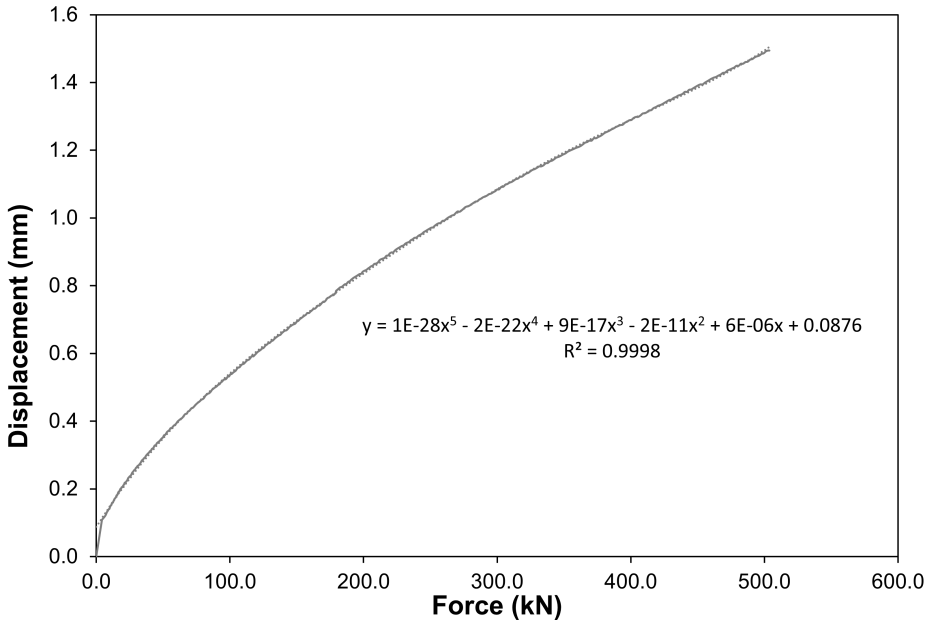

Figure 4.7: Elastic recovery displacement-force evolution.

With the trend line function, a correction factor for the displacement values is computed through the force values, and when both of the values are added, the result is the true displacement value. Figure 4.8 represents the difference of having the displacement corrected or not.

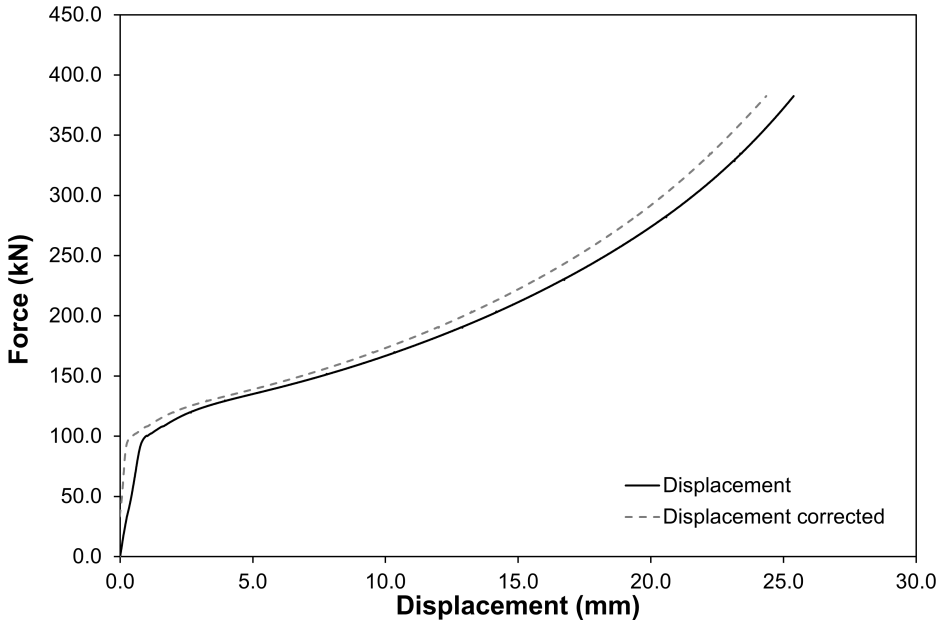

Figure 4.8: Force-displacement evolution for the compression C1 specimen, with and without the displacement corrected.

Performing the process of correcting the displacement for every specimen, the force-displacement curves are ready to be plotted. The results are in figure 4.9. It is observable that the force grows monotonically with the increase in the displacement, until the test was stopped.

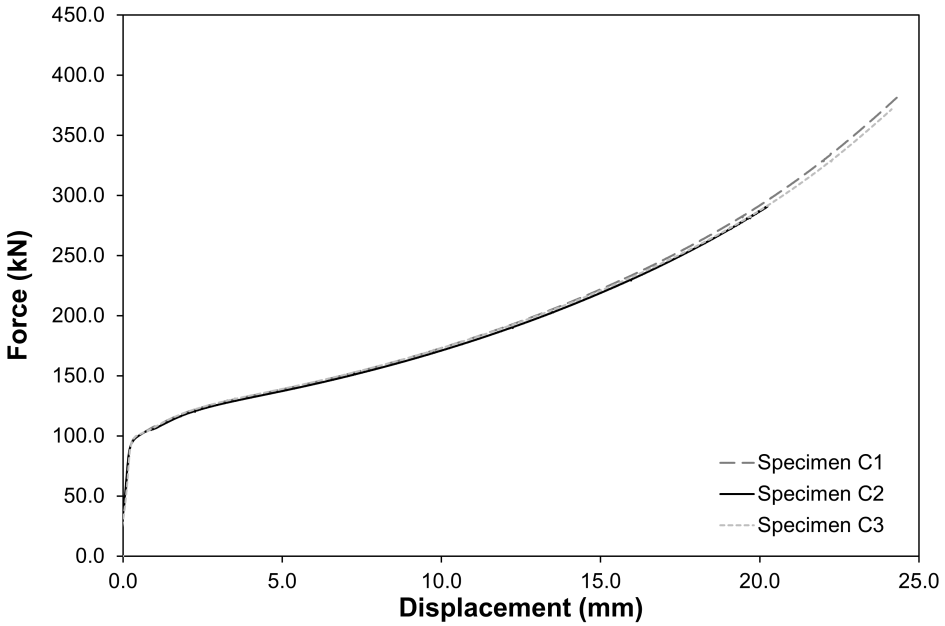

Figure 4.9: Force-corrected displacement evolution for the three compression specimens.

As it can be observed in figure 4.9, there is a good correlation between the three different plots. The True Stress-True Strain curves are represented in figure 4.10.

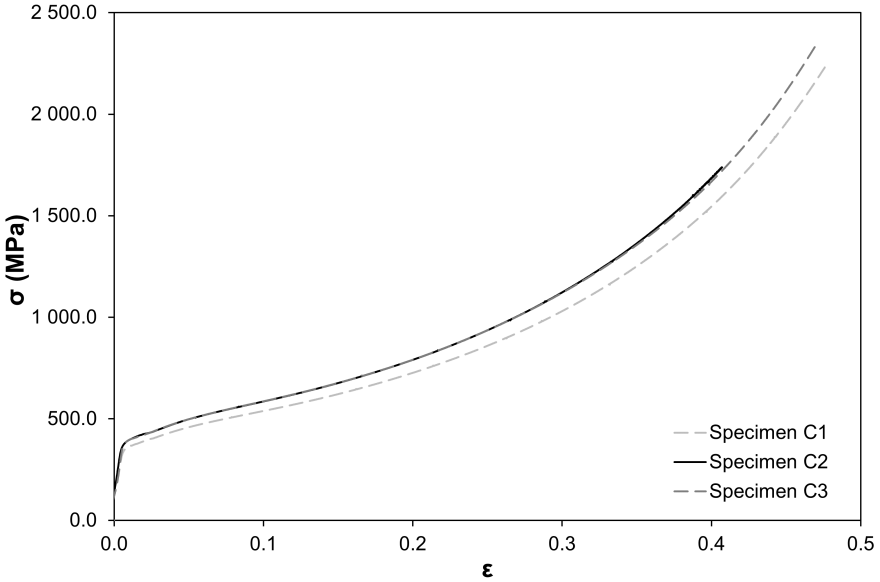

Figure 4.10: True Stress-True Strain evaluation for the three compression specimens.

In addition to the curves showing good coincidence with each other, their form is similar and according to the curves available in the literature for pure iron [104].

As it is observable from figures 4.3 and 4.10, the compression true stress-true strain evolution reaches higher strain values than the tensile ones. Consequently, the compression tests are the ones used to make the approximation of the Ludwik-Hollomon curve. After shortening the curves of the σ-ε compression tests and adding an exponential trend line, the results obtained are shown of figure 4.11.

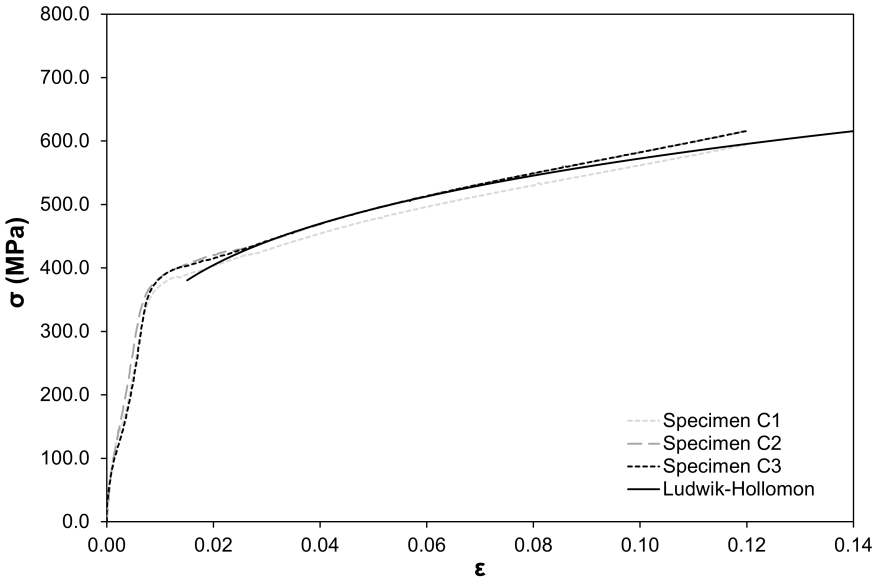

Figure 4.11: Approximation of a Ludwik-Hollomon curve to the compression tests results.

The equation of the Ludwik-Hollomon curve presented in the results is $\sigma = 941.41\varepsilon^{0.216}$.

The strain data gathered with the DIC equipment and processed with *Istra4D* for one of the compression tests is presented in 3D in figure 4.12, with three different instants of the compression test.

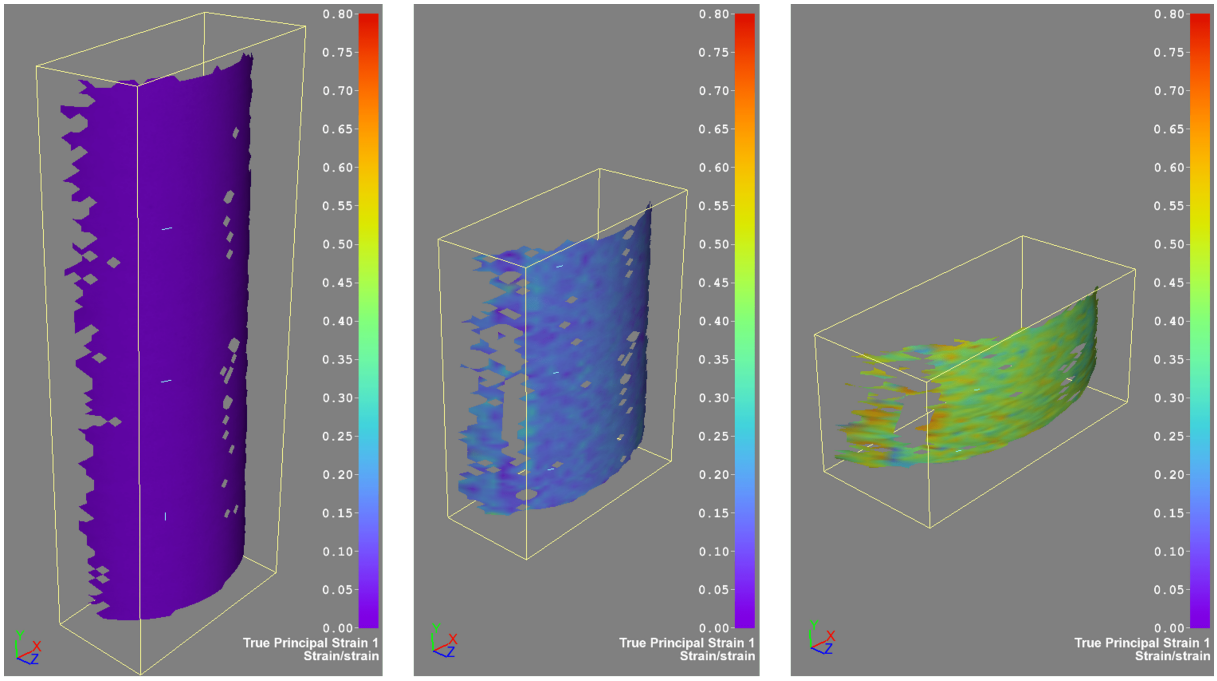

(a) (b) (c)

Figure 4.12: Strain data acquired with DIC in several moments of the compression test: (a) beginning of the test; (b) halfway through the test; (c) end of testing.

4.1.3 Principal Strain Plane

The values of the strains ε_1 and ε_2, respectively radial and axial, acquired with the DIC equipment were used to create the principal strain plane, represented in figure 4.13. Also, with dashed lines, are represented the theoretical straight lines for this type of experimental tests.

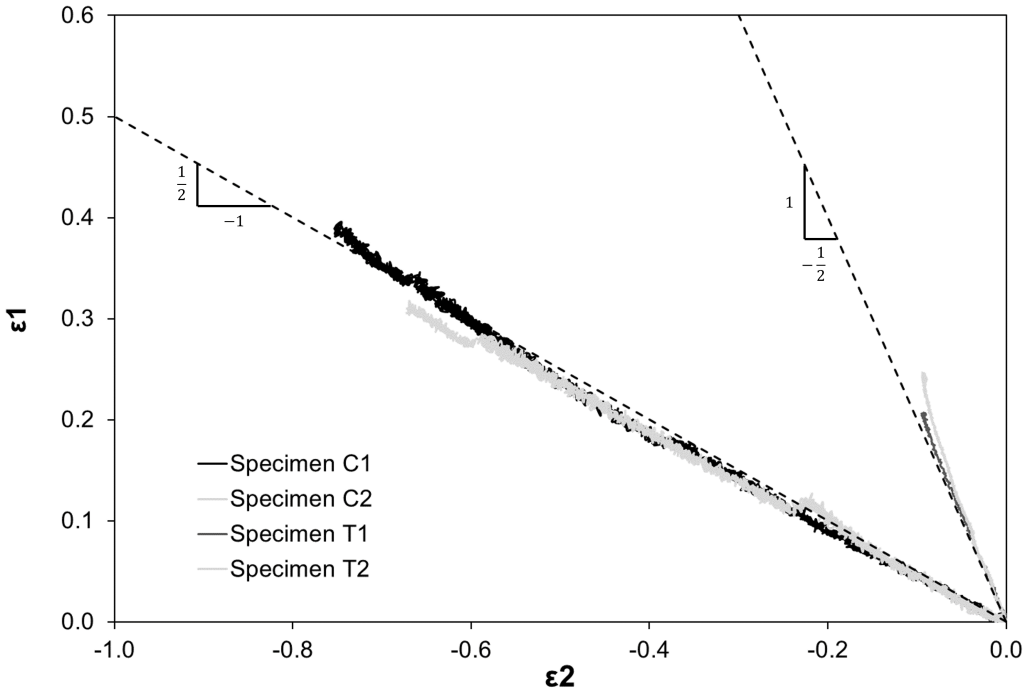

Figure 4.13: Principal strain plane from the strains measured in the tensile and compression tests.

It is observable that the specimens C1 and C2 possess a behaviour according to what is stated in the literature [104]: the ratio of ε_1 to ε_2 is $\frac{1}{2} : -1$ for uniaxial compression. The specimens T1 and T2 also possessed a behaviour according to what is stated in the literature, with the ratio of ε_1 to ε_2 being $1 : -\frac{1}{2}$, despite being more deviated from the theoretical trend line for tensile tests.

4.2 Sensitivity Analysis

4.2.1 Mesh Refinement

The results of the mesh refinement are presented in two forms: computation time, and the simulation results for mass change. The times of computation are in the table 4.1.

Table 4.1: Mesh refinement computation times.

Mesh Quality Index		Computation Time	
		Local Refinement	Global Refinement
Extremely Coarse	(1)	10 s	6 s
Extra Coarse	(2)	10 s	5 s
Coarser	(3)	10 s	5 s
Coarse	(4)	10 s	6 s
Normal	(5)	10 s	11 s
Fine	(6)	10 s	18 s
Finer	(7)	12 s	1 min 2 s
Extra Fine	(8)	19 s	6 min 24 s
Extremely Fine	(9)	44 s	1 h 48 min 55 s

The simulation results are given by the mass change in function of the mass quality index used. In this dissertation, the mass change is computed by:

$$\frac{\Delta m}{m0}(\%) = \frac{\text{Initial mass - Mass at the i}^{\text{th}}\text{ day}}{\text{Initial mass}} \times 100(\%) \qquad i = 0, 7, ..., 42 \tag{4.1}$$

The simulation results are shown in figure 4.14, presenting the values of the mass changes as a function of the mesh quality index of each model's mesh, from 1 to 9. Two curves are shown for Local refinement mesh and Global refinement mesh.

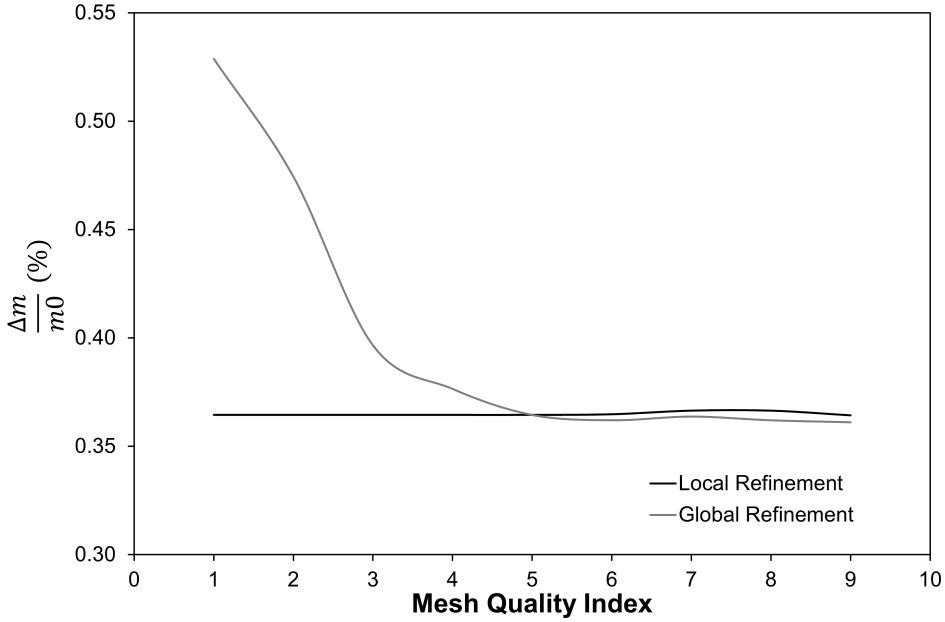

Figure 4.14: Mesh refinement results graphic.

Looking at figure 4.14 it is clearly visible that, with the Local Refinement mesh, the results with the Mesh Quality index from 1 to 5 are always the same, as the graph as a horizontal, constant shape. This proves that, using a Mesh Quality index from 1 to 5 for the bulk specimen, the mesh is always the same

(as already previously stated earlier in Section 3.2.2.1). Having in mind that this mesh refinement is being performed for later use in a porous specimen, using elements size higher than 0.63 mm (from data in table 3.2) could lead into doubtful results for the mass change, or even worse if the element size was too coarse for an optimized geometry. So, although the results seem to have already converged from mesh quality index from 1 to 9, a mesh quality poorer than *Normal* (5) could never be used. Also, looking at figures 3.16(e) to 3.16(h), it is observable that the refinement of the mesh has a lot of influence in the curvature of the recipient. As using *Local Refinement* the mesh in the domain has *Normal* (5) quality index, it was decided to not use this type of refinement, as it could lead to some errors when computing the mass change of the specimens.

Also from figure 4.14 it can be stated that for meshes as or more refined than Mesh Quality Index 6 for the Global Refinement the mass change results have already converged.

With this, it was concluded that the Global Refinement with *Finer* quality index (7) would be used, because it provides a balance between reliable results and fast simulations. This mesh is represented in figure 4.15, the same as the one presented in figure 3.16(g).

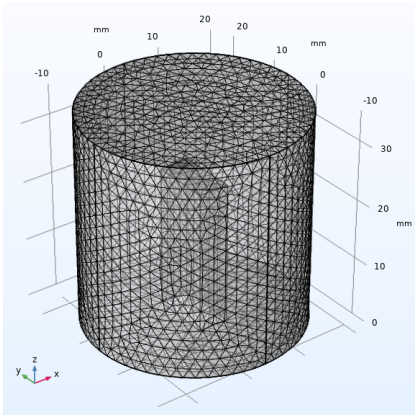

Figure 4.15: Mesh from Global Refinement with mesh quality index *Finer* (7).

4.2.2 Mechanical Properties

The results of the mechanical properties influence analysis are presented in the table 4.2. The study was done for 730 days, or 2 years, in order to have a longer time interval to analyze if the mechanical properties would influence the results or not.

Table 4.2: Variance of results with the mechanical properties at the 730th day.

Model	Volume at the 730th day (mm^3)	Difference (mm^3)
1) With mechanical properties	32658.399	0.000
2) Without mechanical properties	32658.399	

It is concluded from the results that the mechanical properties do not influence the results. However, these properties are very important if it were desirable to perform another type of analysis. For example, a simulation where a mechanical test would be performed after the corrosion of the iron specimen.

4.2.3 Influence of changes in time

The results of the simulations performed to analyse the influence of little changes in time are presented in table 4.3. It is observable that, changing the testing time at which the mass is checked, between 164 and 172 h, the results only vary by approximately 0.02%, thus considered negligible.

Table 4.3: Variance of results with little changes in time at the 7th day.

Time (h)	Mass change (g)	Mass change (%)	Difference (%)
164	0.0751	0.8401	0.0204
165	0.0756	0.8452	0.0153
166	0.0760	0.8503	0.0102
167	0.0765	0.8554	0.0051
168 (7 days)	0.0769	0.8605	-
169	0.0774	0.8656	0.0051
170	0.0779	0.8707	0.0102
171	0.0783	0.8758	0.0153
172	0.0788	0.8810	0.0204

4.2.4 Sharma and Čapek polarization curves

Following the values stated in Section 3.2.2.4 to apply in the ACD and EEP models for the two polarization curves, from Sharma and Pandey [78] and Čapek et al. [71], the simulations were performed and the results compared with the experimental results by Salama et al. [1]. The results of mass change through time are shown in figure 4.16.

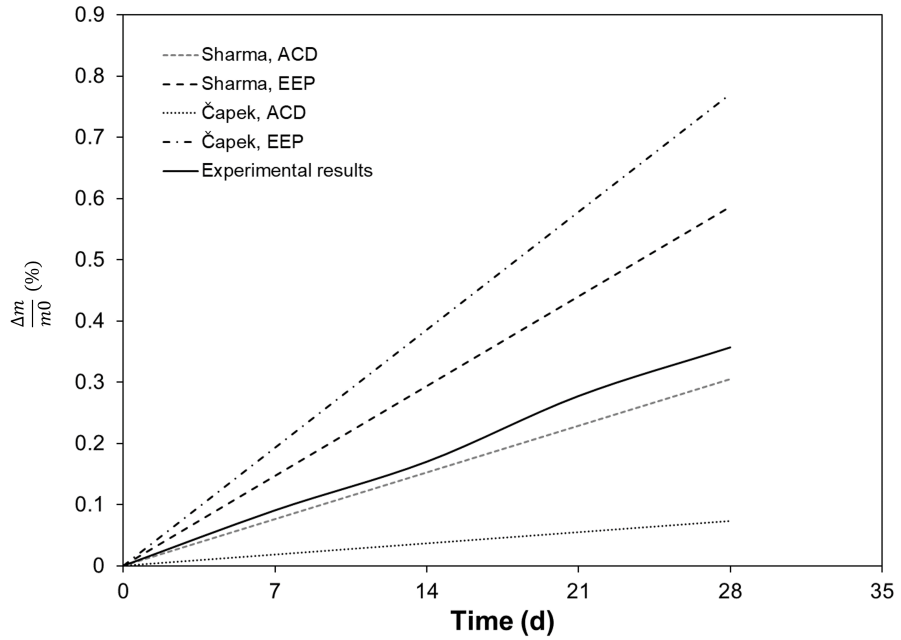

Figure 4.16: Results of mass change variation in time, with ACD and EEP boundary conditions applied in Sharma and Čapek polarization curves.

Observing the plot in figure 4.16 it is possible to conclude that the results with the models using

Sharma polarization curve, either with ACD or EEP boundary conditions, are always closer to the experimental results then the results of the models with Čapek polarization curve. Also, as already stated before in Section 2.3.3, Čapek polarization curve was obtained when using pure Fe in contact with a SBF slightly different from the one used by Salama et al. [1] and Sharma and Pandey [78]. So, the conclusion taken here was that the Čapek polarization curves would not be used anymore.

4.2.5 External Electric Potential (EEP) boundary condition

All the results from the EEP boundary condition simulations are presented in table 4.4.

Table 4.4: Results with different EEP boundary conditions applied.

Time (days)	Experimental	COMSOL									
		$\Phi_{s,ext} = -0.68$ V		$\Phi_{s,ext} = -0.636$ V		$\Phi_{s,ext} = -0.62$ V		$\Phi_{s,ext} = -0.6$ V		$\Phi_{s,ext} = -0.57$ V	
	$\frac{\Delta m}{m0}$ (%)	$\frac{\Delta m}{m0}$ (%)	Deviation (%)	$\frac{\Delta m}{m0}$ (%)	Deviation (%)	$\frac{\Delta m}{m0}$ (%)	Deviation (%)	$\frac{\Delta m}{m0}$ (%)	Deviation (%)	$\frac{\Delta m}{m0}$ (%)	Deviation (%)
0	**0.000**	**0.000**	-	**0.000**	-	**0.000**	-	**0.000**	-	**0.000**	-
7	**0.091**	**0.585**	545.240	**0.426**	370.236	**0.353**	290.120	**0.245**	170.274	**0.091**	0.442
14	**0.170**	**1.167**	586.673	**0.851**	400.641	**0.706**	315.415	**0.489**	187.877	**0.182**	7.025
21	**0.277**	**1.748**	530.362	**1.275**	359.778	**1.058**	281.572	**0.734**	164.498	**0.273**	-1.629
28	**0.357**	**2.328**	552.447	**1.699**	376.086	**1.410**	295.174	**0.978**	174.001	**0.364**	1.946

Also, the results in *COMSOL* are presented in figure 4.17.

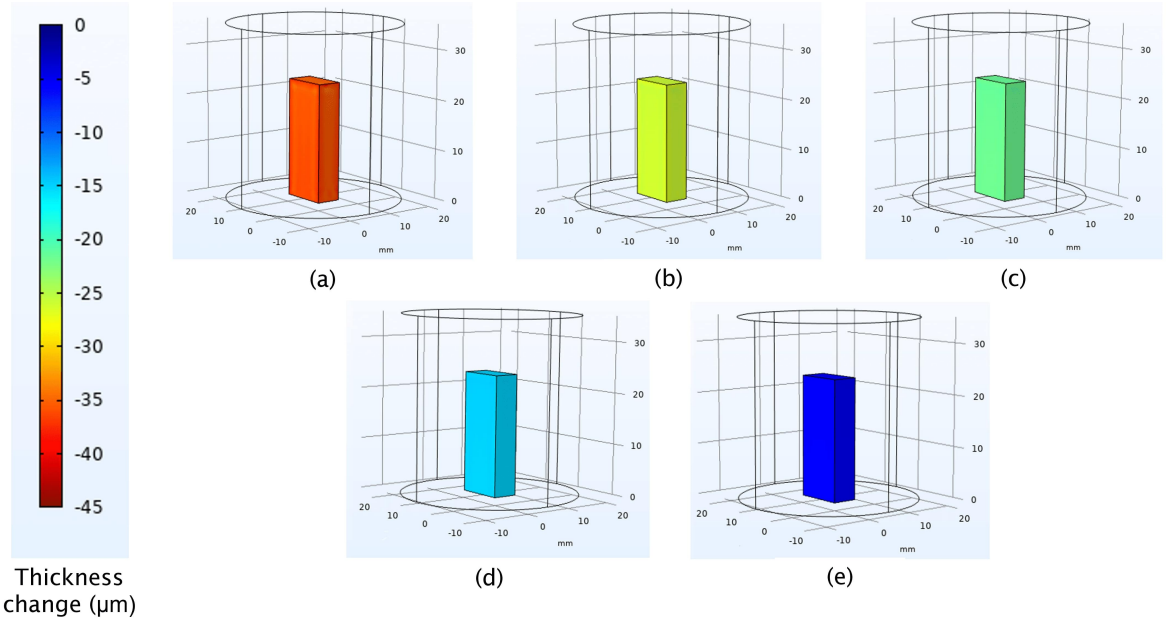

Figure 4.17: EEP boundary conditions results (a) $\phi_{s,ext} : -0.68V$; (b) $\phi_{s,ext} : -0.636V$; (c) $\phi_{s,ext} : -0.62V$; (d) $\phi_{s,ext} : -0.6V$; (e) $\phi_{s,ext} : -0.57V$.

Analysing the results in table 4.4, it is assumable that the $\phi_{s,ext}$ values from Section 3.2.2.5 create an extremely corrosive medium: the deviation is higher than 350 % when using the value with the correct reference electrode (when $\phi_{s,ext}$ is -0.636 V). The $\phi_{s,ext}$ value was increased until the deviation was almost null, with -0.57 V. From another point of view, observing figure 4.17, it is possible to state that the different levels of EEP applied caused corrosion at different stages, but always uniform in all the specimen surfaces.

To conclude, from the sensitivity analysis, the values to go on are -0.6 V and -0.57 V: the first one due to the fact that is the more correct according to the literature, as it gives the most similar results when compared with experimental ones, and the second one due to the accuracy of the results when compared to the experimental results of Salama et al. [1].

4.2.6 Average Current Density (ACD) boundary condition

Following what was described in Section 3.2.2.6, simulations results were obtained and are registered in table 4.5 for the iterated values after the literature average current density in Sharma and Pandey [78].

Table 4.5: Results with different ACD boundary conditions applied (1).

Time (days)	Experimental	COMSOL									
		$i_{average}$ = 0.1153 A/m²		$i_{average}$ = 0.1053 A/m²		$i_{average}$ = 0.1 A/m²		$i_{average}$ = 0.01 A/m²		$i_{average}$ = 0.062 A/m²	
	$\frac{\Delta m}{m0}$ (%)	$\frac{\Delta m}{m0}$ (%)	Deviation (%)	$\frac{\Delta m}{m0}$ (%)	Deviation (%)	$\frac{\Delta m}{m0}$ (%)	Deviation (%)	$\frac{\Delta m}{m0}$ (%)	Deviation (%)	$\frac{\Delta m}{m0}$ (%)	Deviation (%)
0	**0.000**	**0.000**	-	**0.000**	-	**0.000**	-	**0.000**	-	**0.000**	-
7	**0.091**	**0.168**	85.336	**0.153**	69.268	**0.146**	60.751	**0.015**	-83.920	**0.090**	-0.320
14	**0.170**	**0.336**	97.448	**0.307**	80.336	**0.291**	71.265	**0.029**	-82.863	**0.181**	6.214
21	**0.277**	**0.503**	81.449	**0.460**	65.730	**0.437**	57.397	**0.044**	-84.245	**0.271**	-2.374
28	**0.357**	**0.671**	88.007	**0.613**	71.726	**0.582**	63.095	**0.058**	-83.670	**0.361**	1.174

Also, the *COMSOL* results are in figure 4.18.

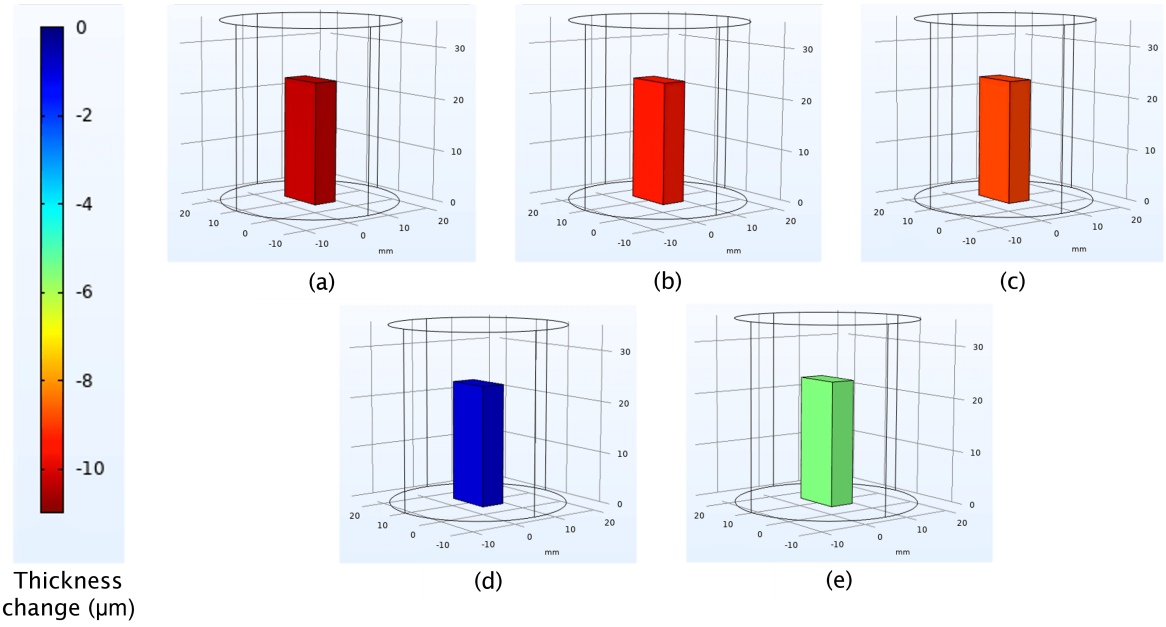

Figure 4.18: ACD boundary conditions results (1) (a) $i_{average}$: 0.1153 A/m²; (b) $i_{average}$: 0.1053 A/m²; (c) $i_{average}$: 0.1 A/m²; (d) $i_{average}$: 0.01 A/m²; (e) $i_{average}$: 0.062 A/m².

Continuing, in table 4.6 are the results for the values taken out of Sharma curve with Tafel Extrapolation rules by Fontana [95].

Table 4.6: Results with different ACD boundary conditions applied (2).

Time (days)	Experimental	COMSOL			
		$i_{average} = 0.0523$ A/m²		$i_{average} = 0.015$ A/m²	
	$\frac{\Delta m}{m0}$ (%)	$\frac{\Delta m}{m0}$ (%)	Deviation (%)	$\frac{\Delta m}{m0}$ (%)	Deviation (%)
0	**0.000**	**0.000**	-	**0.000**	-
7	**0.091**	**0.076**	-15.912	**0.022**	-100.137
14	**0.170**	**0.152**	-10.397	**0.044**	-100.420
21	**0.277**	**0.228**	-17.639	**0.066**	-100.372
28	**0.357**	**0.305**	-14.643	**0.087**	-100.597

In figure 4.19 are the results in *COMSOL* for this last average current density values.

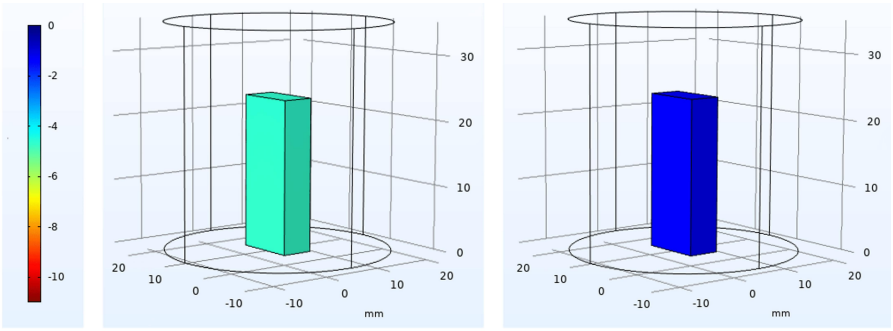

Figure 4.19: ACD boundary conditions results(2) (a) $i_{average}$: 0.0523 A/m^2; (b) $i_{average}$: 0.0150 A/m^2.

As before, it was observed that the corrosion happened uniformly over the whole surface of the specimen, only at different levels due to the different levels of average current density applied.

Analysing the results, it was decided that the values that would be used in the following simulations were 0.1153 A/m^2 and 0.0523 A/m^2. The former value was the value in the paper of Sharma and Pandey [78] and the deviation obtained was not excessive, while the latter was obtained with the Tafel Extrapolation applied on the Sharma polarization curve, according to Fontana [95] (as explained of Section 2.3.3), that gave the more accurate results when compared to the experimental results in Salama et al. [1].

4.2.7 Electrolyte conductivity, κ

The results of the simulations referred in Section 3.2.2.7 are presented in this section. The results of the simulations using OCP value of -0.6 V is presented in table 4.7.

Table 4.7: Results with different κ and EEP boundary condition of -0.6 V.

Time (days)	Experimental	COMSOL					
		$\kappa = 1.715$ S/m		$\kappa = 1.883$ S/m		$\kappa = 2.356$ S/m	
	$\frac{\Delta m}{m0}$ (%)	$\frac{\Delta m}{m0}$ (%)	Deviation (%)	$\frac{\Delta m}{m0}$ (%)	Deviation (%)	$\frac{\Delta m}{m0}$ (%)	Deviation (%)
0	**0.000**	**0.000**	-	**0.000**	-	**0.000**	-
7	**0.091**	**0.245**	170.950	**0.245**	170.046	**0.243**	168.212
14	**0.170**	**0.491**	188.597	**0.489**	187.635	**0.486**	185.683
21	**0.277**	**0.735**	165.158	**0.733**	164.275	**0.728**	162.484
28	**0.357**	**0.980**	174.685	**0.977**	173.771	**0.970**	171.918
Average deviation (%)		-	172.817	-	171.908	-	170.065

The results of the simulations using OCP value of -0.57 V is represented in table 4.8.

Table 4.8: Results with different κ and EEP boundary condition of -0.57 V.

Time (days)	Experimental	COMSOL					
		$\kappa = 1.715$ S/m		$\kappa = 1.883$ S/m		$\kappa = 2.356$ S/m	
	$\frac{\Delta m}{m0}$ (%)	$\frac{\Delta m}{m0}$ (%)	Deviation (%)	$\frac{\Delta m}{m0}$ (%)	Deviation (%)	$\frac{\Delta m}{m0}$ (%)	Deviation (%)
0	**0.000**	**0.000**	-	**0.000**	-	**0.000**	-
7	**0.091**	**0.091**	0.705	**0.091**	0.353	**0.090**	-0.361
14	**0.170**	**0.182**	7.305	**0.182**	6.930	**0.180**	6.170
21	**0.277**	**0.274**	-1.371	**0.271**	-1.716	**0.271**	-2.414
28	**0.357**	**0.365**	2.212	**0.363**	1.856	**0.361**	1.132
Average deviation (%)		-	1.459	-	1.104	-	0.386

Lastly, figure 4.20 shows the *COMSOL* results of one of the simulations, the one with OCP of -0.57 V and κ of 2.356 S/m. Only these results are shown because using OCP of -0.6 V the deviations were rather higher, and using OCP of -0.57 V the results are very similar.

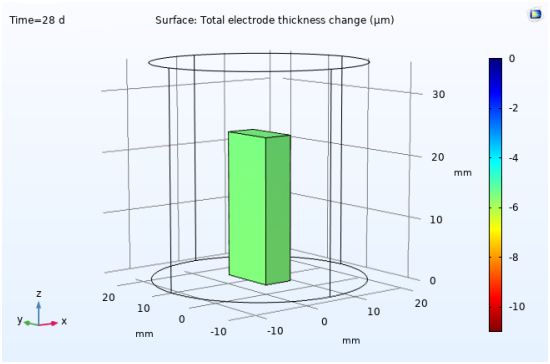

Figure 4.20: *COMSOL* results with EEP boundary condition of -0.57 V and κ of 2.356 S/m.

Observing the results, it is easily concluded that changing the electrolyte conductivity almost does not influence the results. The deviation varies, at most, by approximately 2.8% when using OCP of -0.6 V (and looking at the mass change, it only changes 0.01%). The value that will be used henceforward is 2.356 S/m because this value was for the 14th day (according to the figure 3.17), and the majority of the simulations was for 28 days: thus represents the value for the middle of the evaluated period. Also,

it is the value that has less deviation.

4.2.8 Temperature, T

The results for the temperature influence simulations are in table 4.9.

Table 4.9: Results with different temperatures, for different boundary conditions.

		Mass change after 28 days, $\frac{\Delta m}{m0}$ (%)			Experimental Results
		35 ºC	37 ºC	39 ºC	37 ºC
EEP Boundary Condition (V)	-0.6	0.97016	0.97016	0.97016	0.35678
	-0.57	0.36082	0.36082	0.36082	
ACD Boundary Condition (A/m²)	0.1153	0.67078	0.67078	0.67078	
	0.0523	0.30454	0.30453	0.30454	

The result for one of the models in *COMSOL* is presented in figure 4.21. Only one image is presented, since the results are almost identical.

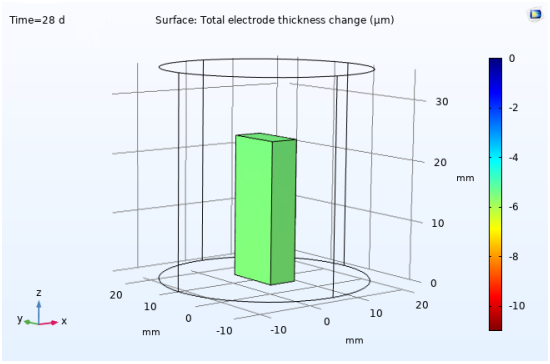

Figure 4.21: *COMSOL* results with EEP boundary condition of -0.57 V, κ of 2.356 S/m and 37 ° C.

It is observed that the variation of $\pm$ 2 ° C does not influence the numerical results, thus the value for the temperature variable will always be 37 ° C.

4.2.9 Sensitivity analysis conclusions

With the temperature value iterated, it is possible to conclude the sensitivity analysis and complete the scheme in figure 3.13. The scheme completed is shown in figure 4.22.

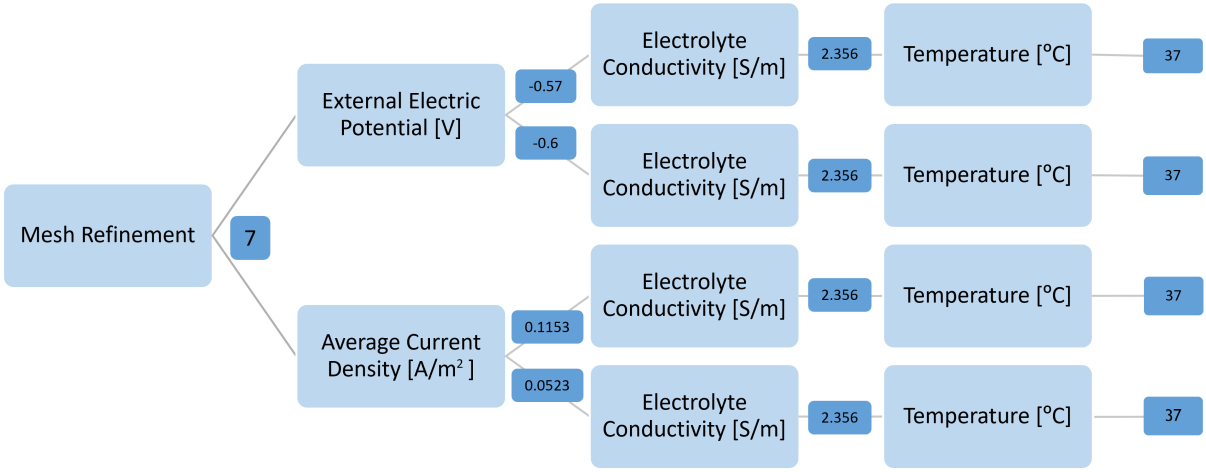

Figure 4.22: Sensitivity analysis scheme completed.

With this, the table 4.10 was created to resume the iterated values. These values are going to be used for the simulations in Section 4.2.10, Section 4.2.11 and Section 4.3.

Table 4.10: Iterated variables to use in *COMSOL*.

	Variable	Values
Polarization Curve	ilocmat	-
-Equilibrium Potential (V)	E_{eq}	-0.545
-Average Current Density (A/m)	$i_{average}$	0.1153 0.0523
Temperature (º C)	T	37
Electrolyte Conductivity (S/m)	κ	2.356
External Electric Potential (V)	$\Phi_{s,ext}$	-0.6 -0.57

4.2.10 Sample Positioning

For this analysis, both boundary conditions were used: EEP and ACD. As was presented in the figure 3.18 in Section 3.2.3, the caption for the positioning in the recipient is the following: (a) vertical; (b) inclined; (c) horizontal. The results of the simulations using the EEP boundary conditions are shown on table 4.11.

Table 4.11: Results with EEP boundary condition applied: -0.57 V.

Time (days)	Experimental	COMSOL					
		Vertical		Inclined		Horizontal	
	$\frac{\Delta m}{m0}$ (%)	$\frac{\Delta m}{m0}$ (%)	Deviation (%)	$\frac{\Delta m}{m0}$ (%)	Deviation (%)	$\frac{\Delta m}{m0}$ (%)	Deviation (%)
0	**0.000**	**0.000**	-	**0.000**	-	**0.000**	-
7	**0.091**	**0.090**	-0.361	**0.097**	7.029	**0.069**	-24.221
14	**0.170**	**0.180**	6.170	**0.194**	14.042	**0.137**	-19.253
21	**0.277**	**0.271**	-2.414	**0.291**	4.819	**0.206**	-25.780
28	**0.357**	**0.361**	1.132	**0.388**	8.625	**0.274**	-23.082

Also, the results of the simulations using the ACD boundary conditions are shown on table 4.12.

Table 4.12: Results with ACD boundary condition applied: 0.0523 A/m^2.

Time (days)	Experimental	COMSOL					
		Vertical		Inclined		Horizontal	
	$\frac{\Delta m}{m0}$ (%)	$\frac{\Delta m}{m0}$ (%)	Deviation (%)	$\frac{\Delta m}{m0}$ (%)	Deviation (%)	$\frac{\Delta m}{m0}$ (%)	Deviation (%)
0	**0.000**	**0.000**	-	**0.000**	-	**0.000**	-
7	**0.091**	**0.076**	-15.914	**0.081**	-10.454	**0.058**	-36.265
14	**0.170**	**0.152**	-10.399	**0.162**	-4.582	**0.115**	-32.084
21	**0.277**	**0.228**	-17.641	**0.243**	-12.295	**0.173**	-37.572
28	**0.357**	**0.305**	-14.644	**0.324**	-9.106	**0.231**	-35.300

Lastly, the results in *COMSOL* are shown on figure 4.23.

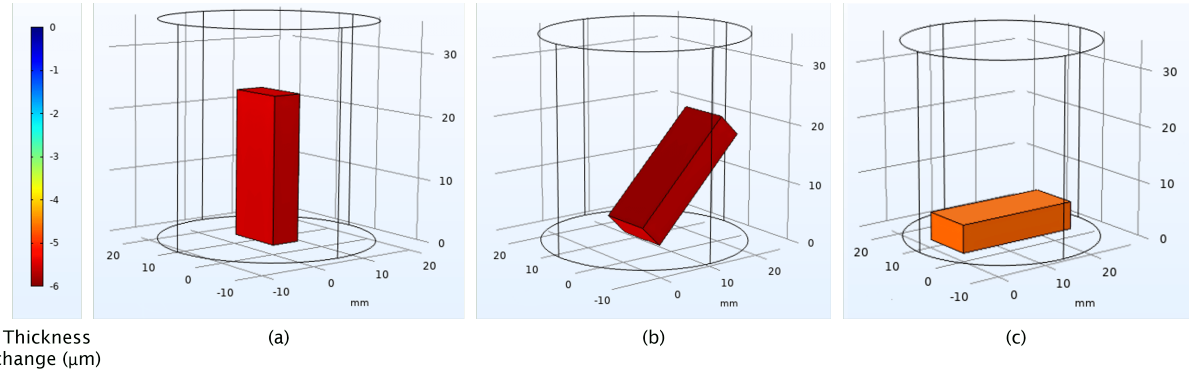

Figure 4.23: Results with different ways of positioning the specimen (a) legend; (b) vertical; (c) inclined; (d) horizontal.

Firstly, it is necessary to have in mind that the quantitative results in this section are not that important, at least for the EEP boundary condition, because the calibration of the value of the potential applied on the EEP boundary condition was made also with the specimen in a vertical position, so the results with lower relative deviation would always be from the vertical specimen. Also, as already stated, the objective was to verify the influences of changing the position of the specimens in the mass change. For this specific reason, the *COMSOL* results of only one of the models are shown.

From these results it is verified what is known from the literature: if the positioning of the specimen causes an increase of the superficial area subjected to the corrosive medium, there will be an increase of the mass loss. Looking at tables 4.11 and 4.12, it is observed that the mass change increases from (c) to (a), and then increases even more to (b). Furthermore, it was concluded that using the leaned position with the ACD boundary condition reduced the deviation of the results when compared to experimental results obtained by Salama et al. [1].

4.2.11 Electrolyte volume

The results of the electrolyte volume influence analysis are reported in table 4.13.

Table 4.13: Results with EEP boundary condition applied: -0.57 V.

Time (days)	Experimental	COMSOL					
		$Volume = 23556$ mm³		$Volume = 32490$ mm³		$Volume = 42786$ mm³	
	$\frac{\Delta m}{m0}$ (%)	$\frac{\Delta m}{m0}$ (%)	Deviation (%)	$\frac{\Delta m}{m0}$ (%)	Deviation (%)	$\frac{\Delta m}{m0}$ (%)	Deviation (%)
0	**0.000**	**0.000**	-	**0.000**	-	**0.000**	-
7	**0.091**	**0.092**	1.462	**0.091**	0.442	**0.091**	-0.362
14	**0.170**	**0.184**	8.112	**0.182**	7.025	**0.182**	6.940
21	**0.277**	**0.276**	-0.630	**0.273**	-1.629	**0.273**	-1.706
28	**0.357**	**0.367**	2.980	**0.364**	1.946	**0.363**	1.866
Average deviation (%)		-	2.221	-	1.194	-	1.114

Observing the results, it is possible to conclude that the changes made in the dimensions of the recipient had almost no influence in the results, changing the mass variation by no more than 0.005% and the average deviation only changed by approximately 1%.

As conclusion from the Sensitivity Analysis, in addition to the parameters concluded and shown on table 4.10, it was concluded that the best positioning of the bulk specimen was leaned on the recipient wall, as shown on figure 4.24.

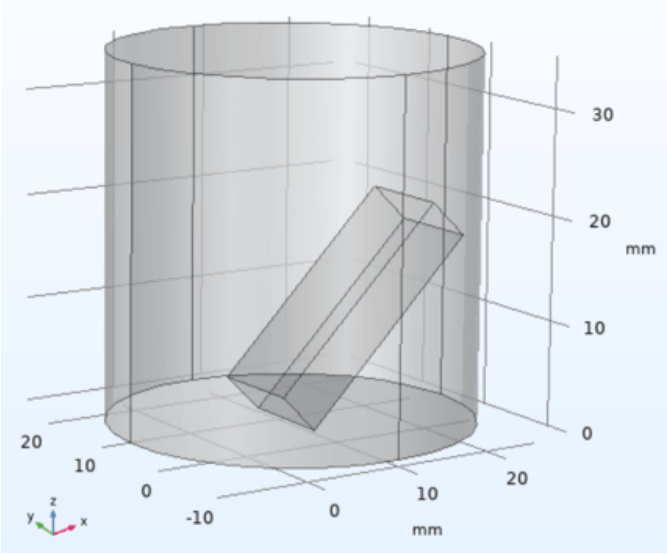

Figure 4.24: Best positioning to be used for the bulk specimen model.

Also, table 4.14 compares the experimental results from Salama et al. [1] with the values obtained with the leaned specimen, showing the best results obtained with the parameters from the sensitivity analysis, where one model uses ACD boundary condition and the other one uses EEP boundary condition.

Table 4.14: Results with EEP boundary condition applied: -0.57 V.

Time (days)	**Experimental**	$i_{average} = 0.0523$ A/m²		$\Phi_{s,ext} = -0.57$ V	
	$\frac{\Delta m}{m0}$ (%)	$\frac{\Delta m}{m0}$ (%)	Deviation (%)	$\frac{\Delta m}{m0}$ (%)	Deviation (%)
0	**0.000**	**0.000**	-	**0.000**	-
7	**0.091**	**0.081**	-10.454	**0.097**	7.029
14	**0.170**	**0.162**	-4.582	**0.194**	14.042
21	**0.277**	**0.243**	-12.295	**0.291**	4.819
28	**0.357**	**0.324**	-9.106	**0.388**	8.625

4.3 Porous Specimens

According to the described processes in Section 3.2.5 (or in figure 3.21), this section will be divided in three studies: Continuous Analysis of 28 days experiment, Phased Analysis of 28 days experiment, and Analysis of 42 days experiment. For simplification, table 4.15 presents a coding used in the next sections.

Table 4.15: Coding used for the three different simulations conditions.

Simulation	Denomination
Continuous Analysis of 28 days experiment	Condition A
Phased Analysis of 28 days experiment	Condition B
Analysis of 42 days experiment	Condition C

The three models for the different types of specimens are shown on figure 4.25.

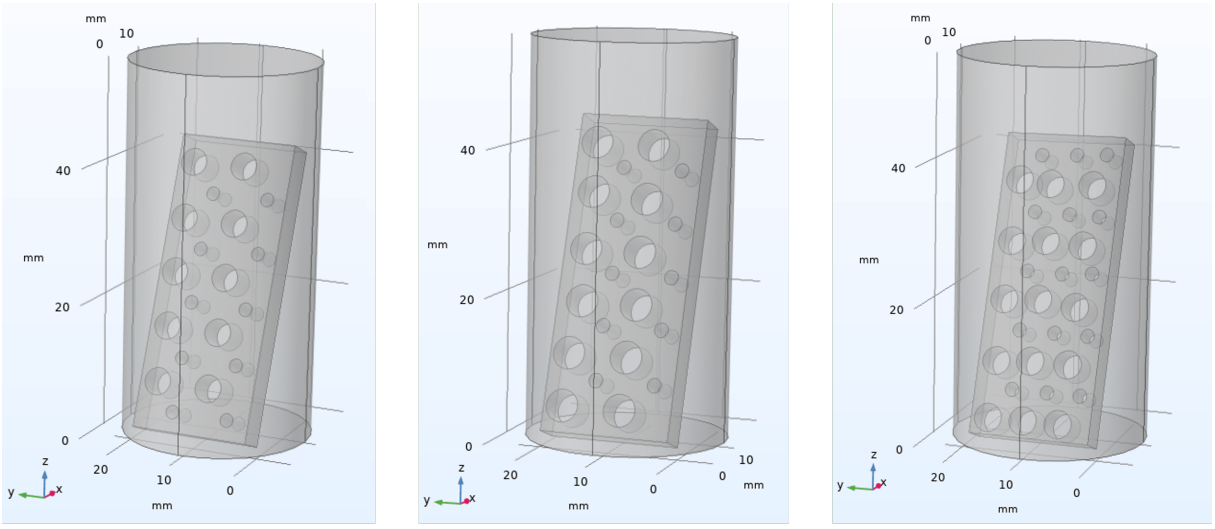

(a) (b) (c)

Figure 4.25: *COMSOL* models for the porous specimens (a) A4_2_20; (b) A4_2_23; (c) A4_2_30.

4.3.1 Condition A

The two types of boundary conditions analysed in this dissertation were implemented, at first, for the A4_2_20 specimens with the 28 days experiment, with a continuous analysis. The results are represented in table 4.16.

Table 4.16: Results of A4_2_20 specimen with EEP and ACD boundary condition.

Time (days)	Experimental	COMSOL							
		$\Phi_{s,ext} = -0.6$ V		$\Phi_{s,ext} = -0.57$ V		$i_{average} = 0.1153$ A/m²		$i_{average} = 0.0523$ A/m²	
	$\frac{\Delta m}{m0}$ (%)	$\frac{\Delta m}{m0}$ (%)	Deviation (%)	$\frac{\Delta m}{m0}$ (%)	Deviation (%)	$\frac{\Delta m}{m0}$ (%)	Deviation (%)	$\frac{\Delta m}{m0}$ (%)	Deviation (%)
0	**0.000**	**0.000**	-	**0.000**	-	**0.000**	-	**0.000**	-
7	**0.082**	**0.408**	397.705	**0.152**	84.876	**0.226**	175.369	**0.102**	24.925
14	**0.138**	**0.816**	489.788	**0.303**	119.175	**0.451**	226.458	**0.205**	48.123
21	**0.272**	**1.223**	350.009	**0.455**	67.302	**0.677**	149.196	**0.307**	13.083
28	**0.367**	**1.629**	343.416	**0.606**	64.922	**0.903**	145.651	**0.410**	11.490

Also, the results from the numerical simulations are shown on figure 4.26.

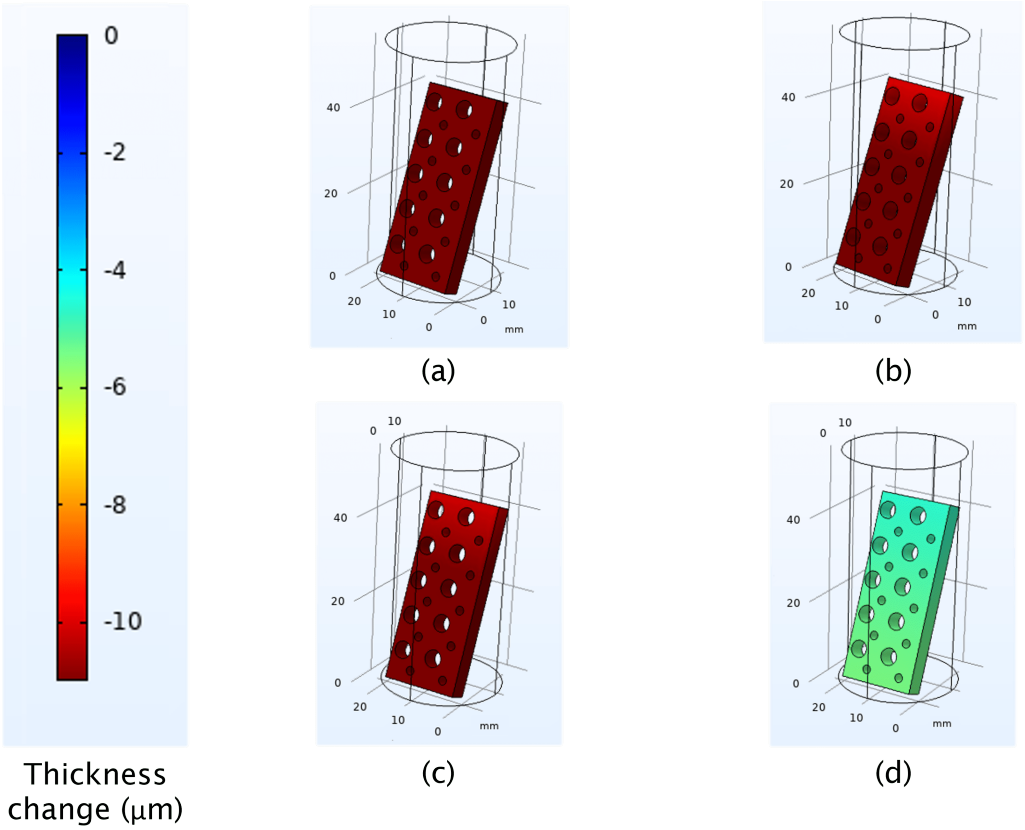

Figure 4.26: *COMSOL* results at 28th day for the specimen A4_2_20 (a) $\phi_{s,ext} = -0.6$ V; (b) $\phi_{s,ext} = -0.57$ V; (c) $i_{average} = 0.1153$ A/m²; (d) $i_{average} = 0.0523$ A/m².

As it is easily noticeable, the deviations in table 4.16 are all rather high, excluding the ones obtained with the ACD boundary condition with $i_{average} = 0.0523$ A/m² applied. Consequently, only this model will be used henceforth for the porous specimens. With this being stated, the results for the 28 days experiment with a continuous analysis for the A4_2_23 specimen are represented in table 4.17.

Table 4.17: Results of A4_2_23 specimen with ACD boundary condition: 0.0523 A/m^2.

Time (days)	Experimental	Numerical	
	$\frac{\Delta m}{m0}$ (%)	$\frac{\Delta m}{m0}$ (%)	Deviation (%)
0	**0.000**	**0.000**	-
7	**0.086**	**0.114**	32.752
14	**0.192**	**0.229**	19.496
21	**0.284**	**0.343**	20.763
28	**0.380**	**0.458**	20.409

Also, the results for the 28 days experiment with a continuous analysis for the A4_2_30 specimen are represented in table 4.17.

Table 4.18: Results of A4_2_30 specimen with ACD boundary condition: 0.0523 A/m^2.

Time (days)	Experimental	Numerical	
	$\frac{\Delta m}{m0}$ (%)	$\frac{\Delta m}{m0}$ (%)	Deviation (%)
0	**0.000**	**0.000**	-
7	**0.098**	**0.130**	32.687
14	**0.203**	**0.259**	27.957
21	**0.318**	**0.389**	22.117
28	**0.420**	**0.518**	23.421

Lastly, the results from the numerical simulations are shown on figure 4.27.

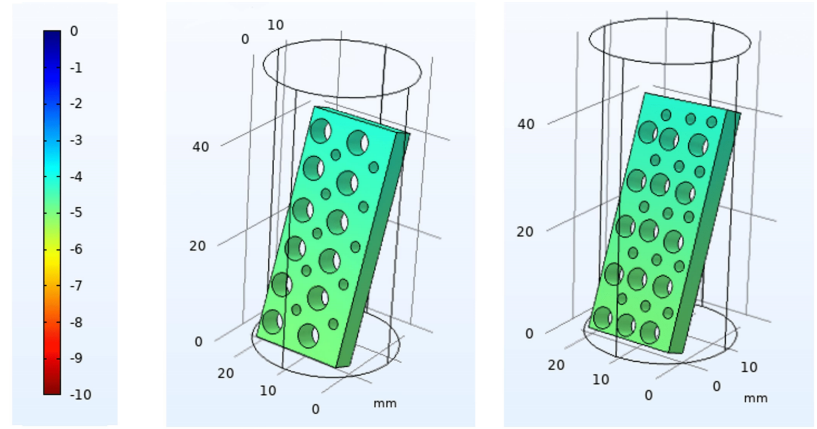

Figure 4.27: *COMSOL* results at 28th day (a) legend; (b) A4_2_23 specimen; (c) A4_2_30 specimen.

The deviations in the A4_2_20, A4_2_23 and A4_2_30 specimens are, respectively, 24.4%, 23.4% and 26.5%. So, it can be stated that with the increase in the porosity, the model loses its accuracy, as the deviations tend to increase with the increment in the porosity. This tendency of the increase of the deviation with the porosity could mean that, experimentally, there are some effects that somehow block the corrosion, and that are not verified in the numerical simulations. This could happen due to the

disregard of the variation in space and/or time of the electrolyte composition, or ionic strength. As a note, it is stated that this tendency could be even more noticeable if there was no break in the pattern of mass loss in the specimen A4_2_20 between the seventh and twenty-first days in the experimental results, increasing greatly the deviation in that time interval.

4.3.2 Condition B

To investigate if the phased analysis was more accurate than the continuous analysis, the table 4.19 has the results from both cases. The caption (A) and (B) is made according to the numeration of the processes done in Section 3.2.5. The first one is for the analysis of 28 days with continuous analysis, while the second one is for the phased analysis.

Table 4.19: A4_2_20 specimen: continuous analysis vs. phased analysis.

Time (days)	Experimental	(A)		(B)	
	$\frac{\Delta m}{m0}$ (%)	$\frac{\Delta m}{m0}$ (%)	Deviation (%)	$\frac{\Delta m}{m0}$ (%)	Deviation (%)
0	**0.000**	**0.000**	-	**0.000**	-
7	**0.082**	**0.102**	24.925	**0.102**	24.925
14	**0.138**	**0.205**	48.123	**0.204**	47.403
21	**0.271**	**0.307**	13.083	**0.305**	12.320
28	**0.367**	**0.410**	11.490	**0.406**	10.603

Also, the results of the phased analysis from *COMSOL* are shown on figure 4.28.

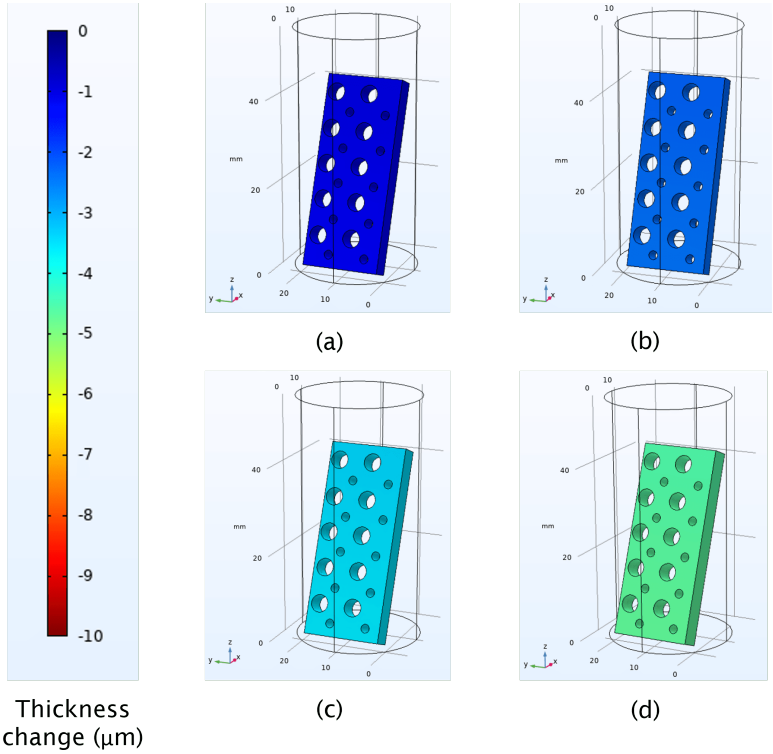

Figure 4.28: *COMSOL* results for the phased analysis (a) results at the 7th day; (b) results at the 14th day; (c) results at the 21th day; (d) results at the 28th day.

Comparing results of the table 4.19 and also with the figures 4.26 and 4.28, it was concluded that both types of analysis gave similar results, with a mass change variation of less than 0.01%. However, it should be noted that using the phased analysis has two downsides associated:

- The new geometry is generated from a simplification of the mesh, after the latter being exported from a previous analysis. This means that some simplifications are made, and the volume of the new mesh will not be the same as in the first one. So, when comparing results, only the changes in the volume, and not the volume itself, must be considered in the results.
- This process is much more time consuming than the continuous analysis and the results are almost the same, so it may not be worth it. Whereas for a continuous analysis it takes about 30 minutes from the moment the model starts to be created until the results are ready, for a phased analysis it takes around 75 minutes from the moment the first model is started until the results of the 28th day are obtained.

4.3.3 Condition C

The results for the 42 days analysis are reported in the table 4.20.

Table 4.20: Results of porous specimen for a 42 days analysis.

Time (days)	A4_2_20			A4_2_23			A4_2_30		
	Experimental	Numerical		Experimental	Numerical		Experimental	Numerical	
	$\frac{\Delta m}{m0}$ (%)	$\frac{\Delta m}{m0}$ (%)	Deviation (%)	$\frac{\Delta m}{m0}$ (%)	$\frac{\Delta m}{m0}$ (%)	Deviation (%)	$\frac{\Delta m}{m0}$ (%)	$\frac{\Delta m}{m0}$ (%)	Deviation (%)
0	**0.000**	**0.000**	-	**0.000**	**0.000**	-	**0.000**	**0.000**	-
42	**0.457**	**0.614**	34.412	**0.420**	**0.686**	63.370	**0.430**	**0.781**	81.625

Also, the *COMSOL* simulations results are shown on figure 4.29.

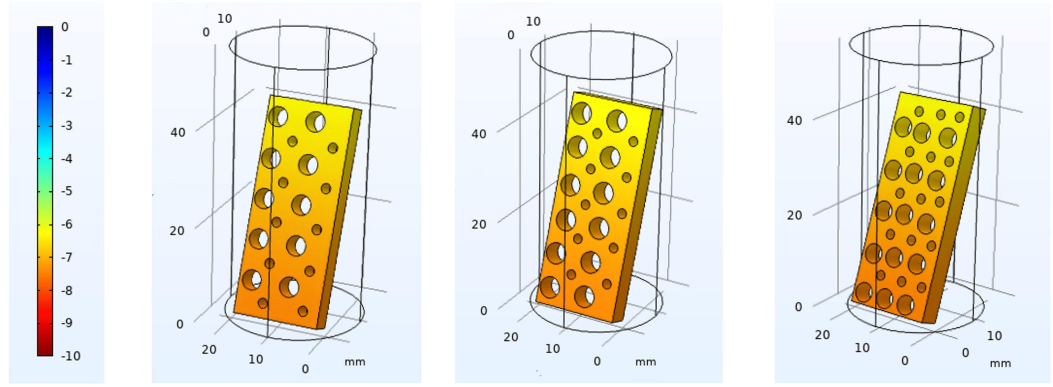

Figure 4.29: *COMSOL* results at 42th day (a) legend; (b) A4_2_20 specimen; (c) A4_2_23 specimen; (d) A4_2_30 specimen.

Analysing them, it is concluded that with the increase in the specimens porosity, the relative deviation also increased. A possible justification could be that *COMSOL* maintains ideal corrosion conditions when in reality this is not physically possible. On the other hand, comparing the experimental results of the

28 days analysis from tables 4.16, 4.17 and 4.18 to the results presented in this section, it is possible to conclude that the decrease in the mass change is small when compared to what might be expected. Whereas the 28 days analysis has, experimentally, approximately 0.1% of mass change every 7 days, the 42 days experimental results shown a mass change around 0.07% per week. This decrease in the corrosive response could be due to experimental imprecisions that the simulation does not have into account. For example, after the 42 days continuous corrosion there could have been some corrosion products that could not be separated from the specimen, or with long corrosion periods the accumulation of corrosion products in the specimen surface could slow down the corrosion process.

4.3.4 Parameters Confirmation

Lastly, more simulations were performed in order to confirm that the parameters concluded from the Sensitivity Analysis, in Section 4.2, were the appropriate ones to be used in high porosity specimens with long immersion times. Four different simulations were performed and their results were compared to the ones obtained in Section 4.3.3 for the A4_2_30 specimen: a) using the Mesh Quality Index (8), Extra fine; b) using ACD boundary condition with $i_{average}$ of 0.1153 A/m^2; c) using EEP boundary condition with $\phi_{s,ext}$ of -0.6 V; d) using EEP boundary condition with $\phi_{s,ext}$ of -0.57 V.

When using the Extra fine mesh instead of the Finer, the results obtained were the ones presented in table 4.21.

Table 4.21: Results of A4_2_30 specimen for a 42 days analysis with Finer and Extra Fine meshes.

Time (days)	**Experimental**	**Finer Mesh**			**Extra Fine Mesh**		
	$\frac{\Delta m}{m0}$ (%)	Simulation Time	$\frac{\Delta m}{m0}$ (%)	Deviation (%)	Simulation Time	$\frac{\Delta m}{m0}$ (%)	Deviation (%)
0	**0.000**	2h 17min 48s	**0.000**	-	93h 40min 39s	**0.000**	-
42	**0.430**		**0.781**	81.625		**0.790**	83.717

It was concluded that using a more refined mesh is not beneficial, as the simulation time increases exponentially and the difference in the mass change results is negligible.

When using the same boundary condition as in Table 4.20 but with a different value for $i_{average}$, or alternatively using the EEP boundary condition with the referred values for $\phi_{s,ext}$, and comparing the different results, the outcome obtained is as shown on table 4.22.

Table 4.22: Results of A4_2_30 specimen for a 42 days analysis with different boundary conditions applied.

Time (days)	**Experimental**	$i_{average} = 0.0523$ A/m^2		$i_{average} = 0.1153$ A/m^2		$\Phi_{s,ext} = -0.57$ V		$\Phi_{s,ext} = -0.6$ V	
	$\frac{\Delta m}{m0}$ (%)	$\frac{\Delta m}{m0}$ (%)	Deviation (%)	$\frac{\Delta m}{m0}$ (%)	Deviation (%)	$\frac{\Delta m}{m0}$ (%)	Deviation (%)	$\frac{\Delta m}{m0}$ (%)	Deviation (%)
0	**0.000**	**0.000**	-	**0.000**	-	**0.000**	-	**0.000**	-
42	**0.430**	**0.781**	81.625	**1.720**	300.093	**1.190**	176.184	**3.191**	642.140

From the results, it is possible to conclude that, as observed in the beginning of Section 4.3.1, using the ACD boundary condition with the $i_{average}$ value of 0.0523 A/m^2 for the specimen with higher level of porosity and with a long immersion period continues to be where the numerical results are closer to the experimental ones.

Chapter 5

Conclusions and Future Work

5.1 Conclusions

This dissertation intended to study the viability of predicting pure iron corrosion in a SBF medium with *COMSOL* FEA software. In order to accomplish this, the models developed results were compared with experimental results obtained in Salama et al. [1], being used to calibrate and validate the models developed. Also, pure iron was characterized mechanically so this properties would be included in the *COMSOL* models.

Tensile and compression iron specimens were designed and machined for the mechanical characterization. The force-displacement and true stress-true strain curves were obtained after analysing the data. Also, the loading paths of the tensile and compression tests were plotted in principal strain space, and the slope of the strain paths followed the expected behaviour.

The second part of this dissertation coupled the numerical simulations results of corrosion of the various iron specimens in *COMSOL* software with the previous experimental work performed by Salama et al. [1]. A sensitivity analysis was effectively performed, using the simpler bulk iron specimen, in order to calibrate and validate the model for the real conditions in Salama et al. [1]. In this process, it was concluded that: 1) there were some conditions or parameters that highly influenced the numerical results, being these the mesh refinement, the specimen positioning, the polarization curve used and the boundary condition applied; 2) other parameters or conditions had minor influences, specifically the electrolyte electrical conductivity, some variations in the temperature, the electrolyte volume and the input of the mechanical properties; 3) four different calibrated models could be used to simulate with great accuracy the results of the Fe immersion tests in SBF. Those four models created were considered in the porous specimens analysis. The models had two different types of boundary conditions applied, imposing in the electrode (iron bulk specimen) surface, either a potential or a current density.

On the porous specimens numerical models, running firstly the simulations for the A4_2_20 specimen in a continuous analysis of 28 days experiment, it was concluded that only one of the four models considered after the sensitivity analysis would be used for the porous specimens simulations.

The model chosen to be used was the one that had the boundary condition imposing a current density

of 0.0523 A/m^2 on the electrode surface, with an average deviation of approximately 24% from the experimental results.

It was observed that the average deviation of the numerical results when compared to the experimental ones had a tendency to be higher with the porosity increase of the iron specimens. This effect could be explained by some experimental limitations that somehow delayed the corrosion processes and do not exist in the numerical model, such as the disregard of the variation in space and time of the electrolyte composition or the ionic strength, no variation in electrolyte composition, no variation on the pH of the solution, or the non-accumulation of corrosion products in the electrode surface. Then, a phased analysis of 28 days experiment was performed, where four different analysis were undertaken, for which the final result of the first set was exported to run the second analysis, and so on (more similar to the experimental process). The conclusion was that the results were very similar while still had the disadvantage of taking much longer to obtain the final value. The similarity of the results means that the *COMSOL* models used did not have into account the aforementioned effects of loss of some electrolyte properties over time that were observed in experimental tests, and so using a phased analysis would be unnecessary. Lastly, with the analysis of 42 days experiment, the deviations were even higher than those previously obtained. These larger differences should be addressed to all the effects that happen experimentally and the models created disregard. Also, due to the 42 days corrosion, the cleaning of the specimen is more difficult, and it is more possible that some corrosion products stay attached to the iron specimens, altering the mass change measurements. Lastly, with the simulation data gathered in this work it was concluded that numerical models can be used to simulate corrosion phenomena faster and substitute the experimental studies that take much longer and are much more costly.

5.2 Future Work

Concerning the scope of the present dissertation, some numerical model simplifications were made, imposing some constraints that affected the results. The models used, assuming a secondary current distribution in the domain, disregards some physical aspects that turn the model close to ideal and, consequently, very different from the experimental conditions. Having this in mind, a model with chemical species transport associated with the secondary current distribution could be developed to have the mass transport and the concentration overpotential in consideration, or a model with tertiary current distribution where the electrolyte composition or ionic strength vary in space and time. These more complex models would allow to obtain results on the porous iron specimens more similar to the experimental ones, using new parameters concluded from a novel sensitivity analysis.

Also, it would be very important to make an electrochemical analysis of the electrolyte-electrode interface like explained in Section 2.3.3, with the SBF obtained in IPS and the iron acquired from *Goodfellow Inc.*, obtain the polarization curve from it and perform the Tafel analysis. This would improve the accuracy of the sensitivity analysis and, probably, lead to better results in the porous specimens. Also, it could be interesting to measure the electrolyte conductivity, as it makes no

difference on a model created with secondary current distribution, but could do on a model with tertiary current condition, for example. Moreover, the external electric potential applied on the electrode surface should be experimentally measured in order to be used as input on the numerical model, as it was observed that this parameter highly influences the numerical results. Additionally, longer immersion tests and with more varied time intervals should be performed in order to accomplish more data so the numerical model could be better calibrated, as it was in long term simulations that the numerical and experimental results presented greatest differences between them.

Lastly, it was noticed that *COMSOL* had the tools needed to perform a very important set of analysis in order to study the behavior of bone implants. By first doing a corrosion analysis on a bone implant prototype, the mesh after the corrosion period (as an example, 28 days) could be exported and then inserted in a new model, were a structural, linear analysis would be performed. This would allow to study the mechanical properties before and after the corrosion process on *COMSOL*, so that it would be possible to predict the structural changes that the corrosion had caused on the implant. For this, the mechanical characterization of iron should be performed again, since the results were not satisfactory mainly in the tensile specimens. Calibrating all this process with experimental results, *COMSOL* would be the perfect tool to help on the design of bone implants, allowing fast and smart iterations.

References

[1] M. C. Salama, D. Rechena, L. Reis, A. M. Deus, C. Santos, M. J. Carmezim, and M. F. Vaz. Effect of the topology on the mechanical properties of porous iron immersed in body fluids. *Proceedings of the Institution of Mechanical Engineers, Part L: Journal of Materials: Design and Applications*, 235(5):1066–1076, jan 2021. ISSN 1464-4207. doi: 10.1177/1464420720987860. URL http://journals.sagepub.com/doi/10.1177/1464420720987860.

[2] W. Andrew. Human skeleton, *Encyclopedia Britannica*. URL https://www.britannica.com/science/human-skeleton. Accessed 12 July 2021.

[3] Word Health Organization. Falls. URL https://www.who.int/news-room/fact-sheets/detail/falls. Accessed 24 Jul 2021.

[4] N. M. Haines, W. D. Lack, R. B. Seymour, and M. J. Bosse. Defining the Lower Limit of a "Critical Bone Defect" in Open Diaphyseal Tibial Fractures. *Journal of Orthopaedic Trauma*, 30(5):e158–e163, may 2016. ISSN 0890-5339. doi: 10.1097/BOT.0000000000000531. URL https://journals.lww.com/00005131-201605000-00015.

[5] S. Bose, S. Vahabzadeh, and A. Bandyopadhyay. Bone tissue engineering using 3D printing. *Materials Today*, 16(12):496–504, dec 2013. ISSN 13697021. doi: 10.1016/j.mattod.2013.11.017. URL http://dx.doi.org/10.1016/j.mattod.2013.11.017.

[6] E. H. Schemitsch. Size Matters: Defining Critical in Bone Defect Size! *Journal of Orthopaedic Trauma*, 31:S20–S22, oct 2017. ISSN 0890-5339. doi: 10.1097/BOT.0000000000000978. URL https://journals.lww.com/00005131-201710005-00005.

[7] M. Wooten, H. Weng, T. V. Hartke, J. Borzan, A. H. Klein, B. Turnquist, X. Dong, R. A. Meyer, and M. Ringkamp. Three functionally distinct classes of C-fibre nociceptors in primates. *Nature Communications*, 5:4122, jun 2014. ISSN 2041-1723. doi: 10.1038/ncomms5122. URL http://www.nature.com/articles/ncomms5122.

[8] C. Mauffrey, B. T. Barlow, and W. Smith. Management of Segmental Bone Defects. *Journal of the American Academy of Orthopaedic Surgeons*, 23(3):143–153, mar 2015. ISSN 1067-151X. doi: 10.5435/JAAOS-D-14-00018. URL http://www.jaaos.org/cgi/doi/10.5435/JAAOS-D-14-00018.

[9] A. Prasad. State of art review on bioabsorbable polymeric scaffolds for bone tissue engineering. *Materials Today: Proceedings*, 44:1391–1400, 2021. ISSN 2214-7853. doi: 10.1016/j.matpr.2020.11.622. URL https://www.sciencedirect.com/science/article/pii/S2214785320392968.

[10] J. E. Dumas, E. M. Prieto, K. J. Zienkiewicz, T. Guda, J. C. Wenke, J. Bible, G. E. Holt, and S. A. Guelcher. Balancing the rates of new bone formation and polymer degradation enhances healing of weight-bearing allograft/polyurethane composites in rabbit femoral defects. *Tissue Engineering - Part A*, 20(1-2):115–129, out 2014. ISSN 1937335X. doi: 10.1089/ten.tea.2012.0762. URL https://www.liebertpub.com/doi/10.1089/ten.tea.2012.0762.

[11] H. Hermawan. Updates on the research and development of absorbable metals for biomedical applications. *Progress in Biomaterials*, 7:93–110, may 2018. ISSN 2194-0509. doi: 10.1007/s40204-018-0091-4. URL https://doi.org/10.1007/s40204-018-0091-4.

[12] Q. Xu and J. T. Czernuszka. Controlled release of amoxicillin from hydroxyapatite-coated poly(lactic-co-glycolic acid) microspheres. *Journal of Controlled Release*, 127(2):146–153, apr 2008. ISSN 01683659. doi: 10.1016/j.jconrel.2008.01.017. URL https://linkinghub.elsevier.com/retrieve/pii/S0168365908000722.

[13] X. Wang, S. Xu, S. Zhou, W. Xu, M. Leary, P. Choong, M. Qian, M. Brandt, and Y. M. Xie. Topological design and additive manufacturing of porous metals for bone scaffolds and orthopaedic implants: A review. *Biomaterials*, 83:127–141, mar 2016. ISSN 01429612. doi: 10.1016/j.biomaterials.2016.01.012. URL https://linkinghub.elsevier.com/retrieve/pii/S0142961216000144.

[14] A. R. Amini, C. T. Laurencin, and S. P. Nukavarapu. Bone tissue engineering: Recent advances and challenges. *Critical Reviews in Biomedical Engineering*, 40(5):363–408, jan 2012. ISSN 0278940X. doi: 10.1615/CritRevBiomedEng.v40.i5.10. URL https://pubmed.ncbi.nlm.nih.gov/23339648/.

[15] L. Li, F. Yu, J. Shi, S. Shen, H. Teng, J. Yang, X. Wang, and Q. Jiang. In situ repair of bone and cartilage defects using 3D scanning and 3D printing. *Scientific Reports*, 7,9416:1–12, aug 2017. ISSN 20452322. doi: 10.1038/s41598-017-10060-3. URL http://dx.doi.org/10.1038/s41598-017-10060-3.

[16] D. R. Sumner. Long-term implant fixation and stress-shielding in total hip replacement. *Journal of Biomechanics*, 48(5):797–800, mar 2015. ISSN 18732380. doi: 10.1016/j.jbiomech.2014.12.021. URL http://dx.doi.org/10.1016/j.jbiomech.2014.12.021.

[17] N. S. Moghaddam, M. T. Andani, A. Amerinatanzi, C. Haberland, S. Huff, M. Miller, M. Elahinia, and D. Dean. Metals for bone implants: safety, design, and efficacy. *Biomanufacturing Reviews*, 1:1, oct 2016. ISSN 2363-507X. doi: 10.1007/s40898-016-0001-2. URL http://link.springer.com/10.1007/s40898-016-0001-2.

[18] G. Li, L. Wang, W. Pan, F. Yang, W. Jiang, X. Wu, X. Kong, K. Dai, and Y. Hao. In vitro and in vivo study of additive manufactured porous Ti6Al4V scaffolds for repairing bone defects. *Scientific Reports*, 6,34072:1–11, sep 2016. ISSN 20452322. doi: 10.1038/srep34072. URL http://dx.doi.org/10.1038/srep34072.

[19] Z. Sheikh, S. Najeeb, Z. Khurshid, V. Verma, H. Rashid, and M. Glogauer. Biodegradable Materials for Bone Repair and Tissue Engineering Applications. *Materials*, 8(9):5744–5794, aug 2015. ISSN 1996-1944. doi: 10.3390/ma8095273. URL http://www.mdpi.com/1996-1944/8/9/5273.

[20] G. L. Koons, M. Diba, and A. G. Mikos. Materials design for bone-tissue engineering. *Nature Reviews Materials*, 5(8):584–603, aug 2020. ISSN 20588437. doi: 10.1038/s41578-020-0204-2. URL http://dx.doi.org/10.1038/s41578-020-0204-2.

[21] L. Polo-Corrales, M. Latorre-Esteves, and J. E. Ramirez-Vick. Scaffold design for bone regeneration. *Journal of Nanoscience and Nanotechnology*, 14(1):15–56, jan 2014. ISSN 15334880. doi: 10.1166/jnn.2014.9127. URL https://pubmed.ncbi.nlm.nih.gov/24730250/.

[22] J. He, J. Fang, P. Wei, Y. Li, H. Guo, Q. Mei, and F. Ren. Cancellous bone-like porous Fe@Zn scaffolds with core-shell-structured skeletons for biodegradable bone implants. *Acta Biomaterialia*, 121:665–681, feb 2021. ISSN 18787568. doi: 10.1016/j.actbio.2020.11.032. URL https://pubmed.ncbi.nlm.nih.gov/33242640/.

[23] S. Wang, Y. Xu, J. Zhou, H. Li, J. Chang, and Z. Huan. In vitro degradation and surface bioactivity of iron-matrix composites containing silicate-based bioceramic. *Bioactive Materials*, 2(1):10–18, mar 2017. ISSN 2452199X. doi: 10.1016/j.bioactmat.2016.12.001. URL http://dx.doi.org/10.1016/j.bioactmat.2016.12.001.

[24] G. Hannink and J. J.Chris Arts. Bioresorbability, porosity and mechanical strength of bone substitutes: What is optimal for bone regeneration? *Injury*, 42(SUPPL. 2):S22–S25, sep 2011. ISSN 00201383. doi: 10.1016/j.injury.2011.06.008. URL http://dx.doi.org/10.1016/j.injury.2011.06.008.

[25] E. García-Gareta, M. J. Coathup, and G. W. Blunn. Osteoinduction of bone grafting materials for bone repair and regeneration. *Bone*, 81:112–121, dec 2015. ISSN 87563282. doi: 10.1016/j.bone.2015.07.007. URL http://dx.doi.org/10.1016/j.bone.2015.07.007.

[26] L. Yuan, S. Ding, and C. Wen. Additive manufacturing technology for porous metal implant applications and triple minimal surface structures: A review. *Bioactive Materials*, 4:56–70, dec 2019. ISSN 2452199X. doi: 10.1016/j.bioactmat.2018.12.003. URL https://doi.org/10.1016/j.bioactmat.2018.12.003.

[27] L. Roseti, V. Parisi, M. Petretta, C. Cavallo, G. Desando, I. Bartolotti, and B. Grigolo. Scaffolds for Bone Tissue Engineering: State of the art and new perspectives. *Materials Science and Engineering C*, 78:1246–1262, sep 2017. ISSN 09284931. doi: 10.1016/j.msec.2017.05.017. URL http://dx.doi.org/10.1016/j.msec.2017.05.017.

[28] D. F. Williams. On the mechanisms of biocompatibility. *Biomaterials*, 29(20):2941–2953, jul 2008. ISSN 01429612. doi: 10.1016/j.biomaterials.2008.04.023. URL https://doi.org/10.1016/j.biomaterials.2008.04.023.

[29] G. Bouet, D. Marchat, M. Cruel, L. Malaval, and L. Vico. In Vitro Three-Dimensional Bone Tissue Models: From Cells to Controlled and Dynamic Environment. *Tissue Engineering Part B: Reviews*, 21:133–156, feb 2015. ISSN 1937-3368. doi: 10.1089/ten.teb.2013.0682. URL https://doi.org/10.1089/ten.teb.2013.0682.

[30] J. Henkel, M. A. Woodruff, D. R. Epari, R. Steck, V. Glatt, I. C. Dickinson, P. F. M. Choong, M. A. Schuetz, and D. W. Hutmacher. Bone Regeneration Based on Tissue Engineering Conceptions — A 21st Century Perspective. *Bone Research*, 3:216–248, dec 2013. ISSN 2095-4700. doi: 10.4248/BR201303002. URL https://doi.org/10.4248/BR201303002.

[31] S. G. Kumbar, C. T. Laurencin, and M. Deng. *Natural and Synthetic Biomedical Polymers*. Elsevier Science, 1st edition, 2014. ISBN 978-0-12-396983-5. URL https://doi.org/10.1016/C2011-0-07330-1.

[32] Y. F. Zheng, X. N. Gu, and F. Witte. Biodegradable metals. *Materials Science and Engineering: R: Reports*, 77:1–34, mar 2014. ISSN 0927796X. doi: 10.1016/j.mser.2014.01.001. URL https://doi.org/10.1016/j.mser.2014.01.001.

[33] F. J. O'Brien. Biomaterials scaffolds for tissue engineering. *Materials Today*, 14(3):88–95, mar 2011. ISSN 13697021. doi: 10.1016/S1369-7021(11)70058-X. URL http://dx.doi.org/10.1016/S1369-7021(11)70058-X.

[34] B. P. Chan and K. W. Leong. Scaffolding in tissue engineering: general approaches and tissue-specific considerations. *European Spine Journal*, 17(Suppl 4):S467–S479, dec 2008. ISSN 0940-6719. doi: 10.1007/s00586-008-0745-3. URL https://doi.org/10.1007/s00586-008-0745-3.

[35] D. W. Hutmacher. Scaffolds in tissue engineering bone and cartilage. *Biomaterials*, 21(24):2529–2543, dec 2000. doi: 10.1016/s0142-9612(00)00121-6. URL https://doi.org/10.1016/S0142-9612(00)00121-6.

[36] S. Yang, J. Wang, L. Tang, H. Ao, H. Tan, T. Tang, and C. Liu. Mesoporous bioactive glass doped-poly (3-hydroxybutyrate-co-3-hydroxyhexanoate) composite scaffolds with 3-dimensionally hierarchical pore networks for bone regeneration. *Colloids and Surfaces B: Biointerfaces*, 116:72–80, apr 2014. ISSN 09277765. doi: 10.1016/j.colsurfb.2013.12.052. URL http://dx.doi.org/10.1016/j.colsurfb.2013.12.052.

[37] E. H. Backes, Emanuel M. F., G. S. Diogo, C. F. Marques, T. H. Silva, L. C. Costa, F. R. Passador, R. L. Reis, and L. A. Pessan. Engineering 3D printed bioactive composite scaffolds based on the combination of aliphatic polyester and calcium phosphates for bone tissue regeneration. *Materials Science and Engineering C*, 122:111928, mar 2021. ISSN 18730191. doi: 10.1016/j.msec.2021.111928. URL https://doi.org/10.1016/j.msec.2021.111928.

[38] ASTM F3160-21. Standard Guide for Metallurgical Characterization of Absorbable Metallic Materials for Medical Implants. Technical report, ASTM International, West Conshohocken, PA, January 2021. URL http://www.astm.org/cgi-bin/resolver.cgi?F3160.

[39] M. Geetha, A. K. Singh, R. Asokamani, and A. K. Gogia. Ti based biomaterials, the ultimate choice for orthopaedic implants - A review. *Progress in Materials Science*, 54(3):397–425, may 2009. ISSN 00796425. doi: 10.1016/j.pmatsci.2008.06.004. URL http://dx.doi.org/10.1016/j.pmatsci.2008.06.004.

[40] M. Long and H.J Rack. Titanium alloys in total joint replacement—a materials science perspective. *Biomaterials*, 19(18):1621–1639, sep 1998. ISSN 01429612. doi: 10.1016/S0142-9612(97)00146-4. URL https://doi.org/10.1016/S0142-9612(97)00146-4.

[41] ScienceDirect Topics. Stress Shielding - an overview, . URL https://www.sciencedirect.com/topics/veterinary-science-and-veterinary-medicine/stress-shielding. Accessed 24 Jul 2021.

[42] MyBiosource, Inc. Bone resorption. URL https://www.mybiosource.com/learn/conditions/bone-resorption/. Accessed 24 Jul 2021.

[43] ScienceDirect Topics. Cortical Bone - an overview, . URL https://www.sciencedirect.com/topics/medicine-and-dentistry/cortical-bone. Accessed 24 Jul 2021.

[44] E. N. Marieb and K. Hoehn. *Human Anatomy Physiology*. Pearson, United Kingdom, 11th edition, 2019.

[45] L J Gibson and M F Ashby. *Cellular solids*, volume 22. Camrbidge University Press, Cambridge, 2nd edition, 1999. ISBN 0521499119. doi: 10.1016/0021-9290(89)90056-0. URL https://linkinghub.elsevier.com/retrieve/pii/0021929089900560.

[46] Y. Okazaki and E. Gotoh. Comparison of metal release from various metallic biomaterials in vitro. *Biomaterials*, 26(1):11–21, jan 2005. ISSN 01429612. doi: 10.1016/j.biomaterials.2004.02.005. URL https://doi.org/10.1016/j.biomaterials.2004.02.005.

[47] H. Ibrahim, S. N. Esfahani, B. Poorganji, D. Dean, and M. Elahinia. Resorbable bone fixation alloys, forming, and post-fabrication treatments. *Materials Science and Engineering C*, 70:870–888, jan 2017. ISSN 09284931. doi: 10.1016/j.msec.2016.09.069. URL http://dx.doi.org/10.1016/j.msec.2016.09.069.

[48] W. Maret. The metals in the biological periodic system of the elements: Concepts and conjectures. *International Journal of Molecular Sciences*, 17,66:1–8, jan 2016. ISSN 14220067. doi: 10.3390/ijms17010066. URL https://pubmed.ncbi.nlm.nih.gov/26742035/.

[49] P. K. Bowen, J. Drelich, and J. Goldman. Zinc exhibits ideal physiological corrosion behavior for bioabsorbable stents. *Advanced Materials*, 25(18):2577–2582, may 2013. ISSN 09359648. doi: 10.1002/adma.201300226. URL https://pubmed.ncbi.nlm.nih.gov/23495090/.

[50] J. Venezuela and M. S. Dargusch. The influence of alloying and fabrication techniques on the mechanical properties, biodegradability and biocompatibility of zinc: A comprehensive review. *Acta Biomaterialia*, 87:1–40, mar 2019. ISSN 18787568. doi: 10.1016/j.actbio.2019.01.035. URL https://doi.org/10.1016/j.actbio.2019.01.035.

[51] M. P. Staiger, A. M. Pietak, J. Huadmai, and G. Dias. Magnesium and its alloys as orthopedic biomaterials: A review. *Biomaterials*, 27(9):1728–1734, mar 2006. ISSN 01429612. doi: 10.1016/j.biomaterials.2005.10.003. URL https://doi.org/10.1016/j.biomaterials.2005.10.003.

[52] F. Witte, V. Kaese, H. Haferkamp, E. Switzer, A. Meyer-Lindenberg, C. J. Wirth, and H. Windhagen. In vivo corrosion of four magnesium alloys and the associated bone response. *Biomaterials*, 26 (17):3557–3563, jun 2005. ISSN 01429612. doi: 10.1016/j.biomaterials.2004.09.049. URL https://doi.org/10.1016/j.biomaterials.2004.09.049.

[53] D. Carluccio, C. Xu, J. Venezuela, Y. Cao, D. Kent, M. Bermingham, A. G. Demir, B. Previtali, Q. Ye, and M. Dargusch. Additively manufactured iron-manganese for biodegradable porous load-bearing bone scaffold applications. *Acta Biomaterialia*, 103:346–360, feb 2020. ISSN 18787568. doi: 10.1016/j.actbio.2019.12.018. URL https://www.sciencedirect.com/science/article/pii/S1742706119308475?via%3Dihub.

[54] B. Zberg, P. J. Uggowitzer, and J. F. Löffler. MgZnCa glasses without clinically observable hydrogen evolution for biodegradable implants. *Nature Materials*, 8(11):887–891, nov 2009. ISSN 14764660. doi: 10.1038/nmat2542. URL http://dx.doi.org/10.1038/nmat2542.

[55] E. Balogh, G. Paragh, and V. Jeney. Influence of iron on bone homeostasis. *Pharmaceuticals*, 11 (4):107, oct 2018. ISSN 14248247. doi: 10.3390/ph11040107. URL https://pubmed.ncbi.nlm.nih.gov/30340370/.

[56] B. Liu and Y. F. Zheng. Effects of alloying elements (Mn, Co, Al, W, Sn, B, C and S) on biodegradability and in vitro biocompatibility of pure iron. *Acta Biomaterialia*, 7(3):1407–1420, mar 2011. ISSN 17427061. doi: 10.1016/j.actbio.2010.11.001. URL http://dx.doi.org/10.1016/j.actbio.2010.11.001.

[57] J. Čapek, J. Kubásek, D. Vojtěch, E. Jablonská, J. Lipov, and T. Ruml. Microstructural, mechanical, corrosion and cytotoxicity characterization of the hot forged FeMn30(wt.%) alloy. *Materials Science and Engineering C*, 58:900–908, jan 2016. ISSN 09284931. doi: 10.1016/j.msec.2015.09.049. URL https://doi.org/10.1016/j.msec.2015.09.049.

[58] T. Kraus, F. Moszner, S. Fischerauer, M. Fiedler, E. Martinelli, J. Eichler, F. Witte, E. Willbold, M. Schinhammer, M. Meischel, P. J. Uggowitzer, J. F. Löffler, and A. Weinberg. Biodegradable Fe-based alloys for use in osteosynthesis: Outcome of an in vivo study after 52 weeks. *Acta Biomaterialia*, 10(7):3346–3353, jul 2014. ISSN 18787568. doi: 10.1016/j.actbio.2014.04.007. URL http://dx.doi.org/10.1016/j.actbio.2014.04.007.

[59] A. Drynda, T. Hassel, F. W. Bach, and M. Peuster. In vitro and in vivo corrosion properties of new iron-manganese alloys designed for cardiovascular applications. *Journal of Biomedical Materials Research - Part B Applied Biomaterials*, 103(3):649–660, apr 2015. ISSN 15524981. doi: 10.1002/jbm.b.33234. URL https://doi.org/10.1002/jbm.b.33234.

[60] M. Parelman, B. Stoecker, A. Baker, and D. Medeiros. Iron restriction negatively affects bone in female rats and mineralization of hFOB osteoblast cells. *Experimental Biology and Medicine*, 231(4):378–386, apr 2006. ISSN 15353699. doi: 10.1177/153537020623100403. URL https://pubmed.ncbi.nlm.nih.gov/16565433/.

[61] J. G. Messer, P. T. Cooney, and D. E. Kipp. Iron chelator deferoxamine alters iron-regulatory genes and proteins and suppresses osteoblast phenotype in fetal rat calvaria cells. *Bone*, 46(5):1408–1415, may 2010. ISSN 87563282. doi: 10.1016/j.bone.2010.01.376. URL http://dx.doi.org/10.1016/j.bone.2010.01.376.

[62] D. Praticò, M. Pasin, O. P. Barry, A. Ghiselli, G. Sabatino, L. Iuliano, G. A. FitzGerald, and F. Violi. Iron-Dependent Human Platelet Activation and Hydroxyl Radical Formation. *Circulation*, 99(24):3118–3124, jun 1999. ISSN 0009-7322. doi: 10.1161/01.CIR.99.24.3118. URL https://doi.org/10.1161/01.CIR.99.24.3118.

[63] H. Hermawan, D. Dubé, and D. Mantovani. Developments in metallic biodegradable stents. *Acta Biomaterialia*, 6(5):1693–1697, may 2010. ISSN 17427061. doi: 10.1016/j.actbio.2009.10.006. URL http://dx.doi.org/10.1016/j.actbio.2009.10.006.

[64] MatWeb. Iron mechanical properties, . URL http://www.matweb.com/search/DataSheet.aspx?MatGUID=654ca9c358264b5392d43315d8535b7d. Accessed 27 Jul 2021.

[65] MatWeb. Magnesium mechanical properties, . URL http://www.matweb.com/search/DataSheet.aspx?MatGUID=ff6d4e6d529e4b3d97c77d6538b29693. Accessed 27 Jul 2021.

[66] AZoM. Zinc mechanical properties. URL https://www.azom.com/article.aspx?ArticleID=9122. Accessed 27 Jul 2021.

[67] A. Atala, F. Kurtis Kasper, and A. G. Mikos. Engineering complex tissues. *Science Translational Medicine*, 4(160):160rv12, nov 2012. ISSN 19466234. doi: 10.1126/scitranslmed.3004890. URL https://pubmed.ncbi.nlm.nih.gov/23152327/.

[68] E. A. Abou Neel, W. Chrzanowski, V. M. Salih, H. W. Kim, and J. C. Knowles. Tissue engineering in dentistry. *Journal of Dentistry*, 42(8):915–928, aug 2014. ISSN 03005712. doi: 10.1016/j.jdent.2014.05.008. URL http://dx.doi.org/10.1016/j.jdent.2014.05.008.

[69] Y. Chen, W. Zhang, M. F. Maitz, M. Chen, H. Zhang, J. Mao, Y. Zhao, N. Huang, and G. Wan. Comparative corrosion behavior of Zn with Fe and Mg in the course of immersion degradation in phosphate buffered saline. *Corrosion Science*, 111:541–555, oct 2016. ISSN 0010938X. doi: 10.1016/j.corsci.2016.05.039. URL http://dx.doi.org/10.1016/j.corsci.2016.05.039.

[70] M. Schinhammer, A. C. Hänzi, J. F. Löffler, and P. J. Uggowitzer. Design strategy for biodegradable Fe-based alloys for medical applications. *Acta Biomaterialia*, 6(5):1705–1713, may 2010. ISSN 17427061. doi: 10.1016/j.actbio.2009.07.039. URL http://dx.doi.org/10.1016/j.actbio.2009.07.039.

[71] J. Čapek, Š. Msallamová, E. Jablonská, J. Lipov, and D. Vojtěch. A novel high-strength and highly corrosive biodegradable Fe-Pd alloy: Structural, mechanical and in vitro corrosion and cytotoxicity study. *Materials Science and Engineering C*, 79:550–562, oct 2017. ISSN 09284931. doi: 10.1016/j.msec.2017.05.100. URL https://pubmed.ncbi.nlm.nih.gov/28629053/.

[72] ScienceDirect Topics. Spark Plasma Sintering - an overview, . URL https://www.sciencedirect.com/topics/materials-science/spark-plasma-sintering. Accessed 26 Jul 2021.

[73] Ioku, K. Transparent apatite ceramics prepared from apatite fine crystals synthesized hydrothermally. URL https://www.researchgate.net/publication/269194952_TRANSPARENT_APATITE_CERAMICS_PREPARED_FROM_APATITE_FINE_CRYSTALS_SYNTHESIZED_HYDROTHERMALLY. Accessed 26 Jul 2021.

[74] Mohammed Menhal Shbeh and Russell Goodall. Open Celled Porous Titanium. *Advanced Engineering Materials*, 19(11):1600664, nov 2017. ISSN 14381656. doi: 10.1002/adem.201600664. URL https://doi.org/10.1002/adem.201600664.

[75] K. G. Ozdemir, H. Yılmaz, and S. Yılmaz. In vitro evaluation of cytotoxicity of soft lining materials on L929 cells by MTT assay. *Journal of Biomedical Materials Research Part B: Applied Biomaterials*, 90B(1):82–86, nov 2008. ISSN 15524973. doi: 10.1002/jbm.b.31256. URL https://doi.org/10.1002/jbm.b.31256.

[76] ISO10993-5:2009. Biological evaluation of medical devices — Part 5: Tests for in vitro cytotoxicity. Technical report, ISO, Geneva, Switzerland, June 2009. URL https://www.iso.org/standard/36406.html.

[77] H. Hermawan, A. Purnama, D. Dube, J. Couet, and D. Mantovani. Fe-Mn alloys for metallic biodegradable stents: Degradation and cell viability studies. *Acta Biomaterialia*, 6(5):1852–1860, may 2010. ISSN 17427061. doi: 10.1016/j.actbio.2009.11.025. URL http://dx.doi.org/10.1016/j.actbio.2009.11.025.

[78] P. Sharma and P. M. Pandey. Corrosion behaviour of the porous iron scaffold in simulated body fluid for biodegradable implant application. *Materials Science and Engineering C*, 99:838–852, jun 2019. ISSN 18730191. doi: 10.1016/j.msec.2019.01.114. URL https://doi.org/10.1016/j.msec.2019.01.114.

[79] Y. Li, H. Jahr, P. Pavanram, F. S. L. Bobbert, U. Puggi, X.-Y. Zhang, B. Pouran, M. A. Leeflang, H. Weinans, J. Zhou, and A. A. Zadpoor. Additively manufactured functionally graded biodegradable porous iron. *Acta Biomaterialia*, 96:646–661, sep 2019. ISSN 17427061. doi: 10.1016/j.actbio.2019.07.013. URL https://doi.org/10.1016/j.actbio.2019.07.013.

[80] Y. Li, H. Jahr, K. Lietaert, P. Pavanram, A. Yilmaz, L. I. Fockaert, M. A. Leeflang, B. Pouran, Y. Gonzalez-Garcia, H. Weinans, J. M. C. Mol, J. Zhou, and A. A. Zadpoor. Additively manufactured biodegradable porous iron. *Acta Biomaterialia*, 77:380–393, sep 2018. ISSN 17427061. doi: 10.1016/j.actbio.2018.07.011. URL https://doi.org/10.1016/j.actbio.2018.07.011.

[81] L. L. Hench. Bioceramics: From Concept to Clinic. *Journal of the American Ceramic Society*, 74(7):1487–1510, jul 1991. ISSN 0002-7820. doi: 10.1111/j.1151-2916.1991.tb07132.x. URL https://doi.org/10.1111/j.1151-2916.1991.tb07132.x.

[82] T. S. Keller, Z. Mao, and D. M. Spengler. Young's modulus, bending strength, and tissue physical properties of human compact bone. *Journal of Orthopaedic Research*, 8(4):592–603, jul 1990. ISSN 0736-0266. doi: 10.1002/jor.1100080416. URL https://doi.org/10.1002/jor.1100080416.

[83] Y. P. Feng, N. Gaztelumendi, J. Fornell, H. Y. Zhang, P. Solsona, M. D. Baró, S. Suriñach, E. Ibáñez, L. Barrios, E. Pellicer, C. Nogués, and J. Sort. Mechanical properties, corrosion performance and cell viability studies on newly developed porous Fe-Mn-Si-Pd alloys. *Journal of Alloys and Compounds*, 724:1046–1056, jan 2017. ISSN 09258388. doi: 10.1016/j.jallcom.2017.07.112. URL https://doi.org/10.1016/j.jallcom.2017.07.112.

[84] B. Rother, A. Steiner, D. A. Dietrich, H. A. Jehn, J. Haupt, and W. Gissler. Depth-sensing indentation measurements with Vickers and Berkovich indenters. *Journal of Materials Research*, 13(8):2071–2076, aug 1998. ISSN 08842914. doi: 10.1557/JMR.1998.0291. URL https://doi.org/10.1557/JMR.1998.0291.

[85] N. A. Sakharova, J. V. Fernandes, J. M. Antunes, and M. C. Oliveira. Comparison between Berkovich, Vickers and conical indentation tests: A three-dimensional numerical simulation study. *International Journal of Solids and Structures*, 46(5):1095–1104, mar 2009. ISSN 00207683. doi: 10.1016/j.ijsolstr.2008.10.032. URL http://dx.doi.org/10.1016/j.ijsolstr.2008.10.032.

[86] P. Sharma and P. M. Pandey. Corrosion rate modelling of biodegradable porous iron scaffold considering the effect of porosity and pore morphology. *Materials Science and Engineering C*, 103:109776, oct 2019. ISSN 18730191. doi: 10.1016/j.msec.2019.109776. URL https://doi.org/10.1016/j.msec.2019.109776.

[87] ScienceDirect Topics. Selective Laser Melting - an overview, . URL https://www.sciencedirect.com/topics/materials-science/selective-laser-melting. Accessed 28 Jul 2021.

[88] T. Kokubo and H. Takadama. How useful is SBF in predicting in vivo bone bioactivity? *Biomaterials*, 27(15):2907–2915, may 2006. ISSN 01429612. doi: 10.1016/j.biomaterials.2006.01.017. URL https://doi.org/10.1016/j.biomaterials.2006.01.017.

[89] Ime B Obot. Recent advances in computational design of organic materials for corrosion protection of steel in aqueous media. *Book Chapter, INTECH*, pages 123–151, feb 2014. doi: 10.5772/57245. URL https://www.researchgate.net/publication/261710945_Recent_

Advances_in_Computational_Design_of_Organic_Materials_for_Corrosion_Protection_of_Steel_in_Aqueous_Media.

[90] L. Müller and F. A. Müller. Preparation of sbf with different hco3- content and its influence on the composition of biomimetic apatites. *Acta Biomaterialia*, 2(2):181–189, mar 2006. ISSN 181-189. doi: 10.1016/j.actbio.2005.11.001. URL https://doi.org/10.1016/j.actbio.2005.11.001.

[91] Corrosionpedia. Electrical Conductivity. URL https://www.corrosionpedia.com/definition/1481/electrical-conductivity-corrosion. Accessed 28 Jul 2021.

[92] K. Magyari, O. Popescu, and V. Simon. Interface processes between iron containing aluminosilicate systems and simulated body fluid enriched with protein. *Journal of Materials Science: Materials in Medicine*, 21(6):1913–1920, jun 2010. ISSN 0957-4530. doi: 10.1007/s10856-010-4041-5. URL https://doi.org/10.1007/s10856-010-4041-5.

[93] ScienceDirect Topics. Open Circuit Potential - an overview, . URL https://www.sciencedirect.com/topics/chemistry/open-circuit-potential. Accessed 27 Apr 2021.

[94] V. Wagener, A. Faltz, M. S. Killian, P. Schmuki, and S. Virtanen. Protein interactions with corroding metal surfaces: comparison of Mg and Fe. *Faraday Discussions*, 180:347–360, apr 2015. ISSN 1359-6640. doi: 10.1039/C4FD00253A. URL https://doi.org/10.1039/C4FD00253A.

[95] Mars G. Fontana. *Corrosion Engineering*. McGraw-Hill, Singapore, 3rd edition, 1987.

[96] R. A. Legault and M. S. Walker. Linear Polarization Measurements In the Study of Corrosion Inhibition. *Corrosion*, 19(6):222t–226t, jun 1963. ISSN 0010-9312. doi: 10.5006/0010-9312-19.6.222. URL https://doi.org/10.5006/0010-9312-19.6.222.

[97] ASTM E8 / E8M-21. Standard Test Methods for Tension Testing of Metallic Materials. Technical report, ASTM International, West Conshohocken, PA, February 2021. URL http://www.astm.org/cgi-bin/resolver.cgi?E8E8M.

[98] J. P. Magrinho, M. B. Silva, L. M. Alves, A. G. Atkins, and P. A. F. Martins. New methodology for the characterization of failure by fracture in bulk forming. *The Journal of Strain Analysis for Engineering Design*, 53(4):242–247, may 2018. ISSN 0309-3247. doi: 10.1177/0309324718758842. URL https://doi.org/10.1177%2F0309324718758842.

[99] ASTM E9-19. Standard Test Methods of Compression Testing of Metallic Materials at Room Temperature. Technical report, ASTM International, West Conshohocken, PA, April 2019. URL http://www.astm.org/cgi-bin/resolver.cgi?E9.

[100] J. P. Magrinho. Process Limits of Sheet-Bulk Forming. PhD Thesis in Mechanical Engineering, Instituto Superior Técnico, 2019.

[101] COMSOL Multyphics. Reference manual version 5.5. 2019. URL https://doc.comsol.com/5.5/doc/com.comsol.help.comsol/COMSOL_ReferenceManual.pdf.

[102] COMSOL Multiphysics®. *Corrosion Module*. 2018. URL https://doc.comsol.com/5.4/doc/com.comsol.help.corr/CorrosionModuleUsersGuide.pdf.

[103] COMSOL Multyphics. Corrosion module user's guide version 5.4. 2018. URL https://doc.comsol.com/5.4/doc/com.comsol.help.corr/CorrosionModuleUsersGuide.pdf.

[104] J. M. C. Rodrigues and P. A. F. Martins. *Tecnologia Mecânica*. Escolar Editora, Portugal, 2nd edition, 2010.

Appendix A

COMSOL tutorial

The *COMSOL* tutorial created explaining how to setup the computer and create a model like the ones developed in this work is online on https://tinyurl.com/Tutorial-COMSOL-IST.

Also, it is presented below the thumbnails of the slides from the tutorial mentioned.

Master Thesis

Mechanical characterization of iron for application in medical implants

COMSOL Tutorial

Pedro Neves nº 84326

Mentors:

Maria Beatriz Silva

Maria de Fátima Reis Vaz

1

1. COMSOL computer Setup

- 1.1. Install Autologon
  - Download the software from https://docs.microsoft.com/en-us/sysinternals/downloads/autologon
    - Open the .zip file downloaded

2

3

4

1. COMSOL computer Setup

- 1.2. COMSOL auto-start when the computer is turned on or restarted
  - Instructions performed as on this video https://www.youtube.com/watch?v=FkdTYqCRq_I&ab_channel=mk

5

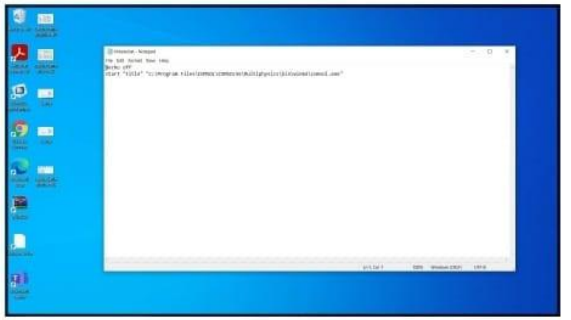

6

7

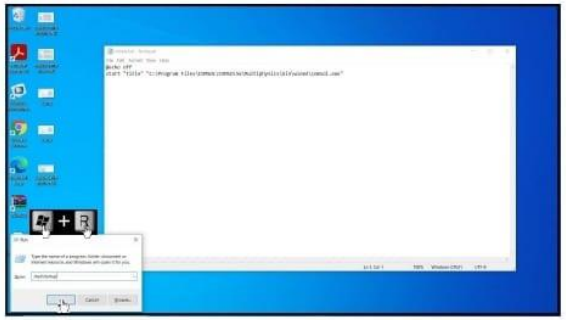

8

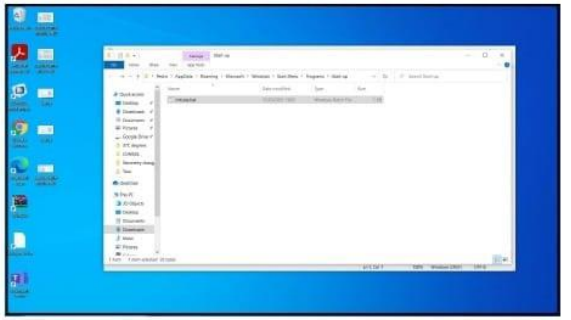

9

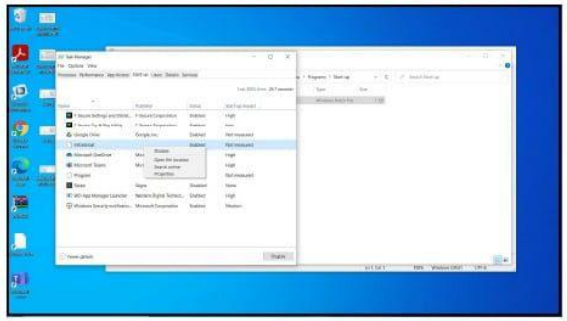

10

2. User computer Setup

- 2.1. Install and connect to IST VPN in your computer
  - Instructions available at https://si.tecnico.ulisboa.pt/servicos/redes-e-conetividade/vpn/
- 2.2. Remotely access to COMSOL computer
  - Use Windows Remote Desktop
    - You will need
      - **Computer name**
      - **User ID Name**
      - **User Password**

11

3. COMSOL model building

12

3.1. Choosing Space Dimension, Physics and Study

13

14

15

16

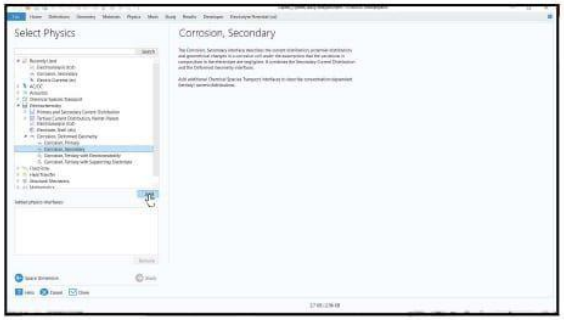

17

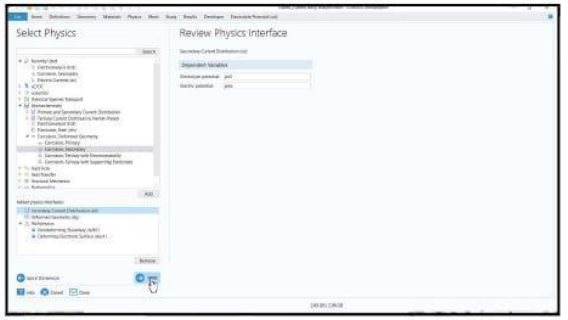

18

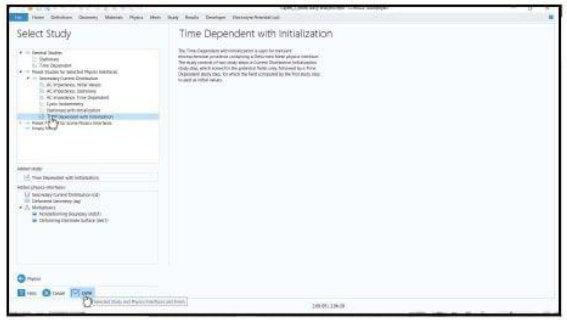

19

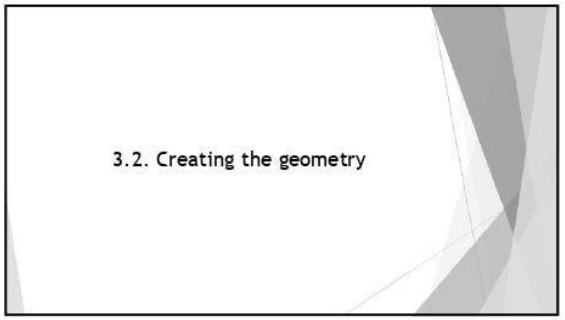

20

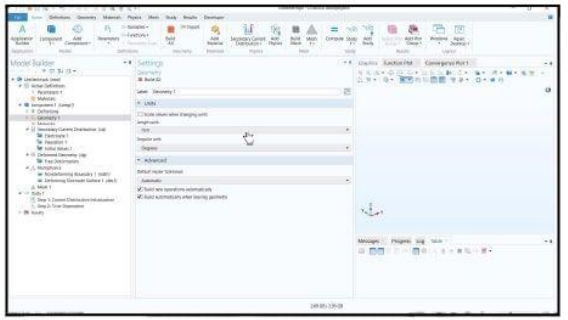

21

22

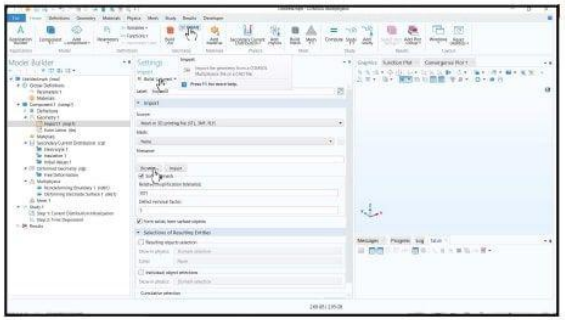

23

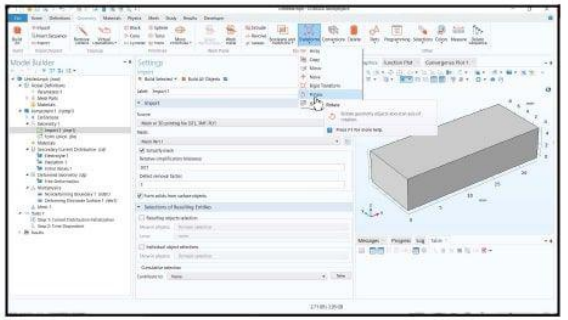

24

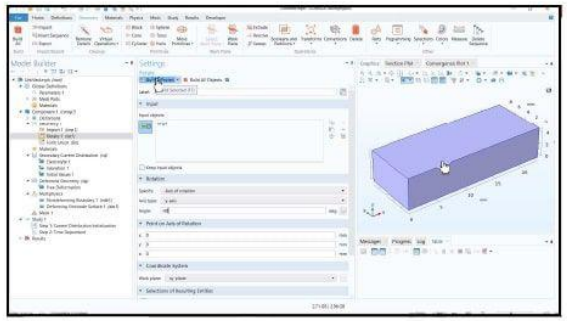

25

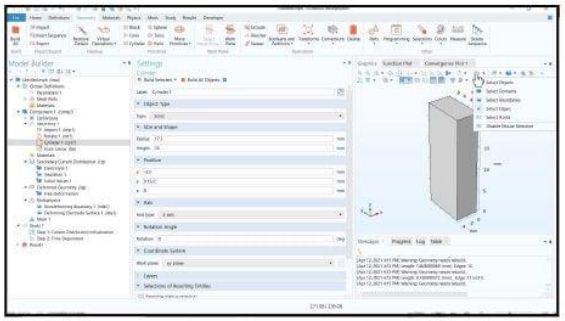

26

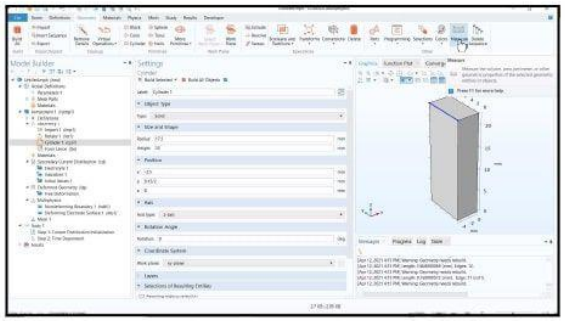

27

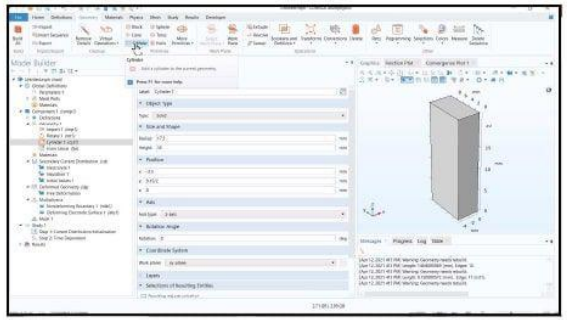

28

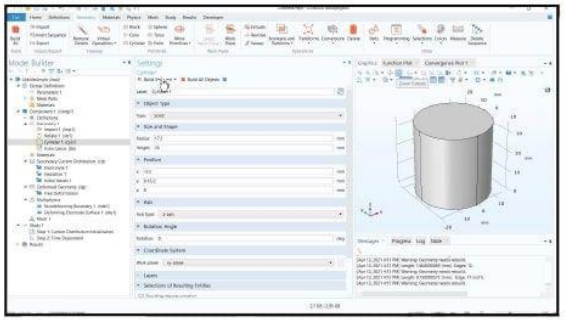

29

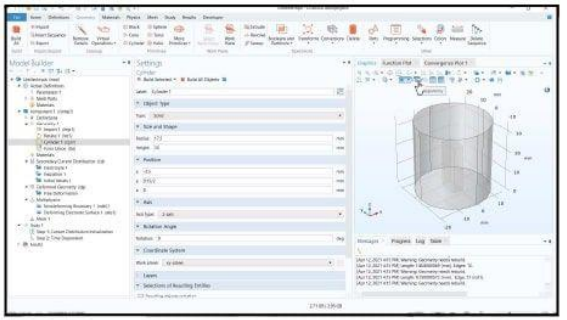

30

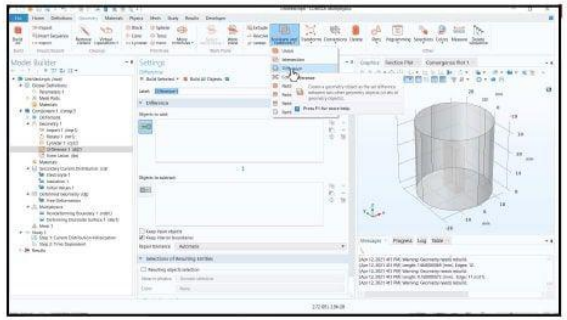

31

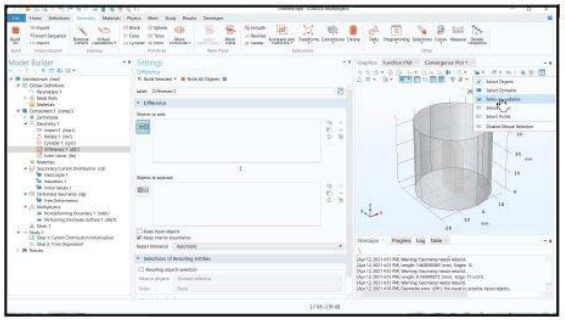

32

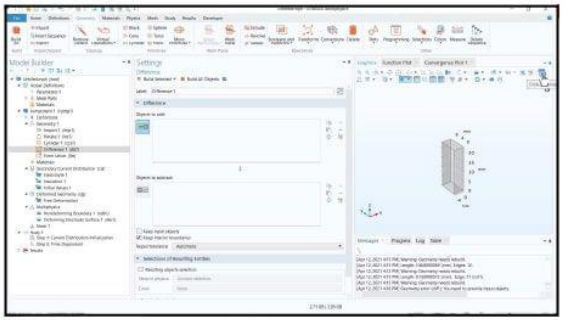

33

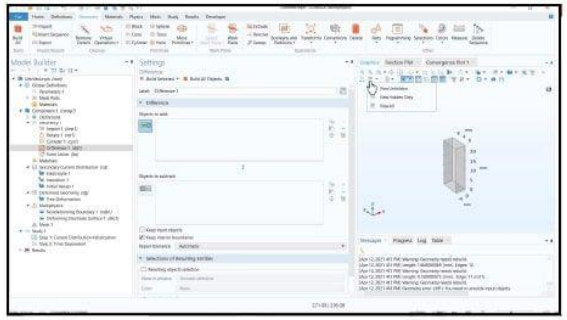

34

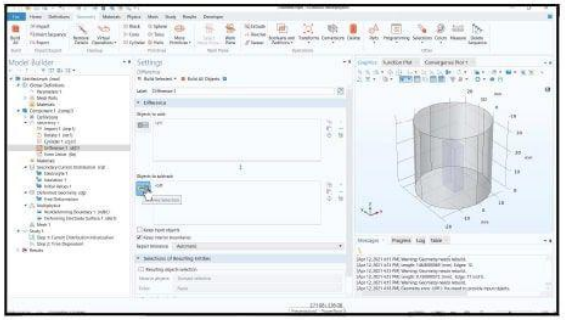

35

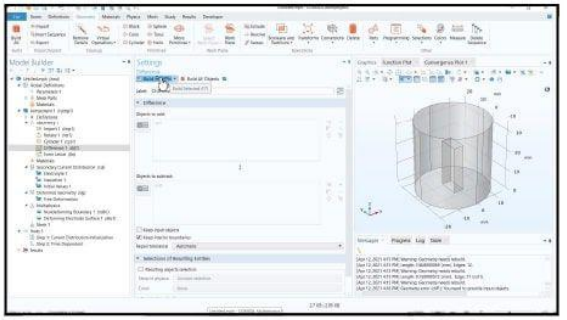

36

3.3. Model Material(s)

37

3.3.1. Editing existent material

38

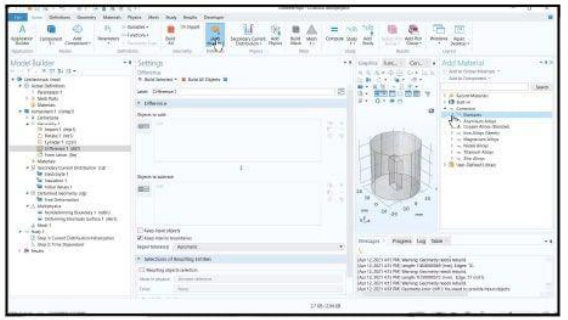

39

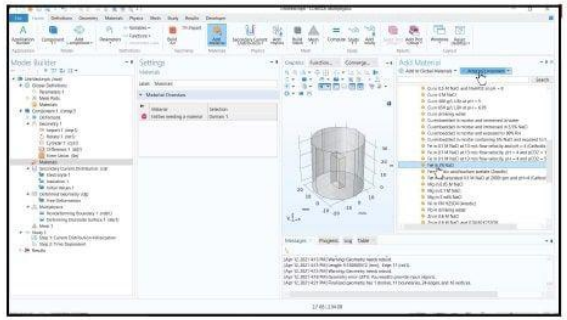

40

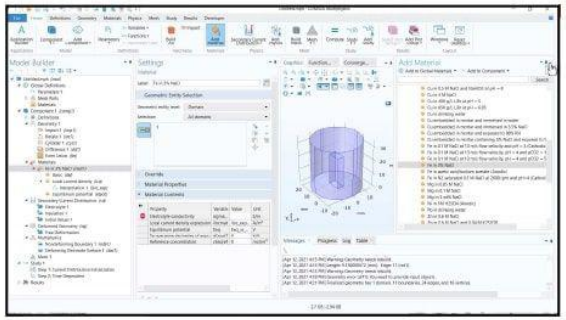

41

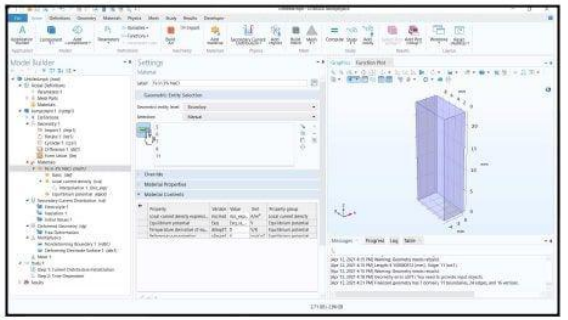

42

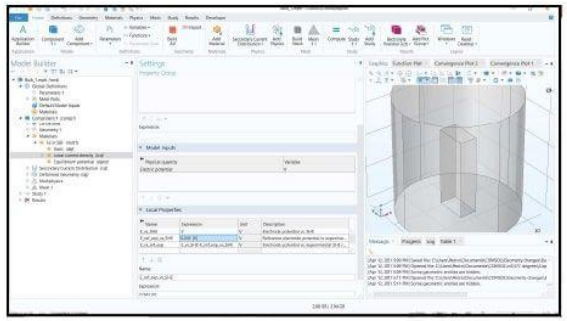

43

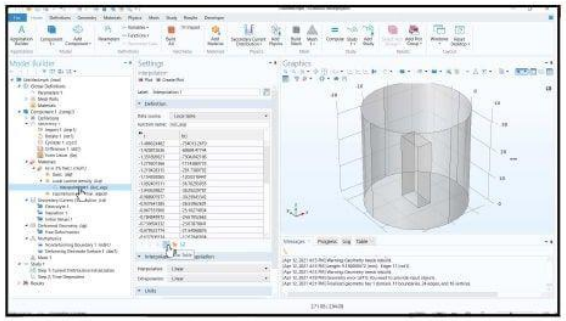

44

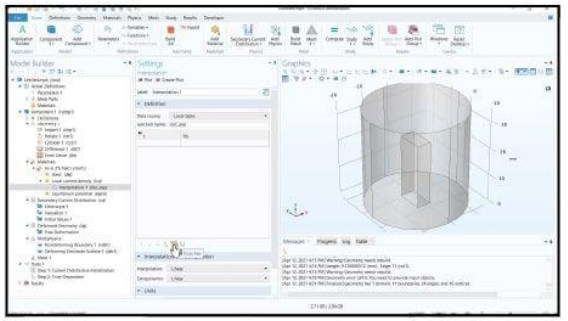

45

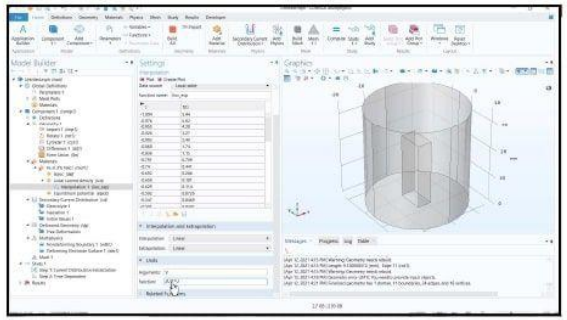

46

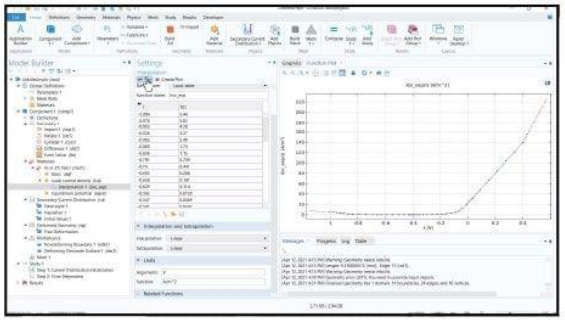

47

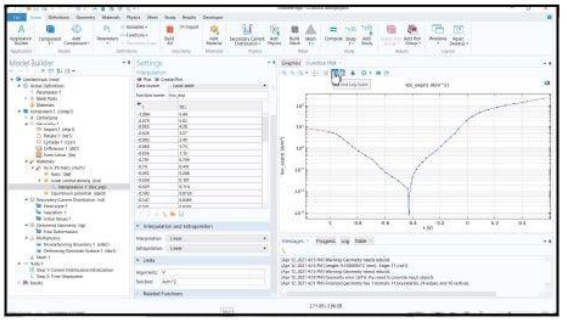

48

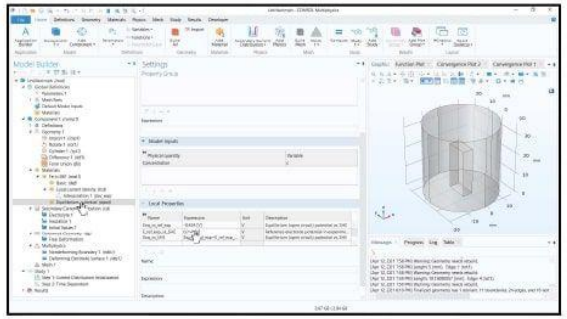

49

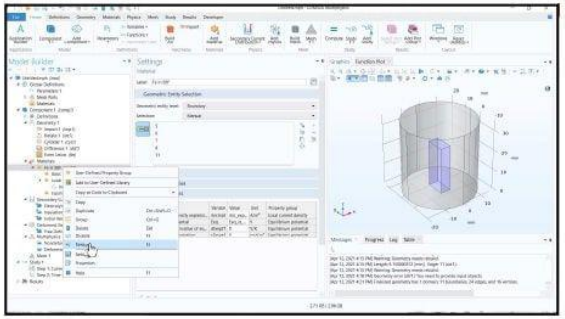

50

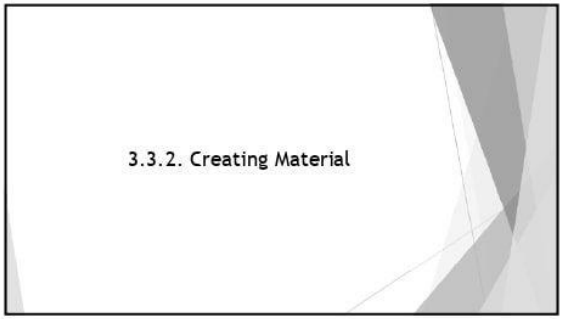

51

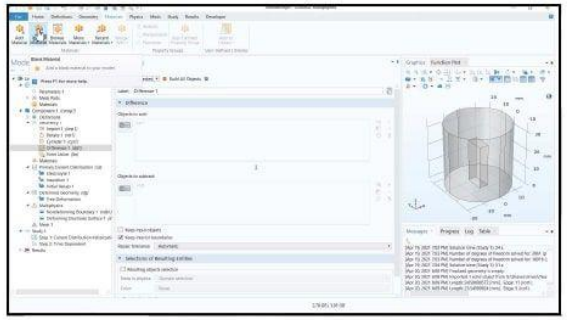

52

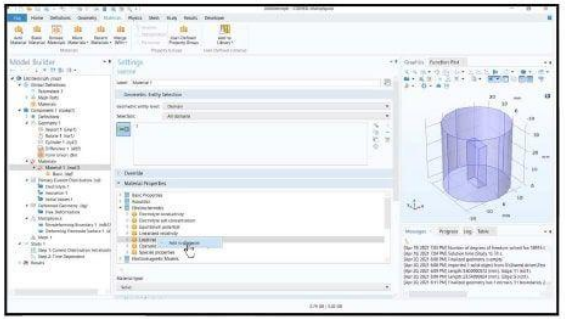

53

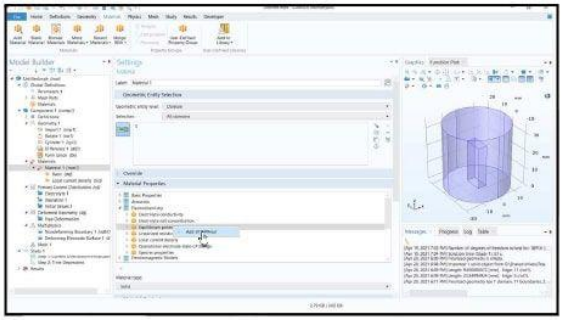

54

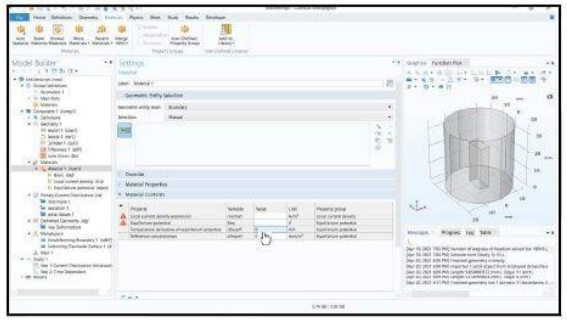

55

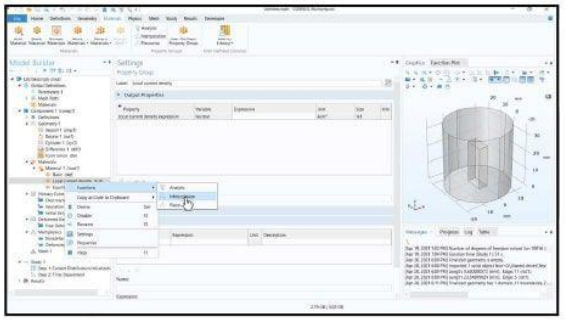

56

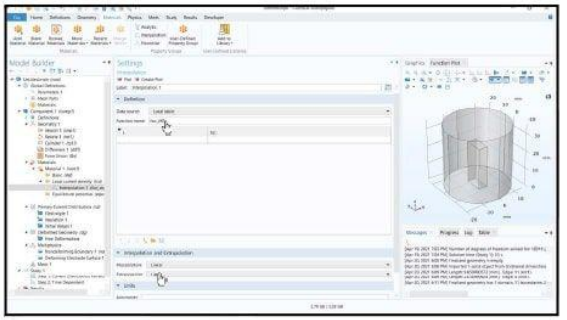

57

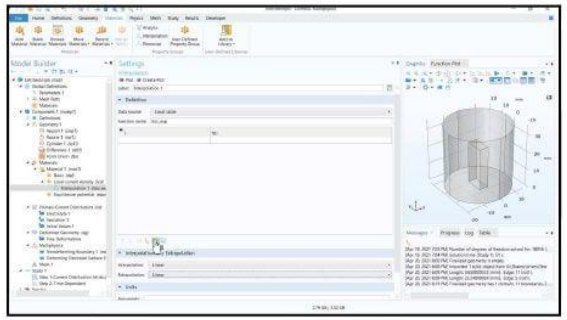

58

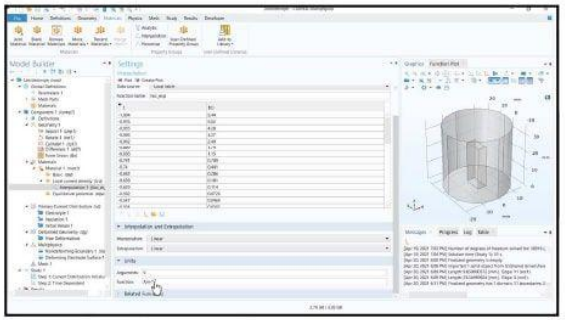

59

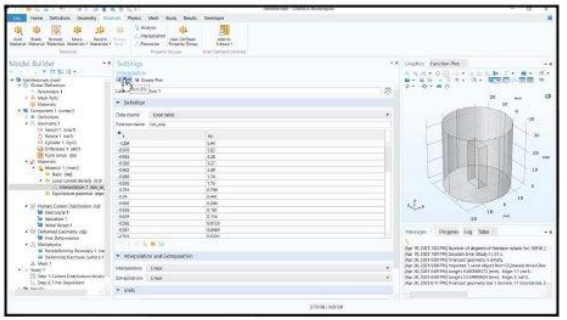

60

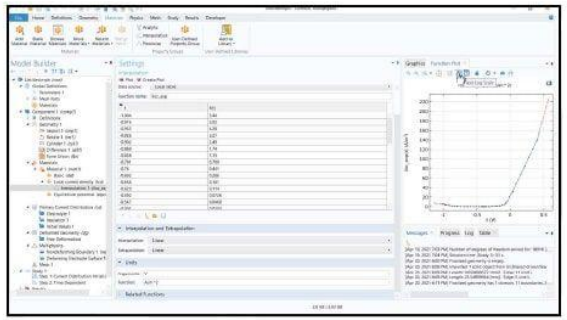

61

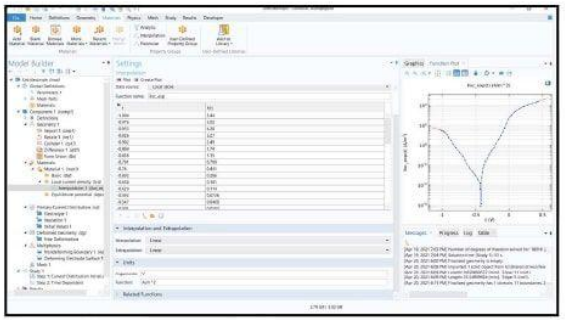

62

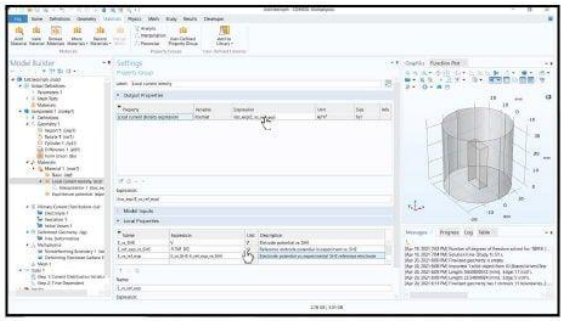

63

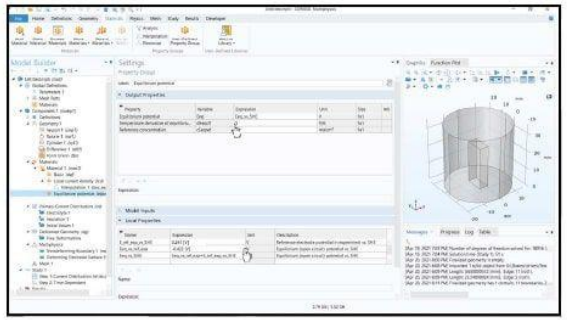

64

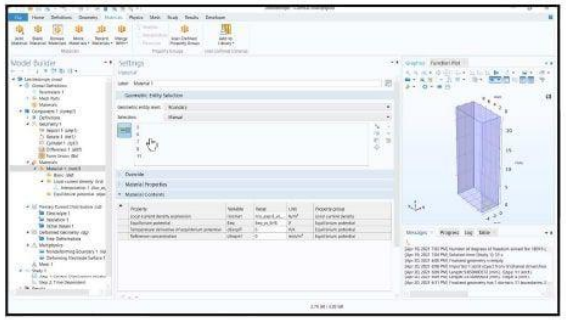

65

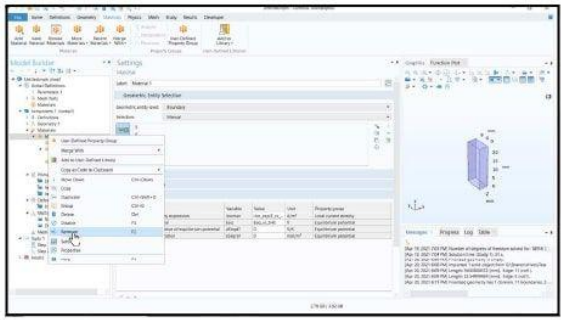

66

3.4. Setting the Current Distribution properties and boundary conditions

67

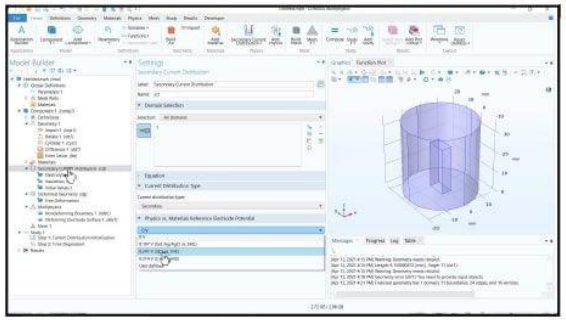

68

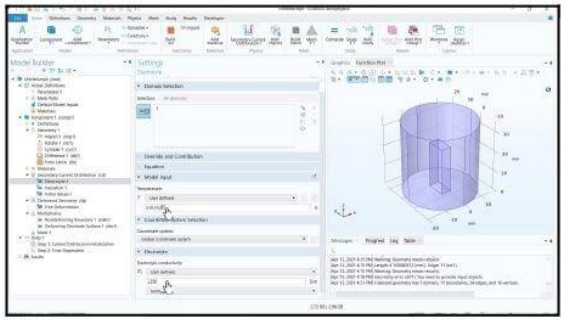

69

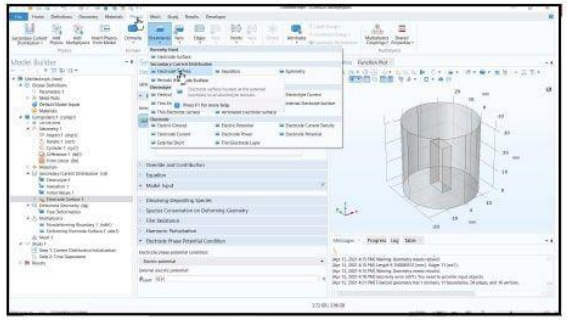

70

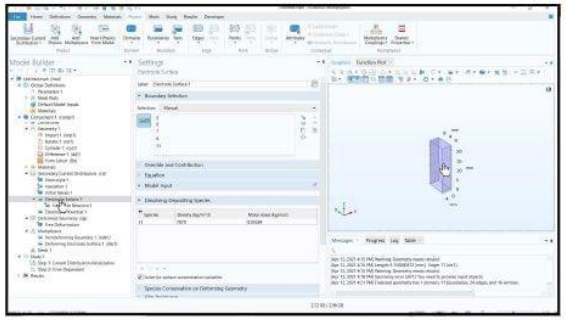

71

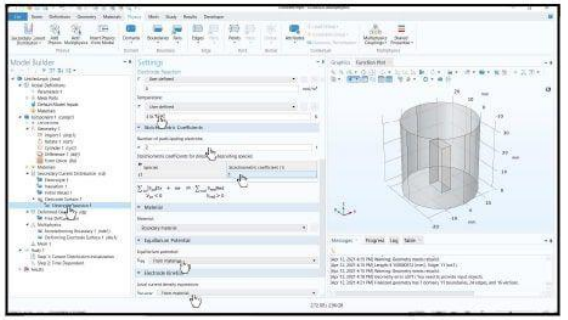

72

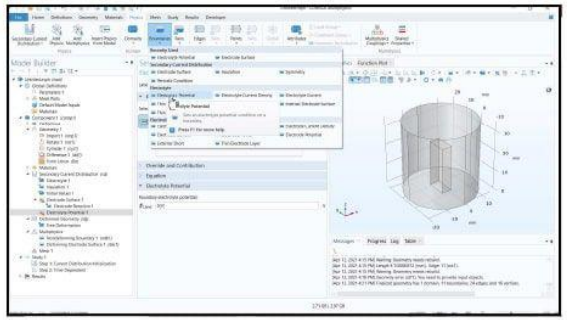

73

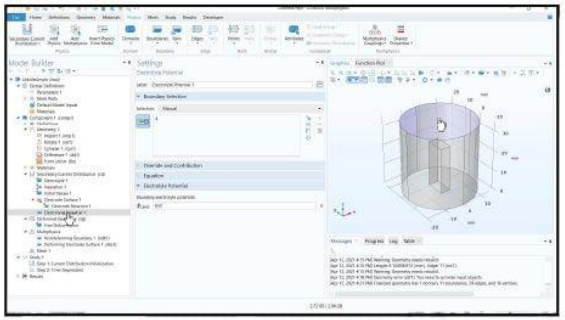

74

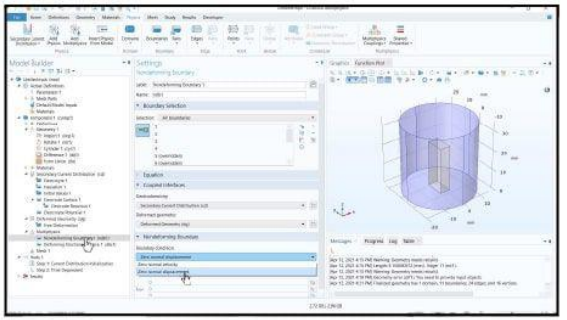

75

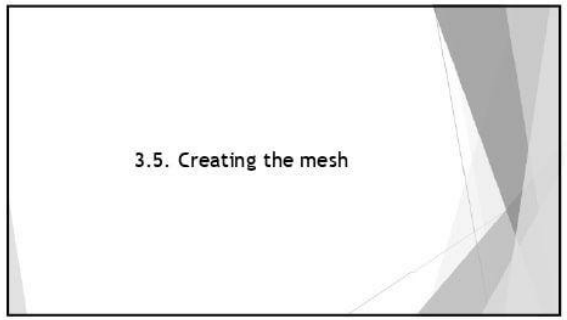

76

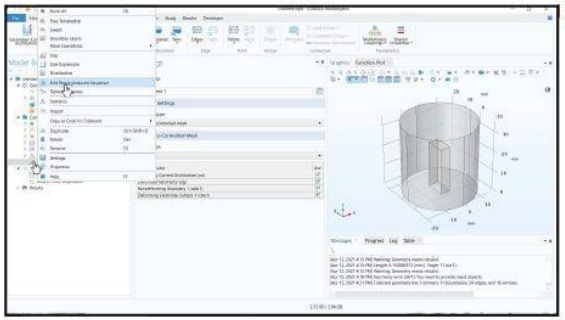

77

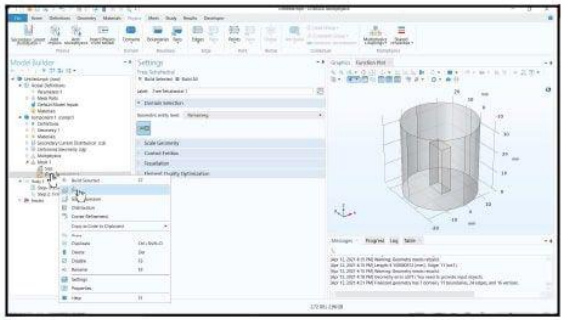

78

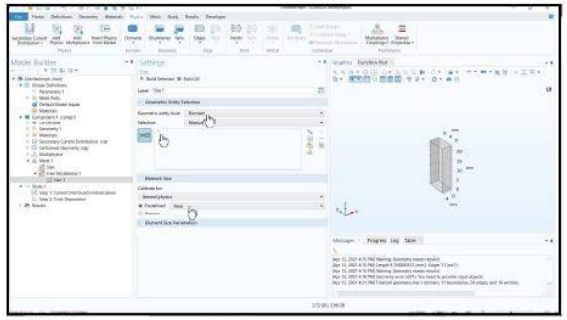

79

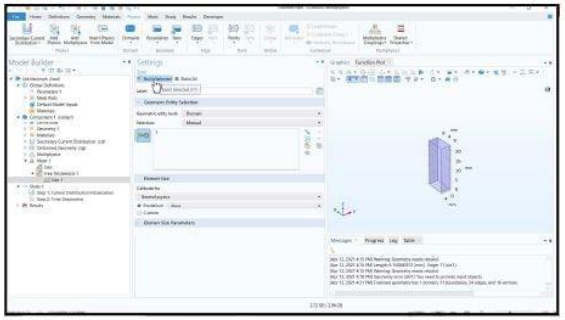

80

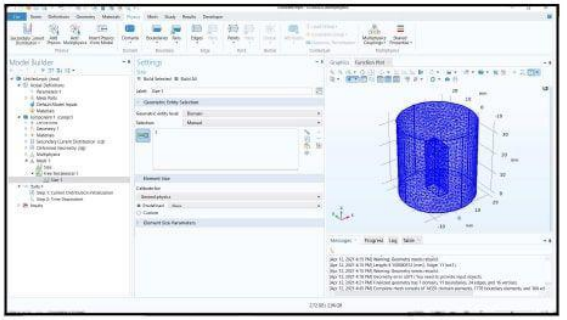

81

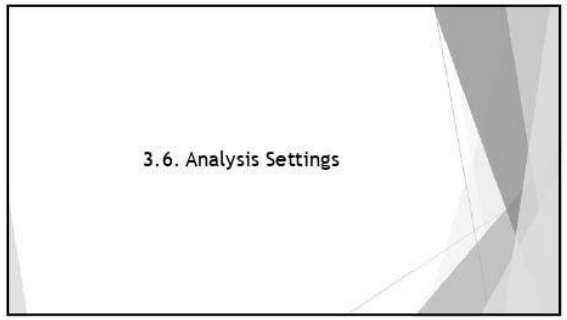

82

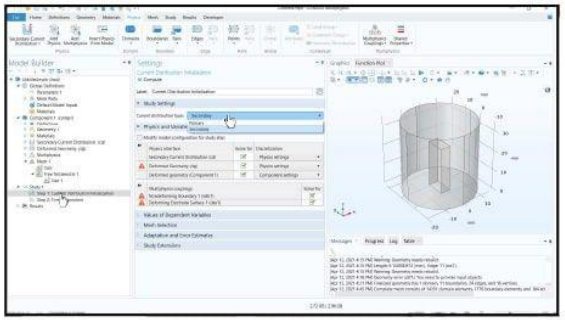

83

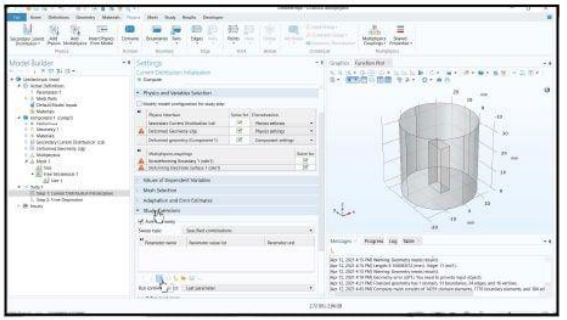

84

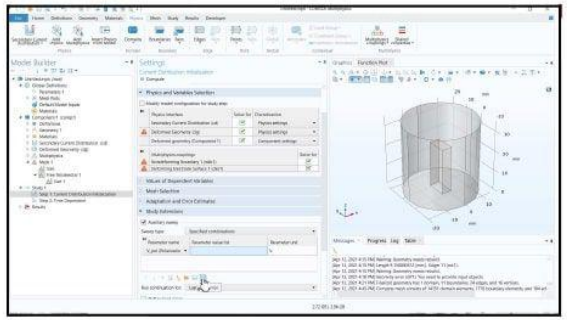

85

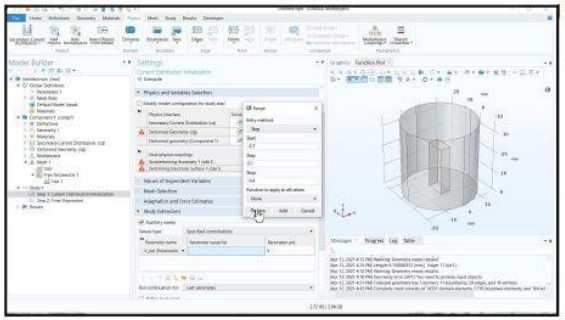

86

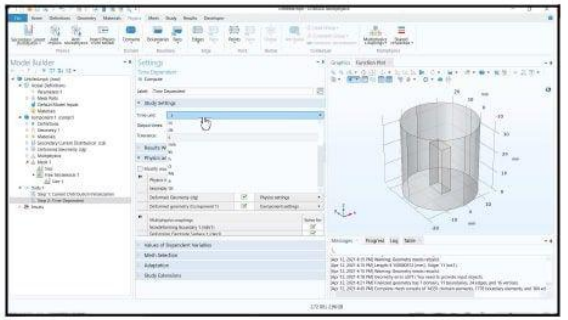

87

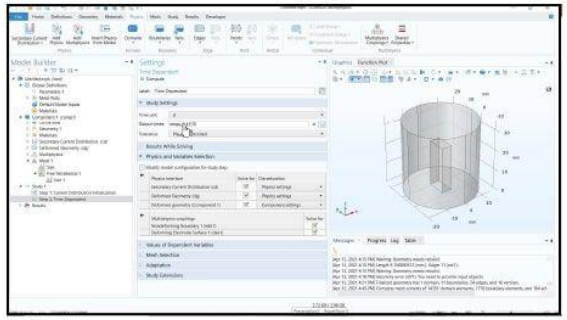

88

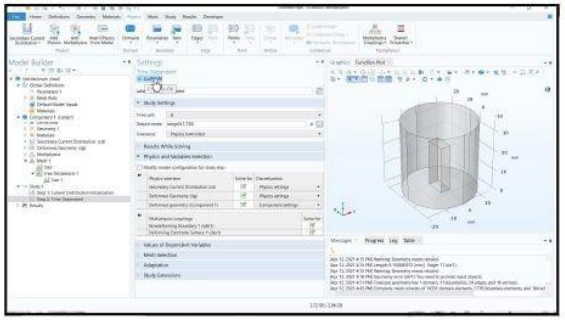

89

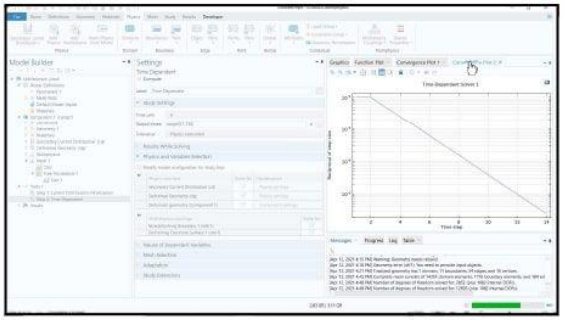

90

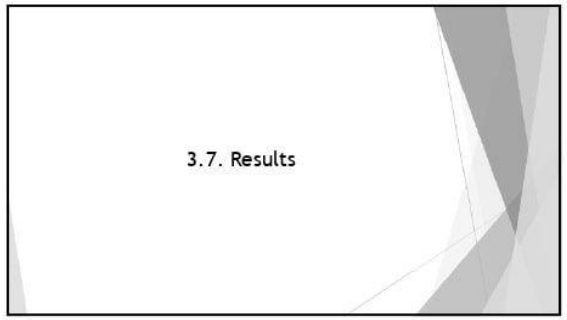

91

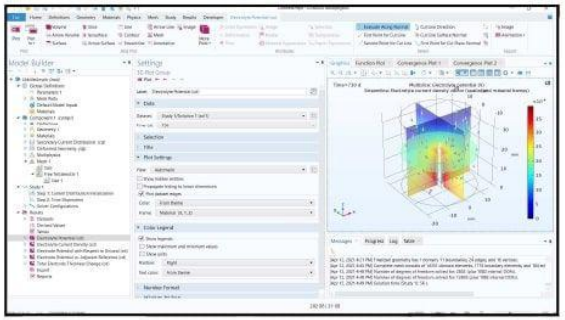

92

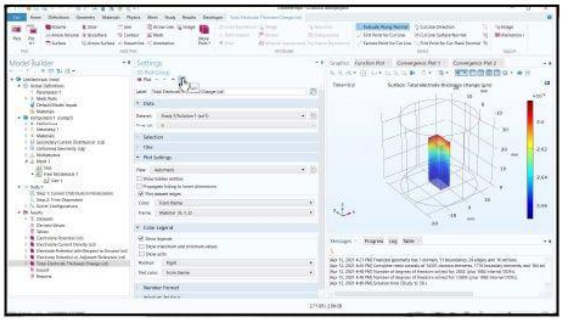

93

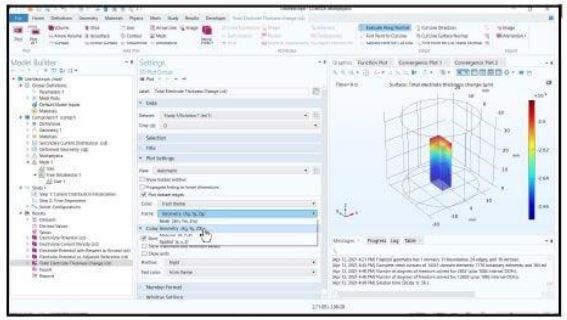

94

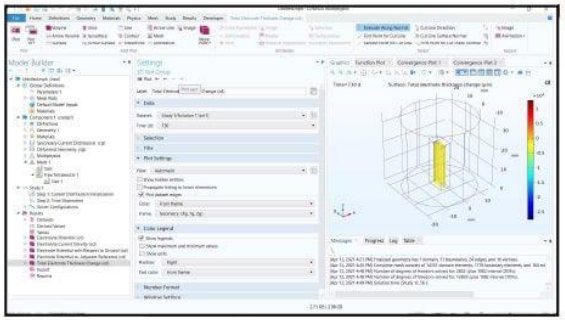

95

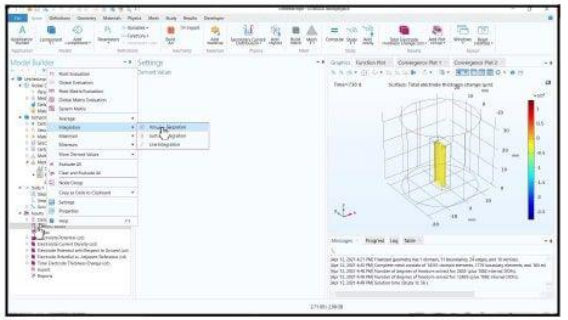

96

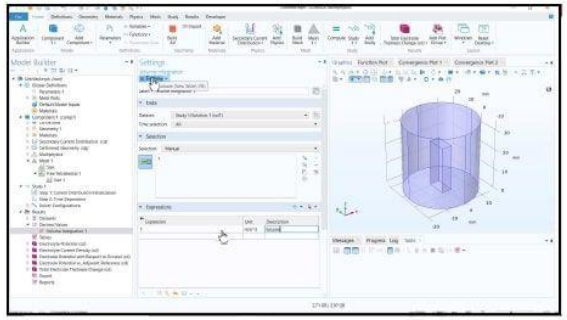

97

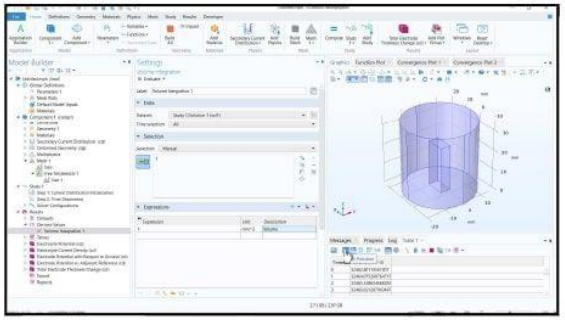

98

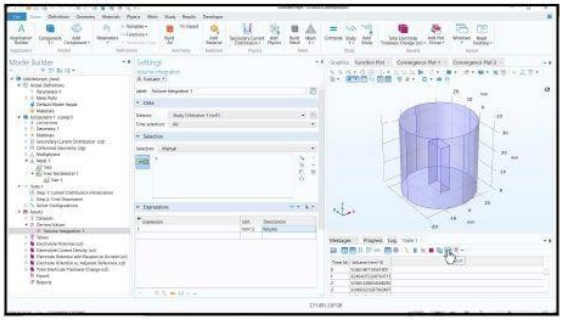

99

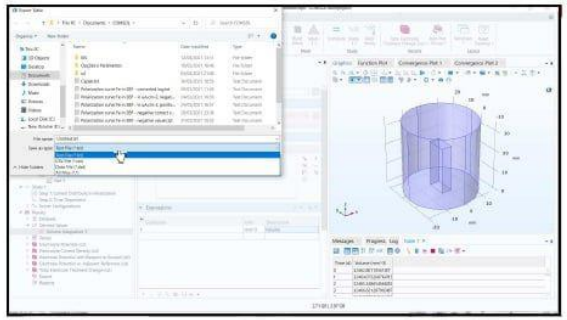

100

4. Extras

101

4.1. Using one functional model for different geometries

102

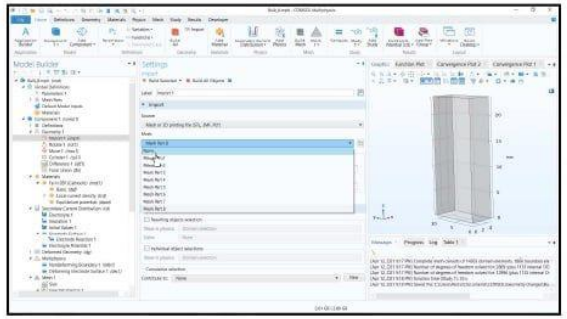

103

4.2. Exporting mesh from the results to use in a new model

104

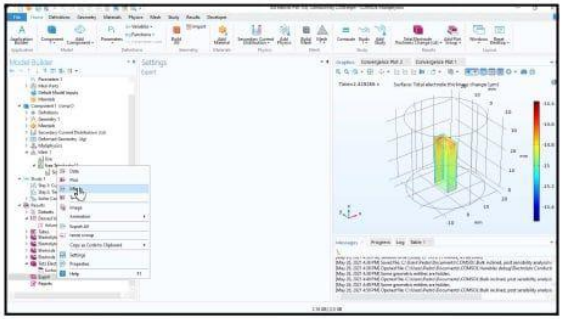

105

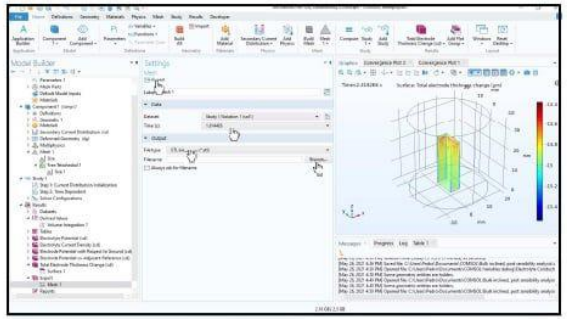

106

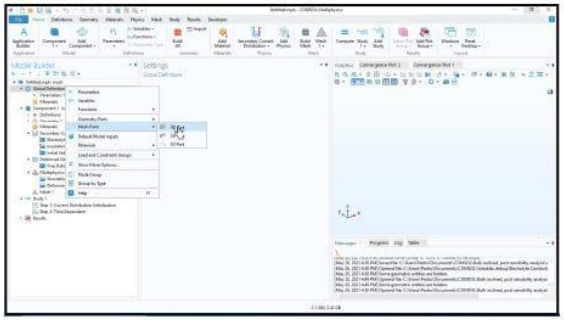

107

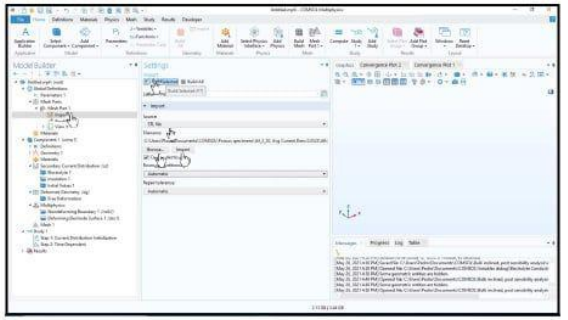

108

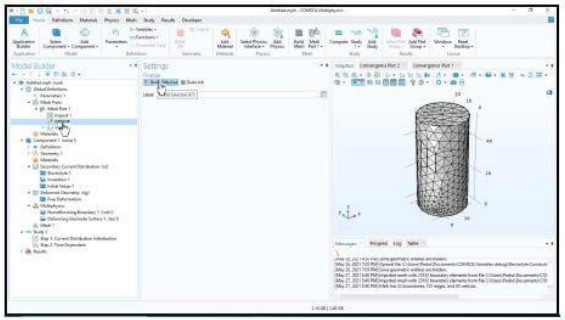

109

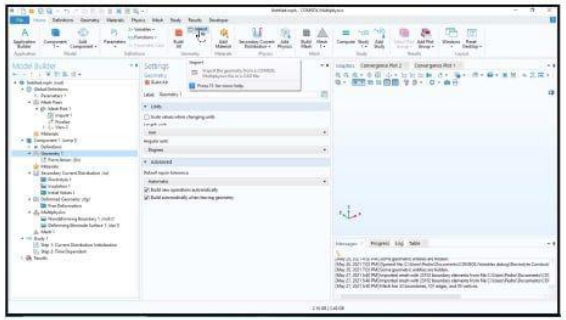

110

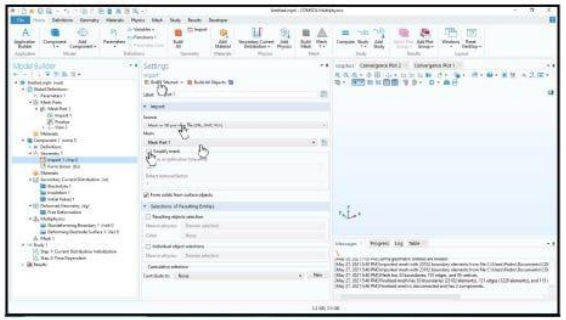

111

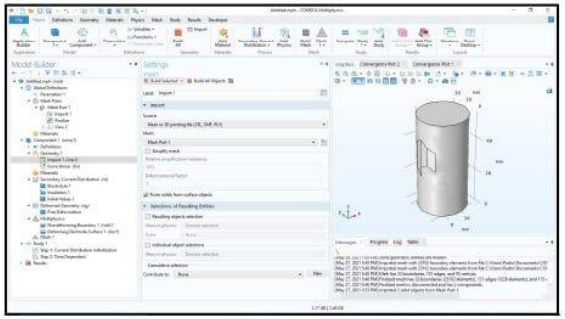

112

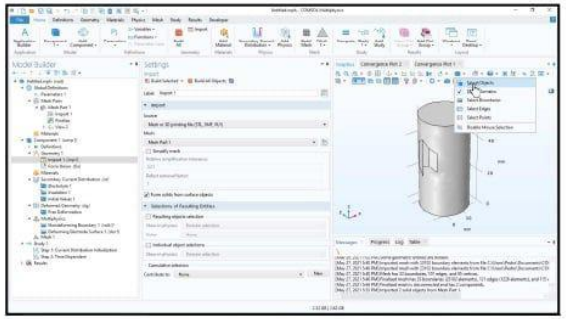

113

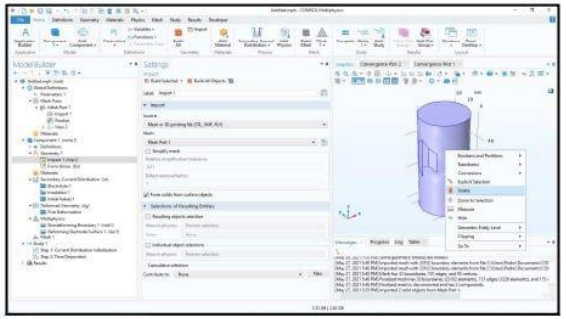

114

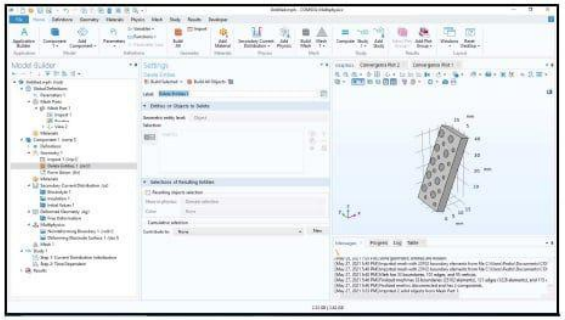

115